DOCTORAATSPROEFSCHRIFT

2012 | Faculteit Wetenschappen

Photovoltaic cells based on zinc oxide nanorod arrays and poly(3-hexylthiophene)

Proefschrift voorgelegd tot het behalen van de graad van
Doctor in de Wetenschappen, Fysica, te verdedigen door:

Bert CONINGS

Promotor: prof. dr. Jean V. Manca
Copromotor: prof. dr. Hans-Gerd Boyen

D/2012/2451/17

universiteit hasselt

Chairman	Prof. dr. Marc D'Olieslaeger, UHasselt
Promotor	Prof. dr. Jean V. Manca, UHasselt
Co-promotor	Prof. dr. Hans-Gerd Boyen, UHasselt
Members of the jury	Prof. dr. Marlies K. Van Bael, UHasselt
	Prof. dr. Dirk Vanderzande, UHasselt
	Dr. Hans Moons, UHasselt
	Prof. dr. ir. René A.J. Janssen, TU Eindhoven (NL)
	Em. prof. dr. ir. Robert Mertens, KU Leuven
	Dr. Jan Kroon, ECN (NL)
	Prof. dr. Germà Garcia-Belmonte, Universitat Jaume I, Castelló (ES)

Dankwoord

Experience is the name everyone gives to their mistakes. Oscar Wilde

Het klinkt in eerste instantie een beetje als een paradox maar toch is het de logica zelve: in dezelfde mate dat een doctoraat een persoonlijke missie is, hangt het welslagen ervan voor een groot stuk af van de samenwerking met een heleboel collega's. Hierbij neem ik dan ook de gelegenheid om ze uitgebreid te bedanken voor de vruchtbare samenwerking gedurende de voorbije jaren.

Allereerst bedank ik mijn promotor Prof. dr. Jean Manca om me enkele jaren geleden na mijn masterstage in onze groep al te "promoveren" tot doctoraatsstudent. Jean, ik apprecieer ten zeerste de vrijheid die je me hebt gegeven in mijn onderzoek, om wegen in te slaan die ik zelf het interessantst vond en waar ik het meeste potentieel in zag. Dat heeft mijn wetenschappelijke zelfstandigheid en creativiteit alleen maar positief beïnvloed. Je open geest, enthousiasme, positivisme en gemoedelijkheid typeren je als inspirerende groepsleider, ondanks je veeleisende bezigheden als decaan. Fijn dat je altijd tijd maakte voor een kritische blik op mijn manuscripten. Ook bedankt om me de mogelijkheid te verschaffen tot het bijwonen van (en een beetje bij te dragen tot) indrukwekkende congressen, ik ben heel blij dat ik die kansen gekregen heb.

Mijn co-promotor Prof. dr. Hans-Gerd Boyen heeft een grote rol gespeeld in mijn doctoraat. Hans-Gerd, ik bedank je graag in het Nederlands omdat ik ervan overtuigd ben dat je me intussen nagenoeg perfect verstaat na onze informele taaloefensessies (en omdat mijn Duits je wellicht zou irriteren). Ik ben ongelofelijk dankbaar voor je grote aanhoudende steun in mijn onderzoek, en je bereidheid om tijd te maken voor vele uitgebreide discussies ondanks je goedgevulde agenda en activiteiten binnen je eigen onderzoeksgroep. Je intimiderende hoeveelheid aan kennis en doorzicht hebben me toegang gegeven tot intrigerende onderzoekspaden, met verrassende en fascinerende resultaten tot gevolg. Je vermogen om extreem kritische en terechte opmerkingen te geven op een zeer positieve en constructieve manier is iets wat weinigen gegeven is. Hartelijk dank ook voor de vele uren die je gespendeerd hebt

aan het meten en interpreteren van XPS data, waarbij je nooit genoegen nam met bijna-perfectie, en voor het aanscherpen van mijn manuscripten. "Deutsche Gründlichkeit" heeft voor mij alleszins een gezicht gekregen. Bovendien weet ik nu ook meer "the big hammer approach" te appreciëren waar nodig, zeker als het gaat om "shaking the fundamentals", en heb ik geleerd dat "it's always going in a spiral"!

Het derde lid van mijn doctoraatscommissie was Prof. dr. Marlies Van Bael. Marlies, bedankt om mijn manuscripten, inclusief deze thesis, ook met een chemisch oog door te nemen, dat is zeker nuttig voor de brede leesbaarheid ervan. Overigens apprecieer ik dat je, gegeven je sterke synthese-achtergrond, toch steeds erg geïnteresseerd was in de elektrische karakterizatie waar ik mee kwam aandraven.

Verder wil ik de leden van de jury bedanken voor hun bereidheid tot het evalueren van mijn werk, en het Bijzonder Onderzoeksfonds voor financiële ondersteuning.

Een dikke merci ook voor dr. Jan D'Haen en Bart Ruttens, voor de regelmatige SEM sessies waarbij ik steeds weer kon rekenen op scherpe, niet-astigmatische prentjes, compleet vrij van trillingen. Zelfs in drukke tijden ten behoeve van de industrie hebben jullie altijd zo snel mogelijk tijd gemaakt om me weer te fascineren met de wondere wereld van het nano-landschap. Dat landschap is uiteraard vaak een dikke tegenvaller, maar met jullie opmerkzaamheid en nuttig advies kon ik altijd een stap verder!

Johnny, het lijkt alsof je altijd in de startblokken staat om me te helpen, echt. Je to-do lijstjes hebben continu ongeveer de lengte van het menu van een doorsnee afhaalchinees, en toch heb je me altijd zeer snel en effectief kunnen bijstaan bij alle mogelijke technische uitdagingen. Hoe dikwijls je ook nog beweert dat iedereen vervangbaar is, ik zet hier toch zwart op wit het tegendeel: zonder jou valt het IMO op zijn gat! Ieder onderzoeksinstituut zou een echte Johnny Baccus moeten hebben! Ook je ontwerpvaardigheden waardeer ik ten zeerste, zowel binnen als buiten het IMO. Bovendien heb je me ook wat levenswijsheid bijgebracht, maar voel je vooral niet oud door deze uitspraak.

Als het over technische ondersteuning gaat, denk ik ook aan Johan Soogen, de man die alle digitale ontwerpen kan omzetten naar een tastbaar iets. Johan, het was altijd weer een plezier om je vers gemaakte creaties in gebruik te nemen, waarvoor dank!

Christel en Hilde, bedankt voor snelle en correcte bestellingen van producten, en om me te voorzien van alle mogelijke "consumables", van banaal tot exotisch, en om me af en toe te verblijden met een nieuw speeltje zoals een pincet of Pyrex-fles. Ook was ik altijd gerustgesteld als jullie me instrueerden aangaande waar ik dit of dat potentieel carcinogeen goedje veilig kon weggieten.

Jan en Lieven ben ik dankbaar voor hun kundige technische ondersteuning wat betreft elektronica. Van weerstand tot wafer prober, jullie brede waaier aan expertise is onmisbaar!

Ik mag zeker de dames van het secretariaat niet vergeten. Lea, Relinde, Lisette en sinds kort ook Ellen, bedankt voor het geduld om me tot vervelens toe opnieuw uit te leggen wat ik op welk formulier moet invullen, en voor het uitgebreid toelichten van al die prachtige cryptische, schijnbaar zichzelf tegensprekende, omschrijvingen die op zulke formulieren steevast hun aanwezigheid opeisen.

Natuurlijk bedank ik ook mijn collega-doctorandi en de postdocs van de ONE^2-groep, voor hun bereidheid tot discussie en hun behulpzaamheid. Donato and Fortunato, I want to thank you guys in particular for the plentiful discussions regarding recombination and other fundamental photovoltaic working principles. I also greatly value your skills as baristas, your home country can be proud! As I write this, our trip to Sweden is still ahead of us, but I'm sure it will be a lot of fun! Donato, thanks a lot as well for the CELIV and TPV measurements, they helped a lot!

Voor UV/Vis metingen kon ik steeds terecht bij scheikunde, waar Huguette Penxten me regelmatig weer wat wijzer kon maken, en een ontspannen babbel maakte die metingen dikwijls ook wat minder eentonig. Dankjewel Huguette!

Hong, thanks a lot for your help with characterizing the single crystal! Your knowledge on high temperature processes has been indispensable, and I definitely appreciate your precise attitude in AFM and XPS. I also want to thank the rest of Prof. Boyen's research group for specific lab advice and interesting discussions.

Anitha, first of all I want to thank you for synthesizing the polystyrene dispersions. They show a lot of potential for the purpose I intended and although time didn't allow this route to be more thoroughly elaborated during my PhD, I certainly hope to explore it further in the future. Also thanks for all the interdisciplinary scientific

discussions, it was always a pleasure to approach things from a different point of view. By the way, we should revisit our informal Dutch courses, so you can buy your fruits and vegetables without any problem here in Belgium too. And remember, we all possess a certain amount of Sheldonian brain cells, but it's not a problem as long as we don't call it a problem!

Verder wil ik ook de rest van mijn bureaugenootjes in de bloemetjes zetten. Jan, Bart, Kasper, Mohammed, Kathia en Marloes, jullie zorgden steeds weer voor de positieve sfeer in 1.32, en daar profiteren we allemaal van! Bart, van jou leerde ik om blij te zijn met kleine dingen, ik heb nog nooit iemand zo opgetogen geweten om een Starbucks-koffie met bijhorende pumpkin loaf. Smaakt zoveel beter in "Frisco", maar de boodschap is er wel! Goeie toelie, en good times! Iets veeleisender was jij, Paulius, nippend van je Rémy Martin in de Marriott, maar die was waarschijnlijk wel nodig ter compensatie van je verbeten weigering tot het aanpassen aan de afwijkende tijdzone, en was je daarom van harte gegund! Nu ik het dan toch over San Francisco heb, Ken, bedankt om ons te laten kennis maken met de "local cuisine", waarbij anticipatie een sleutelingrediënt was!

Lars, ik wil jou apart vermelden als bureaugenoot, maar ook als kameraad. Allereerst ben ik je zeer dankbaar voor je grenzeloze behulpzaamheid, en ik vind nog altijd dat een consultantfunctie je goed zou staan. Onze verschillende wetenschappelijke achtergronden hebben vaak tot een boeiende kruisbestuiving geleid, iets waar ik altijd voor open sta. Verder kon ik ook steeds bij je terecht met bedenkingen over de dingen des levens buiten het IMO, waarbij ik telkens kon rekenen op je onbevooroordeelde en genuanceerde mening. Dankjewel! Ik wens je ook veel werkvreugde in je nieuwe job, en geluk met Evelien! Trouwens, Evelien, ik wil jou ook bedanken voor de synthese van een aantal polystyreen dispersies. Je nauwgezetheid en vastberadenheid zullen zeker hun vruchten afwerpen, zowel voor het afronden van je studie als in je toekomstige job. Succes ermee!

Linny, jij bent zonder twijfel de belangrijkste persoon die ik wil bedanken. Elk staal zink oxide waar ik mee te maken heb gehad is met de grootste zorg door jou gesynthetiseerd, en zonder dat aspect was dit maar een heel dun boekje geweest. Je nauwgezetheid, overmaat aan gezond verstand, stiptheid en betrokkenheid zijn nog

maar enkele van je eigenschappen die ik buitengewoon waardeer. Buiten de pure synthese heb je me ook altijd met veel ijver bijgestaan in het ontwerpen van onderzoeksstrategieën en het interpreteren van resultaten. Ik beschouw de samenwerking met jou als een prachtig voorbeeld van synergie, een bewijs dat één plus één figuurlijk veel meer kan zijn dan twee. Ik had me onmogelijk een betere onderzoekspartner kunnen toewensen. Ik heb heel wat scheikundige achtergrond bijgewonnen door jou, iets wat ik op prijs stel als fysicus, in het bijzonder me bewust zijnde van de continue overlap tussen onze disciplines in het vakgebied photovoltaics. Telkens als de motivatie weer eens ver zoek was, meestal als gevolg van gevestigde fysische wetten zoals de wet van Murphy en het behoud van miserie, wist je me als geen ander er weer bovenop te helpen. Telkens als je me verzekerde dat het wel weer in orde zou komen is dat in alle gevallen ook zo gebeurd. Ik heb enorm genoten van onze samenwerking en ik heb oprecht het gevoel dat we een robuust team zijn. Je hebt van mij niet alleen een betere wetenschapper, maar ook een beter mens gemaakt. Ik wil ook nog vermelden dat ik een prachtige tijd heb gehad in San Francisco met (o.a.) jou als reisgezel, als wetenschapper en als toerist, en dat het telkens weer plezant is om een dansje met je wagen. Ik wens je tot slot heel veel geluk toe in de nieuwe weg die je bent ingeslagen als postdoc! Je hebt alles in huis om ook daar een succes van te maken!

Tenslotte wil ik de mensen in mijn naaste omgeving (buiten het IMO) bedanken. Zeker mijn vrienden voor de nodige ontspanning die nodig was om regelmatig mijn geest te verluchten, en om zonder morren tegen mijn "grumpy face" op te kijken als de zonnecellen die dag weer eens niet genoeg hadden gepresteerd naar mijn zin. En last but certainly not least bedank ik ook van harte mijn ouders, die me in de eerste plaats gemotiveerd hebben om te studeren, en me altijd hebben gesteund in moeilijke periodes. Met een serieuze of humoristische toets (de zos al ens zèggen hè pa, in ozze jongen tied waas dat allemoal hiël anges!), ik weet dat ik kan rekenen op de nodige "geestelijke bijstand". Jullie zijn steeds een veilige thuishaven, dankjewel!

Bert

Publications

§ included in this thesis

* equally contributing authors

S. Bertho, G. Janssen, T.J. Cleij, B. Conings, W. Moons, A. Gadisa, J. D'Haen, E. Goovaerts, L. Lutsen, J.V. Manca, D.J.M. Vanderzande, *Effect of temperature on the morphological and photovoltaic stability of bulk heterojunction polymer:fullerene solar cells,* Sol. Energy Mater. Sol. Cells **2008**, *92*, 753.

B. Conings, S. Bertho, K. Vandewal, A. Senes, J. D'Haen, J.V. Manca, R.A.J. Janssen, *Modeling the temperature induced degradation of the short circuit current in organic bulk heterojunction solar cells*, Appl. Phys. Lett. **2010**, *96*, 163301.

J. Vandenbergh, J. Dergent, B. Conings, T. Krishna, W. Maes, T.J. Cleij, L. Lutsen, J.V. Manca, D.J.M. Vanderzande, *Synthesis and characterization of water-soluble poly(p-phenylene vinylene) derivatives via the dithiocarbamate precursor route,* Eur. Polym. J. **2011**, *47*, 1827.

J. Vandenbergh, B. Conings, S. Bertho, J. Kesters, D. Spoltore, S. Esiner, J. Zhao, G. Van Assche, M.M. Wienk, W. Maes, L. Lutsen, B. Van Mele, R.A.J. Janssen, J.V. Manca, D.J.M. Vanderzande, *Thermal stability of poly-2-methoxy-5-(2'-phenylethoxy)1,4-phenylenvinylene (MPE-PPV):fullerene bulk heterojunction solar cells*, Macromolecules **2011**, *44*, 8470.

§ *L. Baeten, *B. Conings, H.-G. Boyen, J. D'Haen, A. Hardy, J.V. Manca, M.K. Van Bael, *Towards efficient hybrid solar cells based on fully polymer infiltrated ZnO nanorod arrays*, Adv. Mater. **2011**, *23*, 2802.

§ B. Conings, L. Baeten, H.-G. Boyen, D. Spoltore, J. D'Haen, L. Grieten, P. Wagner, M.K. Van Bael, J.V. Manca, *Influence of interface morphology onto the photovoltaic properties of nanopatterned ZnO/Poly(3-hexylthiophene) hybrid solar cells. An impedance spectroscopy study*, J. Phys. Chem. C **2011**, *115*, 16695.

§ *L. Baeten, *B. Conings, J. D'Haen, C. De Dobbelaere, A. Hardy, J.V. Manca, M.K. Van Bael, *Tuning the dimensions of ZnO nanorod arrays for application in hybrid photovoltaics*, ChemPhysChem **2012**, DOI: 10.1002/cphc.201200102.

*L. Baeten, *B. Conings, J. D'Haen, A. Hardy, J.V. Manca, M.K. Van Bael, *Fully water processable hybrid metal oxide nanorods:polymer solar cells*, under review.

§ B. Conings, L. Baeten, H.-G. Boyen, D. Spoltore, M.K. Van Bael, J.V. Manca, *Generalized approach to the description of recombination kinetics in photovoltaics – extending from fully organic to hybrid solar cells*, under review.

§ B. Conings, L. Baeten, H.-G. Boyen, J. D'Haen, M.K. Van Bael, J.V. Manca, *Relation between morphology and recombination kinetics in nanostructured hybrid solar cells*, submitted.

§ B. Conings, H. Yin, M. D'Olieslaeger, J.V. Manca, H.-G. Boyen, *Impact of photoelectron current on the determination of energy level alignment at ZnO/P3HT interfaces - a photoemission study*, in preparation.

L. Grieten, S.D. Janssens, M. Saitner, B. Conings, J.V. Manca, H.-G. Boyen, K. Haenen, P.Wagner, *Probing the electrochemical properties of diamond grown with various [C/H]-ratio's*, in preparation.

Conference contributions

Oral presentations

* presenter

*L. Baeten, C. De Dobbelaere, B. Conings, J. D'Haen, H. Van den Rul, J. Mullens, A. Hardy, M.K. Van Bael, *Influence of a seed layer on growth of ZnO nanorods*, 10de Vlaams Jongerencongres van de Chemie (VJC10), 01.03.2010 - 02.03.2010, Blankenberge, Belgium.

*L. Baeten, B. Conings, H. Van den Rul, J. D'Haen, J.V. Manca, J. Mullens, A. Hardy, M.K. Van Bael, *Parameter influence on the synthesis of ZnO nanorods for use in photovoltaic devices*, Innovation for Sustainable Production (i-SUP) 2010, 18.04.2010 - 21.04.2010, Brugge, Belgium.

*L. Baeten, B. Conings, H.-G. Boyen, J. D'Haen, A. Hardy, J.V. Manca, M.K. Van Bael, *Efficient hybrid solar cells based on fully polymer infiltrated ZnO nanorods*, Materials Research Society (MRS) Spring Meeting 2011, 25.04.2011 - 29.04.2011, San Francisco, US.

*B. Conings, L. Baeten, L. Grieten, P. Wagner, H.-G. Boyen, M.K. Van Bael, J.V. Manca, *Investigating the influence of polymer and interface morphology in ZnO/P3HT solar cells by impedance spectroscopy,* Materials Research Society (MRS) Spring Meeting 2011, 25.04.2011 - 29.04.2011, San Francisco, US.

L. Baeten, * B. Conings, H.-G. Boyen, J. D'Haen, A. Hardy, J.V. Manca, M.K. Van Bael, *Towards efficient hybrid solar cell based on nanostructured metal-oxides*, 2nd European Energy Conference, 17.04.2012 - 20.04.2012, Maastricht, The Netherlands.

*B. Conings, L. Baeten, H.-G. Boyen, D. Spoltore, M.K. Van Bael, J.V. Manca, *Impedimetric probing of recombination kinetics in ZnO nanorod array/poly(3-hexylthiophene) solar cells*, Hybrid and Organic Photovoltaics conference 2012, 06.05.2012 - 09.05.2012, Uppsala, Sweden.

*B. Conings, H. Yin, M. D'Olieslaeger, H.-G. Boyen, J.V. Manca, *Revealing the electronic structure at the donor-acceptor interface in P3HT/ZnO hybrid solar cells*, International Conference on Science and Technology of Synthetic Metals (ICSM) 2012, 08.07.2012 - 13.07.2012, Atlanta, US.

Poster presentations

L. Baeten, B. Conings, H.-G. Boyen, J. D'Haen, A. Hardy, J.V. Manca, M.K. Van Bael, *Optimization of hybrid solar cells based on fully polymer infiltrated ZnO nanorods*, Electroceramics XII, 20.06.2011 - 23.06.2011, Stockholm, Sweden.
**** Best poster, category "Nanomaterials" ****

L. Baeten, B. Conings, H.-G. Boyen, J. D'Haen, A. Hardy, M. D' Olieslaeger, J.V. Manca, M.K. Van Bael, *From nanostructured metaloxides towards efficient hybrid solar cells*, European Materials Research Society (EMRS) Fall Meeting 2011, 19.09.2011 - 23.09.2011, Warsaw, Poland.

L. Baeten, B. Conings, H.-G. Boyen, J. D'Haen, A. Hardy, J.V. Manca, M.K. Van Bael, *From nanostructured metal oxides to efficient hybrid solar cells*, Photovoltaics at the Nanoscale, 24.10.2011 - 28.10.2011, Hasselt University, Belgium.

B. Conings, L. Baeten, L. Grieten, P. Wagner, H.-G. Boyen, M.K. Van Bael, J.V. Manca, *Investigating the influence of polymer and interface morphology in ZnO/P3HT solar cells by impedance spectroscopy,* Photovoltaics at the Nanoscale, 24.10.2011 - 28.10.2011, Hasselt University, Belgium

**** Best poster, awarded by Agfa ****

B. Conings, L. Baeten, H.-G. Boyen, Donato Spoltore, A. Ethirajan, P. Wagner, M.K. Van Bael, J.V. Manca, *Engineering the interface between P3HT and ZnO nanorod arrays by intermediate molecular layers for photovoltaic applications*, Materials Research Society (MRS) Fall Meeting 2011, 28.11.2011 - 02.12.2011, Boston, US.

Table of contents

Abbreviations and symbols

AFM	Atomic Force Microscopy
AM1.5	Air Mass 1.5
at%	atomic percentage
BF-TEM	Bright Field Transmission Electron Microscopy
BHJ	bulk heterojunction
CELIV	Charge Extraction in a Linear Increasing Voltage
CPE	Constant Phase Element
CT	Charge Transfer
d	active layer thickness
DL	dense layer
DSSC	Dye-Sensitized Solar Cell
e	elementary charge
EBL	electron blocking layer
EJ	exajoule = 10^{18} J
EQE	External Quantum Efficiency
eV	electronvolt
FF	fill factor
HBL	hole blocking layer
HMT	hexamethylenetetramine
HOMO	Highest Occupied Molecular Orbital
HPV	Hybrid Photovoltaics
I_{sc}	see J_{sc}
ITO	tin-doped indium oxide
J_{sc}	short-circuit current
LUMO	Lowest Unoccupied Molecular Orbital
n	charge carrier density
n_{corr}	charge carrier density per unit heterojunction area
NR	nanorods

OBHJ	Organic Bulk Heterojunction
OPV	Organic Photovoltaics
P3HT	poly(3-hexylthiophene-2,5-diyl)
PCBM	1-(3-methoxycarbonyl)propyl-1-phenyl-[6,6]-methano fullerene
PEDOT-PSS	poly(3,4-ethylenedioxythiophene) poly(styrenesulfonate)
PET	polyethylene terephthalate
PV	photovoltaic(s)
SEM	Scanning Electron Microscopy
sun	illumination power divided by 1000 Wm^{-2}
TEM	Transmission Electron Microscopy
T_m	melting temperature
TPC	Transient Photocurrent
TPV	Transient Photovoltage
UPS	Ultraviolet Photoelectron Spectroscopy
UV-Vis	Ultraviolet-Visible (spectroscopy)
VBM	valence band maximum
V_{oc}	open-circuit voltage
X-SEM	Cross-sectional Scanning Electron Microscopy
XPS	X-ray Photoelectron Spectroscopy
XRD	X-ray Diffraction
Z	impedance
$Zn(OH)_2$	zinc hydroxide
$ZnAc_2$	zinc acetate
ZnO	zinc oxide
η	power conversion efficiency
μ_h	hole mobility
τ	time constant
τ_n	charge carrier lifetime
$\tau_{\Delta n}$	small perturbation carrier lifetime
ϕ	work function
ω	angular frequency

Chapter 1

Introduction

ABSTRACT

This first chapter opens by briefly situating solar energy in the context of global energy supply, setting it side by side with other renewable energy sources. A short history of photovoltaic technologies is presented, eventually evidencing the relevance of hybrid solar cells, the scope of this thesis. The state of the art of different types of hybrid solar cells is discussed, as well as basic conceptions regarding their working principles. Finally, the aim of this thesis is described, together with a guide to the papers included in the following chapters.

1.1. The intrigue of solar energy

Industrialization has triggered an enormous escalation of global energy demand, and there is no stagnation in sight. To this end, the earth's fossil resources are being exploited (or squandered in many cases) to such an extent that they will run dry in only a few decades. In 1990, globally 373 EJ was consumed, and assuming a business-as-usual scenario, by 2035 we would need over 800 EJ.[1] Considering that tempering mankind's greediness for energy presents in all likelihood an even more daunting task than finding more fossil energy resources in the first place – provided that there are any left – logic dictates that we should invest in harvesting sustainable energy. There are plenty of possibilities to choose from. Well-known examples are hydro energy, geothermal energy, wind energy, bioenergy, tidal energy and (where also the three latter options actually originate from), solar energy. Calculations made by the German Advisory Council on Global Change show that in theory the future must indeed be looking bright. Figure 1.1 (top) shows that all available sustainable power represents the 3078-fold of what we need today, the sun being responsible for 93% of this figure. Despite the plain technological and practical limits to the fraction hereof which is eligible for exploitation, the actual attainable sustainable power at this very instant is about 6 times the required quantity, the sun amounting for 3.8 times in this case Figure 1.1 (bottom). Comparing the several indicated options, it is clear that solar energy has the greatest potential in "harvestable availability" and, while most of the indicated energy sources are a product of solar energy, the amount of available power from each of them suffers in comparison with solar irradiation itself. This does not mean that all research efforts should deflect in this direction, though. Solar energy also has its own drawbacks, such as discontinuous operability. For example, it could make more sense to power a factory near the coast with continuously available tidal energy. Accordingly, it is well accepted that, on the long run, a wide range of appropriate renewable energy sources will be available to serve a wide range of specific applications. In this respect, solar energy can be put to use in three main forms with different (de-)localization properties. A rather localized possibility is solar chemical power, which is a collective noun for processes that harness solar energy to drive a chemical reaction to produce so-called solar fuels, for example the splitting of

water into oxygen and hydrogen. Solar thermal energy may be used directly to produce hot water by collectors on rooftops (delocalized), or to drive a heat engine, for example in a concentrated solar power plant (localized). Finally, the third main option and probably the most flexible one (localized and delocalized), is the conversion of sunlight into electricity, the field in which lies the scope of this thesis.

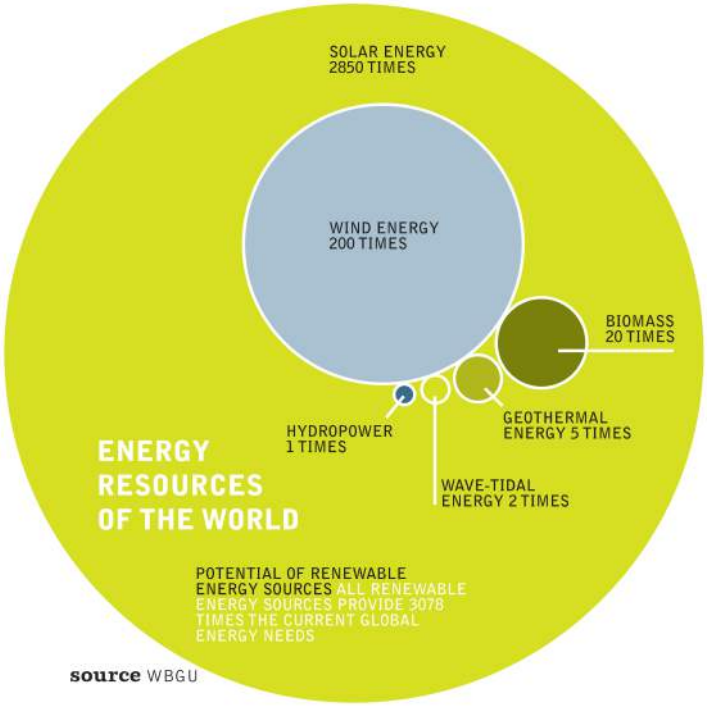

THE AMOUNT OF POWER THAT CAN BE ACCESSED WITH CURRENT TECHNOLOGIES SUPPLIES A TOTAL OF 5.9 TIMES THE GLOBAL DEMAND FOR POWER

Sun	3.8 times
Geothermal heat	1 time
Wind	0.5 times
Biomass	0.4 times
Hydrodynamic power	0.15 times
Ocean power	0.05 times

source DR. JOACHIM NITSCH

Figure 1.1. (top) Available renewable energy, compared with the actual global energy need. (bottom) Amount of power that can be accessed with current technologies, compared with the actual need. (reprinted from [2])

1.2. Photovoltaic technologies: past, present and future in a nutshell

The concept of using the energy of the sun to produce electricity might not sound as an ancient idea. Nevertheless, its origin brings us back to 1839 when Alexandre Edmond Becquerel discovered the photovoltaic effect: the creation of voltage or electric current in a material upon exposure to light. In 1877, William G. Adams and Richard E. Day observed the photovoltaic effect in selenium. Then, in 1883, the American inventor Charles Fritts managed to fabricate the world's first working solar cell, based on selenium, which had an efficiency of about 1% (i.e. 1% of the incoming light power is converted into electric power). It was not until 1954 that Bell Labs came up with the first modern silicon solar cell (6% efficient), the direct ancestor of the solar cells mostly found in solar panels today, and still having the largest market share.[3] Many technological advances have lead to the Si solar cell attaining lab efficiencies up to 25% today, which is close to the theoretical maximum of just over 30% for this material in a single junction configuration, as calculated by William Shockley and Hans Queisser in 1960.[4] Over the years, many different technologies and materials have been developed in parallel. Figure 1.2 contains a timeline that is released on a regular basis by the National Renewable Energy Laboratory (NREL), depicting the progress of record cell efficiencies for all current photovoltaic technologies. The efficiency is obviously an important criterion for the potential success of a particular technology, but there are two equally critical ones: reliability and production cost. While the popular Si solar cells score high marks on efficiency and reliability, their fabrication entails a cumbersome series of processes, leading to a high price per produced Watt of power.[5] Although research efforts in Si-based photovoltaics are nowadays directed to cheaper production rather than efficiency enhancement, policy makers still need to implement feed-in tariffs to stimulate the use of solar energy to the masses. In that respect, compelling alternatives for Si – or other inorganic – solar cells are organic solar cells (OPV).[5, 6] Eventually owing to Alan J. Heeger, Alan G. MacDiarmid and Hideki Shirakawa who discovered the possibility to synthesize semiconducting polymers in 1977, the concept of the organic solar cell as we know it today was introduced in the 1990s.[7, 8] The main selling point of OPV is that

they can be entirely solution deposited. This way, they could be cheaply produced much like a newspaper is printed, where the paper is replaced by a transparent flexible substrate, and the ink contains the active light-absorbing material.[9-11] Even electrodes (metallic or transparent) can be printed within the same effort.[12, 13] Despite the obvious benefit of solution processing, evaporation of small molecules has also proven to be a viable alternative.[14] Unfortunately these organic solar cells are not yet as efficient as their inorganic counterparts, nor are they very durable yet.

An efficiency of 10% is considered as the minimum requirement for commercial viability of OPV technology.[11] It is however not uncommon for photovoltaic technologies to exhibit a lower performance in their manufactured form as compared to laboratory performance. Where the ratio of production versus laboratory performance is about 65% for Si photovoltaics, this ratio so far is only half for organic photovoltaics. Recently, 10% OPV efficiency was claimed by Mitsubishi Chemicals but module efficiencies today in general are not higher than 3%.[5] Nevertheless, considering the progress indicated in Figure 1.2 and from theoretical efficiency prospects, inferior performance of OPV as compared to Si PV will be a temporary problem.[15]

A second hurdle for OPV to become a contender in the renewable energy market is durability. Organic solar cells typically consist of a blend of a semiconducting polymer and a fullerene (buckyball) derivative, being intimately mixed. Temperature-driven phase separation causes degradation due to the loss of intimate contact between these components.[16, 17] To tackle this problem, organic/inorganic solar cells (or "hybrid photovoltaics", HPV) pose an eligible alternative. Where in case of OPV the adjacent fullerene molecules can diffuse across the flexible polymer chains, in HPV these are replaced with a solid inorganic phase, providing a rigid backbone, *ergo* more stable morphology. So far, HPV are still less efficient than OPV, simply because the concept is younger and less mature.

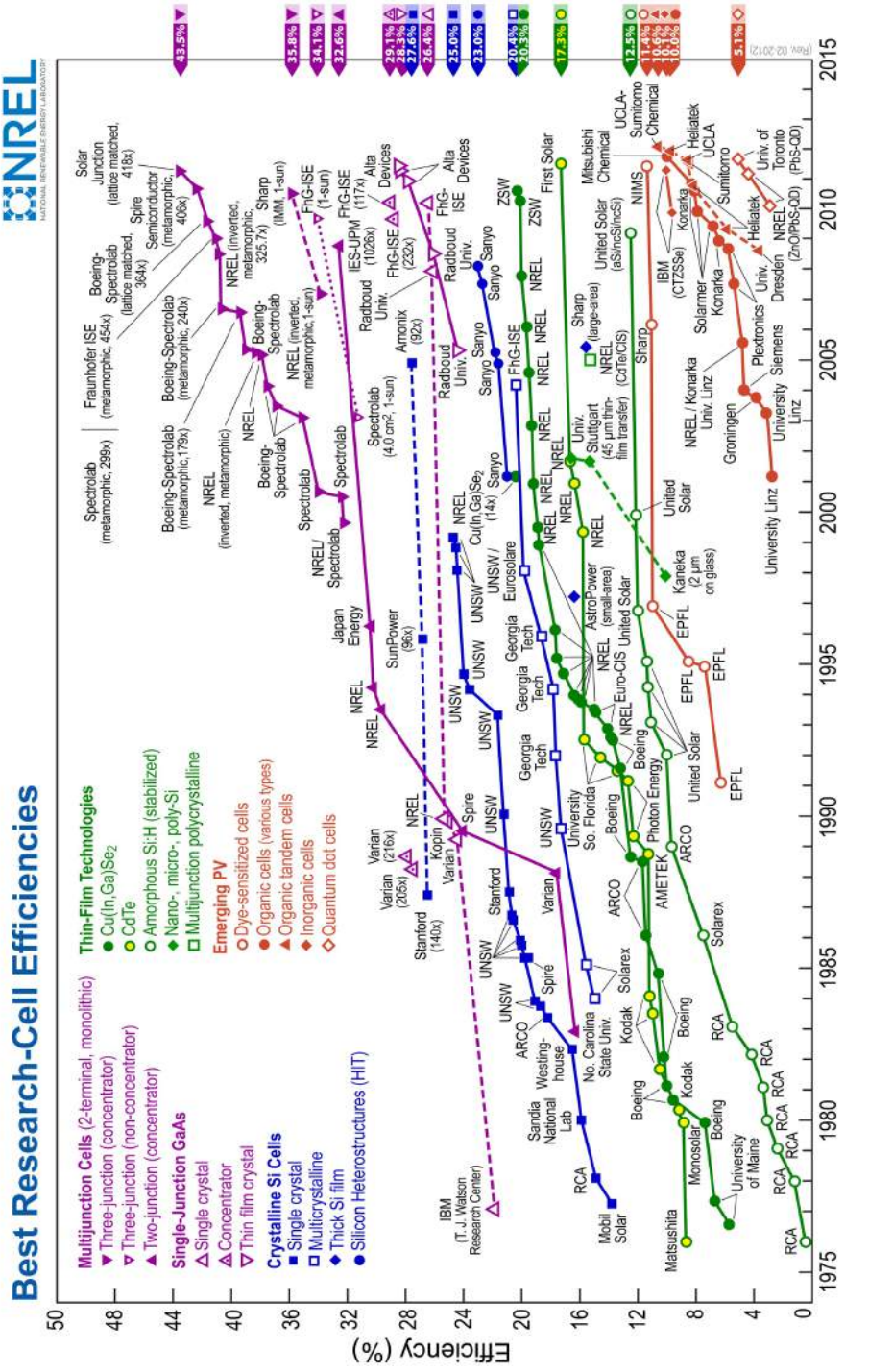

Figure 1.2. Efficiency comparison of current photovoltaic technologies. (NREL).

1.3. Excitonic solar cells

1.3.1. Basic working principle

A energetic picture of the basic working principle of organic and hybrid solar cells is given in Figure 1.3, broken up into consecutive events. For simplicity, the energy levels are drawn as for the individual materials, not showing energy level alignment or band bending between one another. The efficiency η of each of the steps represents a number between 0 and 1. Successful operation of a solar cell hinges on all values of η being as close to 1 as possible. The overall photon-to-electron conversion efficiency, also referred to as external quantum efficiency (EQE) is then given by:

$$\mathrm{EQE}(\lambda, \mathrm{V}) = \eta_{\mathrm{A}} \cdot \eta_{\mathrm{diff}} \cdot \eta_{\mathrm{diss}} \cdot \eta_{\mathrm{tr}} \cdot \eta_{\mathrm{cc}} \quad (1.1)$$

Where λ is the wavelength of the incident light and V the applied voltage across the device.[18]

Absorption (Figure 1.3a) Upon illumination, photons with energy larger than the bandgap of the donor excite electrons from the donor's highest occupied molecular orbital (HOMO) to its lowest unoccupied molecular orbital (LUMO), thus creating bound electron-hole pairs or excitons. η_A represents the fraction of the incoming photons absorbed in the active layer. This relies in the first place on a high absorption coefficient of the absorbing polymer. While most conjugated polymers fulfill this requirement with ease (in case of poly(3-hexylthiophene) (P3HT, see Figure 1.4) it is possible to absorb all the light in a thin film of ~200 nm), a bottleneck in this respect lies in the spectral mismatch between polymer absorption and solar irradiation. The bandgap of P3HT is about 1.9 eV, so only a modest fraction of the solar spectrum can be absorbed. Recently, lower bandgap polymers are being investigated with success, but competing with the absorption of Si (bandgap 1.1 eV) remains a challenge.[19, 20] A promising strategy to create a larger absorption window is to stack several active layers with complementary absorption spectra in a tandem device.[21]

Exciton diffusion (Figure 1.3b) Within its lifetime (typically several 100's of ps[22]), an exciton can travel a short distance, depending on the host material, typically somewhere between 5 and 20 nm.[22-25] If an exciton does not separate into an electron and a hole within this lifetime, it eventually recombines by emitting a photon

or it decays via thermalization.[26] For an exciton to contribute to the photocurrent, it has to reach a donor-acceptor interface first, were it can eventually split (see below). η_{diff} is the exciton diffusion yield, or, the fraction of excitons that succeeds in reaching a donor-acceptor interface without falling victim to so-called geminate recombination.[27] The most straightforward manner to maximize η_{diff} from a physical point of view is to reduce the average donor-acceptor distance to an appropriate value.

Exciton dissociation (Figure 1.3c) Once the exciton has reached a donor-acceptor interface, it can enter a charge transfer (CT) state where the hole remains in the HOMO of the donor material and the electron is located at the conduction band of the acceptor material.[28] The timescale on which this charge transfer takes place is significantly smaller than the timescale of recombination, rendering the CT state a metastable state. Eventually, the potential gradient between donor and acceptor causes dissociation of the exciton, enabling the free charges to start drifting to their respective electrodes. η_{diss} gives the ratio of the number of excitons that enter the CT state to the total number of excitons at donor-acceptor interfaces. η_{diss} can be increased by increasing the potential difference between the donor's LUMO and the acceptor's electron affinity.

Charge transport (Figure 1.3d) During the journey towards the electrodes, impurities, structural defects, as well as unfavorable percolation pathways and cul-de-sacs, can cause charge carriers to become trapped and to recombine (non-geminate recombination). This affects the transport efficiency η_{tr}, the ratio of the number of free charges transported to the electrodes to the number of excitons dissociated at the donor-acceptor interface. η_{tr} can be optimized by introducing higher mobility materials and increased order in the active layer morphology.

Charge collection (Figure 1.3e) η_{cc} is the charge collection yield, which is the portion of charges collected at the electrodes compared to the charges that reach the electrodes without recombining. η_{cc} is 1 for Ohmic contacts.

After passing an external load, lowering their energy, the charge carriers are re-injected in the device, and the entire process reinitiates.

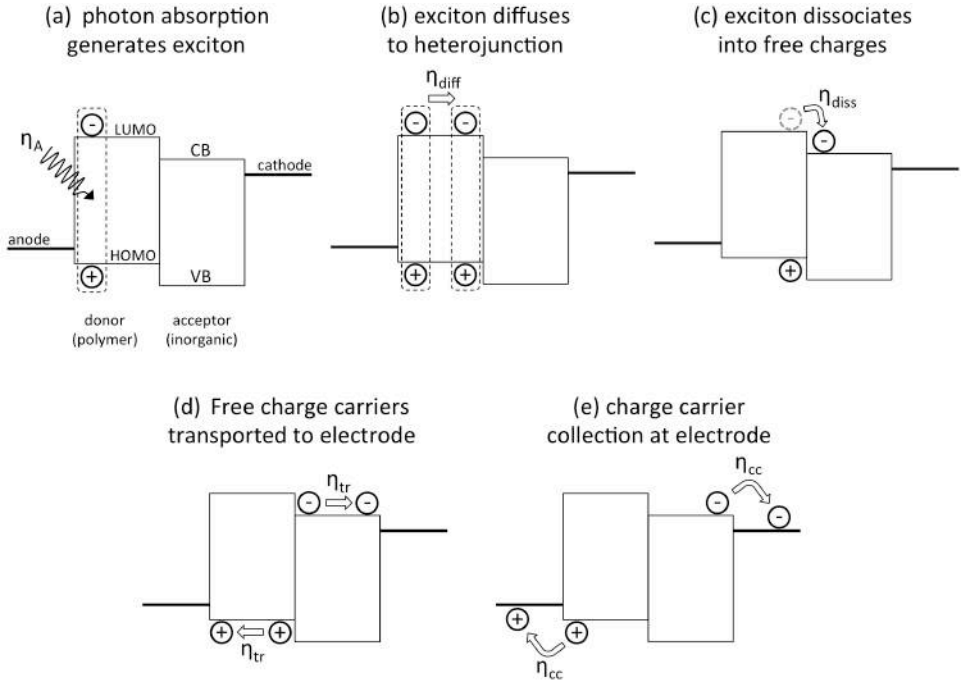

Figure 1.3 Consecutive steps for photocurrent generation in an excitonic solar cell. (adapted from [18])

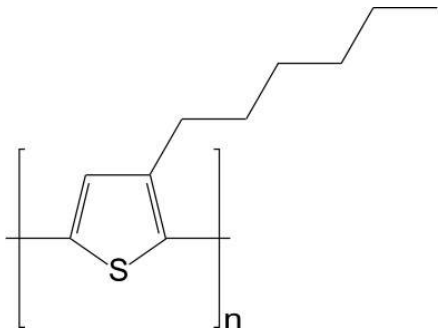

Figure 1.4. Chemical structure of poly(3-hexylthiophene).

1.3.2. Recombination

Because of is relevance in this thesis, the process of recombination is now concisely elaborated on. As can be deduced from the previous section, recombination occurs in two forms: geminate and non-geminate recombination.[29] This classification is

straightforward: whenever two charge carriers recombine that originate from the same parent exciton, this is designated as geminate recombination, whereas recombination involving two previously unrelated carriers is referred to as non-geminate recombination. In practice it is assumed that all recombination events prior to exciton dissociation are by definition geminate and, naturally, after dissociation every recombination event is non-geminate. The order of recombination depends on the number of participants, which introduces another type of classification: monomolecular (1st order) or bimolecular (2nd order) recombination (higher order is improbable in this context).[29] Geminate recombination is monomolecular because the two constituents originate from the same exciton. Two mobile and independent charge carriers recombining are doing so bimolecularly. Up to now it might seems that non-geminate and bimolecular recombination are synonyms, however, the following subtlety illustrates the contrary: recombination of a mobile charge carrier with a trapped carrier is monomolecular, despite the participation of two constituents, provided that the trapped charges clearly outnumber the mobile ones, whereas in case of a similar concentration of trapped and mobile charges, this recombination is bimolecular (this last case is denoted as Shockley-Read-Hall (SRH) recombination).

In this work, recombination-related topics will consider only non-geminate recombination. Charge carrier dynamics are given by the continuity equation:

$$\frac{\mathrm{d}n}{\mathrm{d}t} = -\frac{1}{q}\frac{\mathrm{d}j_n}{\mathrm{d}x} + G - R \tag{1.2}$$

with n the electron concentration, $\mathrm{d}j_n/\mathrm{d}x$ the spatial derivative of the electron current, G the optical generation rate, and R the recombination rate. In this equation, R is of the form:

$$R = k(np - n_i p_i) \tag{1.3}$$

with n and p the electron and hole concentrations, n_i and p_i the intrinsic carrier concentrations, and k the recombination constant. Because electroneutrality is assumed, and the second term is small compared to the first, the equation is mostly used as

$$R = kn^2 \tag{1.4}$$

Recombination constant *k* can take different forms, depending on the device and/or material system being considered. For example, for free charges in low-mobility materials, Langevin-type recombination is expected, for which

$$k = \frac{e}{\varepsilon_r \varepsilon_0}(\mu_e + \mu_h) \quad (1.5)$$

where *e* is the elementary charge, $\varepsilon_r\varepsilon_0$ the effective dielectric constant, μ_e and μ_h the electron and hole mobilities. In practice, an additional factor is needed to appropriately describe the charge carrier dynamics, which is thought to originate from the fact that the charge carriers are spatially separated, each species residing on their corresponding side of the heterojunction and only being able to recombine at the interface. Another suggested cause is that the minimum of the mobilities in Equation 1.5 is relevant, instead of the sum.[30] For P3HT:PCBM solar cells, it was experimentally found that the *k* is dependent on *n*, following the emperical formula:

$$k = \frac{n^{\lambda-1}}{(1+\lambda)\tau_{\Delta n_0} n_0^{\lambda}} \quad (1.6)$$

where λ, n_0 and $\tau_{\Delta n_0}$ are experimentally determined constants.[31]

1.3.3. Basic characterization

The most straightforward and easy-to-judge characterization of a solar cell is the current voltage (J-V)-curve. It can be easily acquired by varying the voltage across the cell while measuring the current under illumination, resulting in a curve like in Figure 1.5. Two important parameters on such a curve are the short-circuit current density J_{sc} and the open-circuit voltage V_{oc}. J_{sc} is simply the current flowing at zero voltage. The definition of V_{oc} can be rather deceptive. While the term open-circuit leads to the impression that no current is flowing and its value should thus be fully dependent on the position of the energy levels within the device, the V_{oc} as designated in a solar cell is the voltage at which the sum of photocurrent and loss current exactly compensate each other.

The conversion efficiency η is given by the ratio of the extracted power to the incident light power. The maximum output power P_{out} that can be drawn is defined by the double-shaded area in Figure 1.5, which equals the product of what is referred to as J_{max} and V_{max} (the "maximum power point" MPP).

$$\eta = \frac{P_{out}}{P_{light}} = \frac{J_{max}V_{max}}{P_{light}} \quad (1.7)$$

Or, alternatively,

$$\eta = \frac{J_{sc}V_{oc}FF}{P_{light}} \quad (1.8)$$

Where *FF* is the fill factor, which is the ratio between the single and the double-shaded areas:

$$FF = \frac{J_{max}V_{max}}{I_{sc}V_{oc}} \quad (1.9)$$

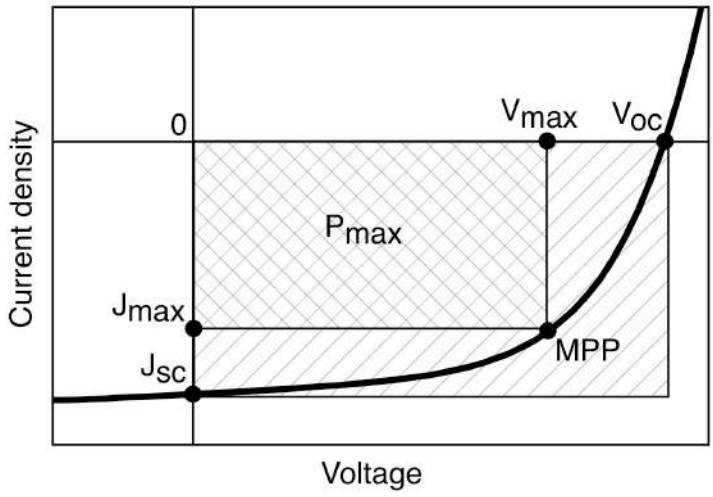

Figure 1.5. (J-V)-curve of a solar cell.

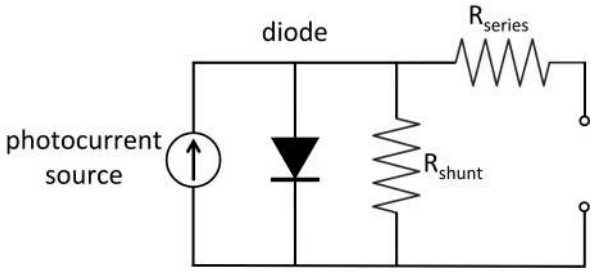

Figure 1.6. Traditional equivalent circuit of a solar cell.

A convenient way to understand the basic shape of the J-V curve, and therefore also *FF*, is the equivalent electrical circuit in Figure 1.6. It considers the J-V behavior to consist of four parts: a photocurrent source, a diode, a series resistor and a shunt

resistor. The photocurrent source is simply the representation of converting absorbed photons to free charges that can be collected by the contacts, the diode stands for the electron-hole recombination at the donor-acceptor junction, the series resistor R_{series} accounts for the combined internal resistance (slope near V_{oc}) and the parallel resistor R_{shunt} models leakage currents through, e.g., pinholes (slope near J_{sc}).[32] From this model, it is clear that the combination of a low R_{series} and a high R_{shunt} generate a nearly ideal diode-shaped curve, and that undesirable phenomena affecting these resistances are visible in the shape of the J-V curve. However, it should be stressed that this traditional model is very basic, and there are many factors that can have an influence on the values of these resistances.[32] For this reason, complex models have been developed that take into account more parameters.[33-35]

1.3.4. Towards the optimal device morphology

The first photovoltaic device setup that made use of organic material was very simple: the light absorbing organic film was sandwiched between two electrodes. Bearing in mind section 1.3.1, it is clear that this concept could only yield very modest efficiencies. Since there is no heterojunction, the (Coulombically bound) excitons could rely only on the electrodes' difference in work function in order to be dissociated, resulting in low performance (< 0.1 %).[36, 37] A key development was then made by Tang in 1985, who succeeded to fabricate the first two layer (or, bilayer) organic solar cell (Figure 1.7a) with an efficiency of almost 1 %.[38] The significant increase in efficiency owes to the interface between the two active layer components that promotes exciton splitting. As mentioned in section 1.3.1, the diffusion length of an exciton is typically very small (a few nm), so it is indisputable that in such a bilayer system only the excitons created within a diffusion length's distance from a donor-acceptor interface are eligible for efficient dissociation. Provided that maximum light absorption requires an active layer thickness of many times the exciton diffusion length, a new development was necessary to fully harness the organic material's light absorbing capabilities. A breakthrough came in mid 1990's, when the bulk heterojunction (BHJ) concept was introduced (Figure 1.7b).[7, 8] By blending the active layer materials in a solution, upon deposition an interpenetrating network is formed

in situ, creating a large donor-acceptor interface in the bulk of the active layer. As a consequence, excitons only have to travel for a short distance before they encounter an interface, leading to reduced recombination and thus increasing the exciton diffusion yield. On the other hand, the interpenetrating network creates sinuous pathways that are not necessarily continuous, so charge carriers have to percolate along them to find the electrodes. Numerous studies have been dedicated to the manipulation and understanding of the microstructure formed by solution casting, aiming to find the optimum morphology that combines a large heterojunction interface while still providing effortless charge transport, though obtaining accurate control presents a challenge.[34, 39-41] Nevertheless, so far efficiencies of more than 8 % have been reached using this concept.[42, 43] In contrast with the BHJ, an interesting remark is that the bilayer device setup, despite its obvious general limitations, is still being used in small-molecule based solar cells. These materials have higher absorption coefficients than polymers so they only need a very thin layer to absorb most of the light. The top efficiencies today from this kind of devices are comparable with polymer-based OPV.[14, 44]

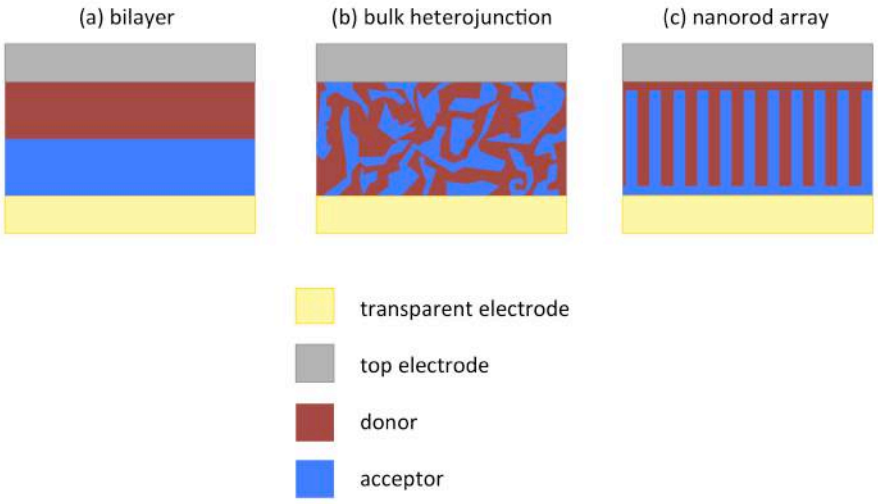

Figure 1.7. Different types of donor-acceptor morphology.

The holy grail in heterojunction morphology is depicted in Figure 1.7c. An array of elongated structures incorporates both the large interface interfacial area and straight

pathways to the electrodes. Successful efforts to create this type of heterojunction from organic materials usually entail the application of surface patterning, but the technique has limited potential as it can only create quite wide and shallow structures that do not classify as nanorod arrays.[45-47] Hybrid solar cells based on the nanorod array morphology are more accessible, though they have their own specific intricacies, as is the scope of this thesis.

1.3.5. Hybrid solar cells: state of the art

1.3.5.1. Dye-sensitized solar cells

Although usually not considered in the context of hybrid solar cells, the dye-sensitized solar cell (DSSC) is technically also a hybrid. Thus, it has to be mentioned here, especially because it shares basic components with the other types of hybrids. The DSSC was introduced in 1991 by Brian O'Regan and Michael Grätzel, and deemed a groundbreaking novelty as the first report of this kind already announced an efficiency of nearly 8 %.[48] The basic idea is to coat a porous metal-oxide layer (electron acceptor), usually TiO_2, with a monolayer of light-absorbing dye, and infiltrate it with a liquid electrolyte (electron donor). Over the years, many studies have been conducted to reveal the basic working mechanisms, continuously overlapping chemistry and physics. Several thousands of dyes have been investigated, as well as hundreds of electrolyte systems and numerous types of mesoporous films with different morphologies and compositions.[49] The current record efficiency is 12.3 %, again obtained by Grätzel's group.[50] A major downside of DSSC is the liquid electrolyte, which tends to cause leakage and corrosion problems.[51] Solid-state electrolytes have been developed however, the most known one being spiro-OMeTAD ((2,2',7,7'-tetrakis-(N,N-di-p-methoxyphenylamine)9,9'-spirobifluorene)), but the resulting device performance (5%) is not yet equivalent with the liquid counterparts.[52, 53]

1.3.5.2. Polymer:inorganic blends

The popular fullerene derivatives that take on the role of electron acceptor in OPV, can be replaced be inorganic nanocrystals to form a polymer:nanocrystal bulk

heterojunction. Intensified research in this domain was initiated by the seminal work of Huynh et al. in 2002, that demonstrated a conversion efficiency of 2 % using a mixture of CdSe nanoparticles and P3HT.[54] Alternative nanocrystals introduced since are a.o. CdTe,[55] PbS,[56] and PbSe[57]. Advantageous about these materials it that they also contribute to light absorption, unlike most acceptors.[58] A downside of the nanocrystals is that they need ligands to keep them in solution, and even with larger ligands the solubility is limited. The ligands also induce thin insulating barriers between the nanocrystals, impeding proper charge transport. To minimize this effect, and to limit the amount of grain boundaries, elongated particles, tetrapods and branched nanostructures were shown as improvements to 1-dimensional crystals.[59-62] Dayal et al. demonstrated an efficiency of 3.2 % for tetrapod-shaped CdSe nanocrystals mixed with the low-bandgap polymer PCPDTBT.[63]

Metal oxide nanoparticles pose another possibility as electron acceptor. In 2004, Kwong et al. demonstrated an efficiency of 0.42 % for a BHJ of TiO_2 nanoparticles and P3HT.[64] Beek et al. reported the first BHJ hybrids based on ZnO nanocrystals and poly[2-methoxy-5-(3',7'-dimethyloctyloxy)-1,4-phenylenevinylene] (MDMO-PPV), with an efficiency of 1.6 %, also in 2004. In both cases, the particles were ligand-free, requiring a carefully balanced solvent to keep the particles dissolved.[65] In ligand-based syntheses, the default ligands that are often insulating can be exchanged with more favorable ones, preferably containing conjugated structures, which can lead to drastic improvements in J_{sc} and *FF*. Lin et al. managed to improve a TiO_2/P3HT BHJ solar cell from 0.38 % up to 1.7 % with a non-absorbing ligand, and up to 2.2 % using a dye as ligand.[66, 67] Notwithstanding that these results are promising, also here the problem of grain boundaries exists. A strategy to circumvent this obstacle is to mix the donor polymer with a metal oxide precursor, the latter one converting into the corresponding metal oxide upon deposition, creating *in situ* the BHJ morphology. This strategy was first demonstrated in 2002 by van Hal et al., who used a mixture of MDMO-PPV and titanium isopropoxide, giving an MDMO-PPV:TiO_2 BHJ as the precursor converts to TiO_2 upon exposure to moisture.[68] It was perfected later, using diethylzinc as a precursor to ZnO, combined with P3HT, eventually resulting in the current record efficiency of 2% by Oosterhout et al..[69] The technique promises further

improvements by manipulation of the metal oxide/polymer mixing behavior through fine-tuning of the polymer structure.[70]

1.3.5.3. Template based polymer/inorganic solar cells

For active layers cast from a donor-acceptor blend, the eventual degree of phase separation is difficult to control. Changing solvent, drying conditions, possible additives and annealing treatments, a whole range of morphologies can be accessed, though not always in the simplest fashion. An alternative and perhaps more elegant approach to morphology control is the use of an acceptor template into which the donor polymer is infiltrated (much like the electrolyte is infiltrated in the porous layer of a dye-sensitized solar cell), *ipso facto* creating a BHJ. First attempts of this kind were carried out around 2000, when Van Hal et al. and Arango et al. infiltrated the polymer 2-methoxy,5-(2'-ethyl-hexyloxy)-p-phenylenevinylene (MEH-PPV) into a porous thin layer of TiO_2.[71, 72] Later on, more investigation was being directed towards the degree of infiltration, as initiated by Coakley et al., now using P3HT instead of MEH-PPV.[73, 74] It has been shown that the structural incompatibility between TiO_2 and P3HT has electronic repercussions for the resulting solar cells.[75] The TiO_2 surface is therefore often coated with an infiltration-facilitating agent that may as well act as an additional sensitizer or interface enhancer.[76-78] In that case the term solid-state dye-sensitized solar cell is used, pointing out the analogy with the regular DSSC, only the electrolyte is replaced by a (solid state) polymer. Chang et al. reported an Sb_2S_3 modified porous TiO_2 film, infiltrated with P3HT, exhibiting an efficiency as high as 5.13 %.[77]

Porous layers mostly consist of individual particles that are sintered together, incorporating a significant number of grain boundaries, and contain inherently sinuous electron pathways, both of which are disadvantageous for charge transport.[79] It thus makes sense to strive to an improved kind of porous structure that solves both these drawbacks simultaneously: a nanorod array, which provides quasi single crystalline and direct pathways to the cathode, its side-planes accounting for the required area enlargement. So far, the application of TiO_2 nanorod arrays is almost exclusively directed towards DSSC.[80] This holds for TiO_2 nanotubes as well.[81] In

contrast to TiO_2, ZnO offers a lot more manipulability to form different kinds of nanostructures, including nanorod arrays, and has drawn plenty of interest in the field of both DSSC and polymer/inorganic solar cells.[82-84] Moreover, juxtaposing with other inorganic semiconductors, ZnO has convincing assets such as reduced toxicity and superior electron mobility.[83] In 2005, Olson et al. demonstrated the first hybrid solar cell based on ZnO nanorod arrays and P3HT, yielding an efficiency of 0.53 %.[85] As in particle-based porous layers, also for nanorod arrays the problem of insufficient infiltration is present, albeit to a smaller extent.[86] It was found that the right choice of casting solvent for the polymer and an appropriate annealing step have a major influence on infiltration.[87] Likewise the effect of ZnO processing was investigated, revealing that a mild annealing step (150°C), removing physisorbed water molecules, is beneficial for device performance.[88] It was proposed that nanorod morphology and P3HT crystallinity are the main parameters to be optimized in order to raise efficiencies beyond 0.55 %.[86] Additionally, the P3HT morphology near the interface with ZnO was identified as a cause for mediocre device performance.[89] Functionalization of the ZnO surface with organic molecules such as alkene thiols was put forward as a solution to mend this deficiency, though the approach has only been demonstrated for bilayer devices, indicating that the direction of charge transport and/or the exposed crystallographic direction has an impact on its efficacy.[90] The use of a dye as surface functionalization has been proven to improve performance, [91, 92] though almost all available dyes are designed to sensitize TiO_2 and are not optimized for the ZnO surface regarding attachment and electron injection.[93]

Envisioning the application of nanorods as highways for charge carriers, efforts were also taken to infiltrate the organic blend P3HT:PCBM into nanorod arrays. While abundant successful devices had already been fabricated with this blend,[94] nanorod arrays were expected to improve the performance even further by enhancing the long-range charge transport. Although this antenna effect was demonstrated to occur, nominally no gain in efficiency was made compared to state-of-the-art P3HT:PCBM devices.[95, 96]

1.4. Aim of the thesis

From the previous section one can safely conclude that with the potential that comes with each type of hybrid solar cells, a downside is present as well. Classical dye-sensitized solar cells suffer from problems induced by their liquid electrolyte. The fabrication of organic/inorganic blends is not straightforward regarding morphology control, and solubility issues limit the options for further improvements. *In situ* formation of a metal-oxide/polymer BHJ, deposited from a metal-oxide precursor/polymer blend, is promising but also here it remains a challenge to control the microstructure. Due to infiltration issues, polymer filling of a porous inorganic layer is tricky, but becomes manageable by introducing a surface functionalization. In that sense, filling of a more open structure such as a nanorod array should be more convenient. It is worthwhile to investigate this device type, as it is a promising alternative to fully organic ones because of its inherent morphological stability, owing to the rigid structure of the inorganic phase. However, despite its apparent potential, the obtained efficiencies so far are still quite low compared to OPV.

This thesis aims to improve the efficiency of hybrid solar cells based on ZnO nanorod arrays and P3HT, and to understand the mechanisms that govern the improvement. Three main research questions are central in this work.

(i) How do morphological variations in both the ZnO phase and the polymer phase influence the device performance?

(ii) Is the recombination behavior of these solar cells comparable with fully organic ones and how does it relate to the morphology-dependent performance variation?

(iii) What is the role of the ZnO/P3HT interface in the operation of the corresponding solar cell?

1.5. Guide to the chapters

Chapters 2 to chapter 7 each represent a paper that was written in the framework of this PhD study.

First of all it has to be pointed out that all chemical aspects and optimizations regarding the synthesis of ZnO nanorod arrays used in this work were fully carried out by Linny Baeten, in the framework of her PhD in the research group Inorganic and Physical Chemistry of Hasselt University.

Chapter 2 describes the optimization of ZnO nanorod array/P3HT solar cells *via* the variation of morphological parameters. The nanorod length is varied to find the optimal trade-off between light absorption and charge transport, and blocking layer thicknesses are optimized. X-ray photoelectron spectroscopy is used to acquire a compositional depth profile of the device in order to investigate the extent of infiltration upon thermal treatment.

Chapter 3 further examines the consequences of morphological tailoring on device performance, the emphasis now lying in the nanorod diameter and spacing. The paper commences with a chemical part regarding the nanorod array synthesis, which is actually in scope of Linny Baeten's PhD study, but it is included for the sake of completeness.

Chapter 4 introduces impedance spectroscopy as a powerful analysis tool to pinpoint the consequences of processing conditions on device performance. By varying several device properties, their corresponding signature in the impedance spectrum can be identified, allowing to establish an equivalent circuit model for the solar cell. Furthermore, the model is used to examine the interfacial polymer behavior upon thermal treatment during device fabrication.

To improve the metal-oxide/polymer hybrid solar cell in a systematic way, a thorough comprehension of its recombination kinetics is indispensable. In Chapter 5, the impedimetric knowledge from Chapter 4 is applied to probe specifically this aspect. For OPV it was evidenced that the main loss mechanism that limits its performance is non-geminate recombination. A model that was recently introduced to support this statement is now revisited for our hybrid solar cells, authenticating the mutual equivalency of both device types concerning dynamics of recombination.

Based on Chapter 5, the influence of morphological parameters on recombination kinetics is investigated in Chapter 6, making use of the nanorod and P3HT tailoring described in Chapters 2 and 3. Charge carrier densities are expressed in terms of the effective interfacial donor-acceptor area, exploiting the ZnO/P3HT compound as model for pure two-phase systems, and enlightening its usefulness toward recombination studies for OPV as well. Furthermore, a remarkable influence of nanorod array alignment on device performance, as described in Chapter 3, is further examined regarding recombination.

Chapter 7 reports an experimental study of the electronic structure at the P3HT/ZnO interface by means of photoelectron spectroscopy, intending to shed more light onto the alignment/coupling of electronic states between the two materials. In contrast to previous work based on sputter-deposited ZnO films, we now use ZnO single crystals to ensure well-defined surfaces/interfaces. Serious deficiencies in the analysis of related work in literature are revealed regarding electronic parameter determination of these (non-metallic) materials, and a new appropriate methodology is established.

Finally, Chapter 8 concisely summarizes all results from this work and uses them as a leading edge towards recommendations for future research, these being illustrated with preliminary results.

Chapter 2

Towards efficient hybrid solar cells based on fully polymer infiltrated ZnO nanorod arrays

*L. Baeten, *B. Conings, H.-G. Boyen, J. D'Haen, A. Hardy, J. V. Manca, M. K. Van. Bael, *Adv. Mater.* **2011**, *23*, 2802.

ABSTRACT

A significantly improved efficiency is achieved for solar cells based on hydro-thermally grown ZnO nanorods and P3HT. This efficiency is obtained by fine-tuning morphological parameters and by adding electron and hole blocking layers. Insight into the mechanisms underlying the improvement lead to recommendations for further future improvements.

2.1. Introduction

Hybrid photovoltaic devices based on heterojunctions of nanostructured metal oxides and conjugated polymers are attracting great scientific interest as low cost and up-scalable alternatives for conventional photovoltaics.[97] Although dye-sensitized solar cells are still the most efficient metal oxide based solar cells,[48, 98] the presence of a liquid electrolyte induces leakage and corrosion which harms the long term performance and stability.[99, 100] The introduction of solid state hybrid solar cells offers an alternative approach to overcome these drawbacks by replacing both the dye and the electrolyte by a single polymer that acts as a hole conductor and absorber.[101] Until now, hybrid solar cells based on ZnO nanorods and poly-(3-hexylthiophene-2,5-diyl) (P3HT) have reached maximum efficiencies up to 0.55 %.[86, 102-104] Here, we demonstrate a significantly improved efficiency of 0.74 % ± 0.02 % for hydrothermally grown ZnO nanorods and P3HT. We show that tuning the crystalline quality of the polymer in combination with optimized hole and electron blocking layers are mainly responsible for the achieved progress.

Due to the short exciton diffusion length in conjugated polymers (~10 nm), an intimate intermixing with the acceptor material is crucial. In that sense the bulk heterojunction (BHJ) solar cell, in which the photoactive layer is deposited from one solution that contains both donor and acceptor, is known to be particularly successful. The best BHJ of ZnO and P3HT so far demonstrates an efficiency of 2 %.[69] However, properly balancing photogeneration and charge carrier percolation remains an issue, as the morphology of the inorganic matrix is difficult to control during synthesis.[69] In this work, the morphology of the active layer can be controlled prior to polymer deposition by manipulating the morphological properties of the metal oxide structure. The ZnO nanorods then serve as an n-type semiconductor with high electron mobility due to their single crystalline morphology,[105] thereby avoiding grain boundary scattering of electrons as seen in, e.g., nanoparticle based porous layers.[106] Hence, electron transport in such wires is expected to be several orders of magnitude faster than percolation through a random polycrystalline network.[107] From a chemical point of view, the solution-based hydrothermal synthesis of single crystalline ZnO

nanorods, the ease of crystallization and the favorable growth direction along the c-axis allow straightforward and low cost synthesis of ZnO nanostructured arrays.[108, 109]

2.2. Results and discussion

The basic setup of our photovoltaic cell (experimental details on page 32) is shown in Figure 2.1. The cell comprises an ITO base electrode (120 nm), followed by a thin ZnO film used as a hole blocking layer (generally 20 nm), a ZnO nanorod array filled with P3HT as the photoactive layer (0.1-1.1 µm), a solid P3HT film (50 nm - 450 nm) as an electron blocking layer, a PEDOT-PSS film (20 nm) intended to enhance the ohmic contact between the polymer and the Ag top electrode (80 nm).[103] To give the polymer sufficient time to soak into place during the sequential deposition of the individual layers (which is vital to create a maximal ZnO/P3HT interface) two main techniques are generally utilized. In case of solvent annealing, the polymer is spincoated from a high boiling point solvent and slowly dried.[87, 88] Alternatively, a lower boiling point solvent can be used, in which case the dried polymer is thermally annealed above its melting point.[86, 87, 110] In this work, in order to better understand the fundamental problems of such hybrid photovoltaic cells by evaluating as many aspects of device fabrication as possible, we followed the second approach by post-annealing as-prepared devices for different time scales (1 min, 15 min) at the melting temperature of P3HT (225 °C).

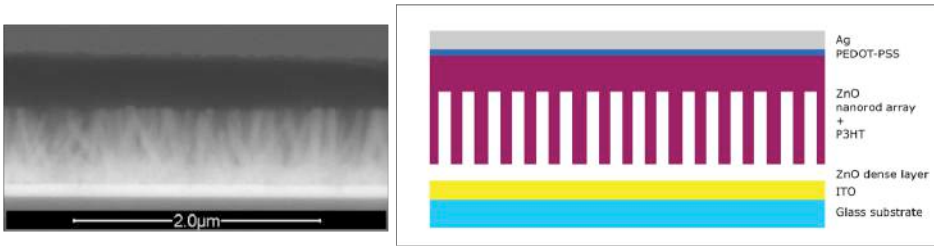

Figure 2.1. Back-scattered electron SEM image and schematic representation of the hybrid P3HT:ZnO solar cell.

To gain more insight into the formation of the photoactive part of the solar cell, the deep penetration of the polymer into the nanorod array is essential. The assessment of the polymer infiltration by means of electron microscopy techniques[87, 102, 104] is rather difficult as can be seen in the SEM image presented in Figure 2.1. Thus, depth

profiling based on Ar ion etching combined with X-ray photoelectron spectroscopy (XPS) is used here as an additional tool to study the element distribution within the photoactive layer for samples with different thermal history. Figure 2.2a shows the normalized core level intensities of contributing elements as a function of sample depth (expressed by the number of sputter cycles) for a pristine device. Starting from the top electrode, Ag is the most prominent element present with small additions of C arising from adsorbed hydrocarbons due to exposure to ambient conditions (region 1). Region 2 represents the dense polymer film acting as an electron blocking layer (EBL). Here, only C and S signals are detected in the XPS spectra. The thin PEDOT-PSS layer is undistinguishable from the pure P3HT due to its similarity in stoichiometry. When reaching the P3HT/ZnO composite layer (region 3), Zn and O (the latter not shown here) signals appear as additional contributions to the measured spectra. Region 4 reflects the dense ZnO (i.e., hole blocking) layer (HBL) onto which the rods were grown initially. Finally, in region 5, a strong In signal appears representing the ITO bottom electrode of the photovoltaic device.

From the depth depth profiling experiments, several important conclusions can be drawn: (i) The distributions of C and S atoms agree well with each other thereby evidencing a deep infiltration of the P3HT into the ZnO nanorod array already in the as-prepared state. Furthermore, significant contaminations of the ZnO rods and the ZnO base layer by additional carbon atoms can be excluded despite the presence of C-containing precursor materials during their synthesis; Otherwise, deviations in the distributions of S (representing the P3HT) and C (representing P3HT + additional contaminants) would be expected; (ii) During the depth profiling measurements, the O-1s core level was monitored as well (not shown here) confirming the 1:1 stoichiometry of the ZnO compound and the complete absence of oxygen based contaminations (like water) in the P3HT film within the detection limit of the spectroscopy (0.5 at%). (iii) In contrast to the sharp Ag/polymer interface observable in the depth profile, a significant overlap between the Zn and In signals is found in Figure 2.2a (regions 4 and 5). This, on one hand, could be due to the special setup of our device: in the 'valleys' between the nanorods the ions reach the ITO base electrode much earlier as compared to the areas covered by the ZnO rods.

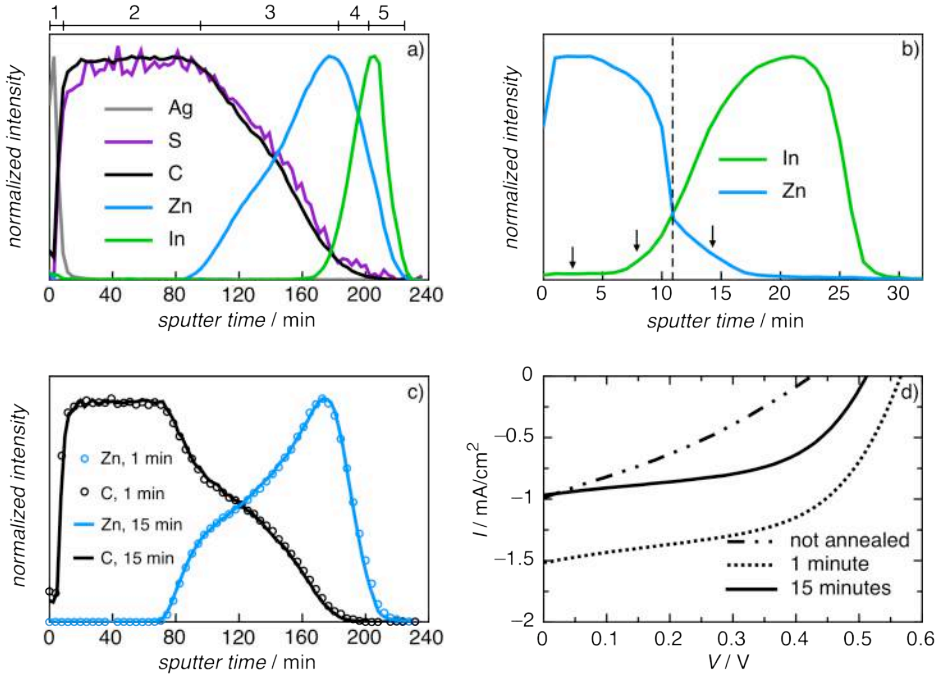

Figure 2.2. Normalized XPS intensities as a function of sputter cycles for (a) a pristine device, (b) a dense layer on ITO and (c) annealed devices (1 and 15 minutes). (d) corresponding I-V curves of (a) and (b).

On the other hand, thermally activated diffusion of Zn and In atoms crossing the ZnO/ITO interface during the preparation of the dense ZnO layer at 550 °C might contribute to the overlapping Zn and In signals as well. To study the relevance of such an effect in more detail, additional depth profiles were acquired on samples consisting only of a dense ZnO layer (100 nm) deposited on top of a ITO base layer (130 nm). The results are presented in Figure 2.2b, thereby clearly evidencing the interdiffusion of In atoms into the ZnO film with a minimum concentration of about 1 at% and of Zn atoms into the ITO electrode (see arrows). It is worth to mention that, as opposed to the dense layer, the ZnO nanorod array is prepared at a much lower temperature (95°C) thus allowing to safely exclude interdiffused species in this case.

Figure 2.2c depicts the Zn and C signal for devices that were annealed at 225 °C for 1 minute and 15 minutes. The resemblance between both sets of curves is striking, providing clear evidence that any additional annealing beyond 1 minute is redundant for infiltration, as the polymer has already reached the bottom of the nanorod array.

A direct comparison with the pristine device, that would yield more detailed information regarding the extent of infiltration in this case, is unfortunately not straightforward. This becomes obvious when comparing the carbon distributions presented in Figure 2.2a and Figure 2.2c. Clearly, in the latter case, a much shorter sputter time is required for the annealed samples to remove the pure polymer film (region 2). The increase in sputter efficiency for the polymer is also visible for the infiltrated part of the device where a much stronger decay of the C intensity (accompanied by a much stronger increase of the Zn intensity) can be recognized. The sputter yield of polymers under Ar ion bombardment is well known to be very sensitive to the degree of topological order.[111] In this case, (ion-induced) disorder in a polymer may result in a reduction of the sputter yield by more than one order of magnitude.[112] Turning this argument around, the observed increase in sputter efficiency after annealing a pristine device to the melting temperature of P3HT clearly points towards an improved structural order/crystallinity of the polymer within the electron blocking layer as well as the P3HT/ZnO hybrid layer, respectively. It is important to note, that no changes in thickness (density) of a reference P3HT film deposited on a Si/SiO_2 could be detected after such a heat treatment.

To gain more insight into the relation between infiltration/morphology and the electrical properties of the device, the depth profiling results need to be correlated to its photovoltaic performance (Figure 2.2d). The pristine device demonstrates the lowest short circuit current (I_{sc}) and open circuit voltage (V_{oc}), as compared to the annealed ones. On one hand, annealing induces a greater degree of crystallinity of the P3HT, which in any case contributes to an improved hole transport in the bulk polymer. On the other hand, it gives the polymer more time to arrange in between the nanorods, rendering the ZnO/P3HT interface more intimate, and thereby decreasing geminate recombination. Taking notice of the aforementioned similarity in infiltration for 1 minute and 15 minutes of annealing, it is reasonable to anticipate a roughly identical device performance. However, the 15-minute device shows considerably lower efficiency as compared to the 1-minute device, implying an additional effect that lowers both I_{sc} and V_{oc}. It might be speculated that, when the polymer is given more time in the molten state, its chains spontaneously align onto

the rods in the (1,0,-1,0)-direction (perpendicular to the rods),[110, 113, 114] thus inferiorly conducting in the desired z-direction and consequently allowing more non-geminate recombination. Degradation of the polymer upon longer annealing times is ruled out as a cause for lower performance, as UV-Vis spectra acquired on ZnO/P3HT samples annealed up to 2 hours were identical (See Supporting Information Figure 2.4 on page 34). XPS measurements on the ZnO/P3HT exclude chemical modification of the polymer during annealing of the polymer (which will be further described in a forthcoming paper).

In order to obtain well performing devices it is necessary to reduce leakage currents, which are the result of holes reaching the ITO electrode and electrons arriving at the top contact, respectively. Consequently, it is crucial to counteract these effects using a hole blocking layer (HBL) and an electron blocking layer (EBL). An optimal thickness of the blocking layers is necessary in favoring desired transport whilst impairing undesired transport: On the one hand thicker layers will induce smaller leakage currents and diminish unwanted transport, on the other hand they will obstruct desired transport due to inclusion of traps, impurities, larger pathways and an increased number of grain boundaries. In this work, the HBL is conveniently provided by the seed layer required for the synthesis of the ZnO nanorods. Upon increasing the seed layer thickness a modest decrease in device performance is obtained which is shown in Figure 2.3a. The cause of this effect is manifold. First of all, the total amount of defects in the seed layer scales with the number of individual sublayers. Secondly, a thicker seed layer has larger grains, which is inherently related to a larger diameter of the grown nanorods. This implies that even though a thicker HBL might still be beneficial by itself, the effect might be compensated by a smaller photocurrent as a consequence of a smaller donor-acceptor interface. Furthermore, due the direct proportionality between the amount of grain boundaries and the number of deposition cycles an excessively thick seed layer will inevitably have a negative effect on the HBL resistance. Therefore the optimal thickness of 20 nm is used in all of the devices. This is in accordance with the weak coupling in the valence band state between P3HT molecules and ZnO, by which hole injection into the ZnO is rather unlikely.[113] Moreover, compared to electrons, the diffusion length of holes is rather

small in ZnO nanorods whereby holes getting through to the ITO contact is improbable.[115][24]

Just as much as an HBL is required for blocking holes, an EBL is needed to reduce the leakage current from electrons towards the metal electrode. Here, the EBL is formed by the remaining polymer layer on top of the nanorod array. Where in the case of the HBL a thin layer is needed, a thick EBL of 250 nm is required to prevent electron transfer from ZnO towards P3HT and recombination (Figure 2.3b). This can be clarified by the fact that the electron mobility in P3HT is almost equivalent to the hole mobility,[116] which works in favor of the leakage current and thus results in the need for a thicker EBL.

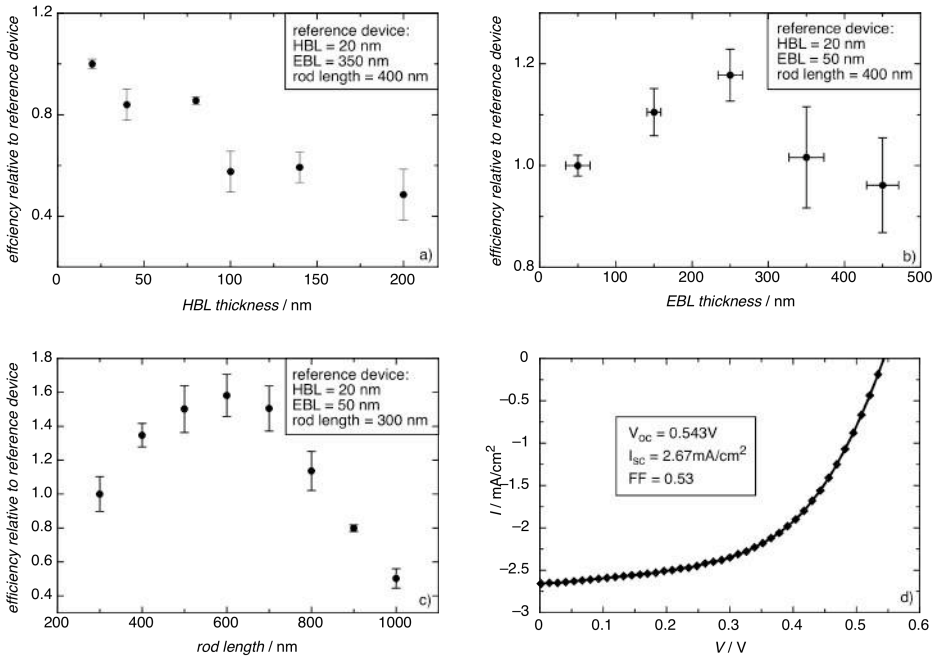

Figure 2.3. Device performance relative to reference devices as function of (a) HBL thickness, (b) EBL thickness and (c) length of ZnO nanorods. (d) I-V curve of the optimal device.

As mentioned before, a large interface area is indispensable for an efficient solar cell. Therefore, longer nanorods would in principle result in a higher photocurrent, though this is not a linear relation as an excessive rod length will induce longer hole transit times (which the polymer cannot support) and therefore promote recombination.

Devices with different nanorod lengths (from 300 nm up to 1µm) were synthesized. To evaluate only the effect of the nanorod length, the EBL on top of the arrays was kept constant. As Figure 2.3c illustrates, the predicted dependence of photocurrent on rod length is confirmed, putting forward 600 nm as the optimum.

Having found the device properties that form the best compromise between charge transport and light harvesting, solar cells were prepared accordingly. Herein, an I_{sc} of 2.67 mA/cm², a V_{oc} of 0.543 V and a *FF* of 0.53 was obtained, giving an efficiency of 0.76%. This represents an increase by 40 % as compared to values reported in the literature for this device configuration (0.55 %).[86] (See Figure 2.3d and Supporting Information Figure 2.5, Figure 2.6 on pages 35-36**).**

2.3. Conclusion

In conclusion, nanostructured ZnO/polymer hybrid photovoltaic cells have been analyzed combining XPS depth profiling and electrical characterization. Already in the as-prepared state, a deep infiltration of the polymer into the nanorod array is observed. However, the efficiency of such a device can be improved by post-annealing at the melting temperature of the polymer for a well-defined time (1 minute) resulting in an improved crystallinity of the polymer. Subsequent annealing diminishes the device performance most likely due to unfavorable ordering of the polymer chains with respect to the nanorods. A significantly improved efficiency of 0.76 % for such type of hybrid solar cell can be achieved by optimizing the ZnO/polymer interfacial area in combination with a control of leakage currents by means of appropriate blocking layers for electrons and holes. This approach might open the door to considerable further improvements in efficiency in the future by fine-tuning the properties of the nanorod array (degree of order, diameter of/distance between nanorods etc) thereby allowing to challenge the current device concepts.

2.4. Experimental details

ZnO nanorods. ZnO nanorods were synthesized using a two step process consisting of seeding and hydrothermal growth. A seed layer was deposited by an aqueous solution-gel method.[117] Prior to seed layer deposition, patterned ITO (15 Ω/sq, Every Rich Enterprise Limited) on glass was successively cleaned by sonication in a soap solution, deionized water, acetone and in boiling isopropanol each for 10 min. In order to improve the wettability of the substrate for the aqueous precursor solution, the wet cleaning was followed by a 15 minutes UV-ozone treatment before spin coating. Next, the substrates were heated on a hotplate at 300 °C for 1 minute followed by a hotplate step at 500 °C for 5 minutes to obtain a thin film. Depending on the thickness of the desired HBL, this process was repeated several times in order to create a dense ZnO layer. The substrates were finally annealed in a horizontal tube furnace for 1 h at 550 °C in an oxidizing atmosphere of dry air.

For the hydrothermal growth of the nanorods, an aqueous solution was prepared by dissolving equimolar (0.025 M) zinc acetate dihydrate (Aldrich) and hexamethylenetetramine (Aldrich) in deionized water. This mixture, together with the seed layer covered substrates was placed in a closed Pyrex bottle. The hydrothermal reaction was done in a furnace at 95 °C for diverse times depending on the desired nanorod length. Afterwards the solution was cooled down naturally for 1 h, before the samples were removed. The samples were then rinsed with deionized water and dried at 60 °C for 1 h.

Photovoltaic devices. The freshly prepared ZnO coated ITO substrates were heated at 150 °C for 20 minutes and cooled down with N_2 flow[87] prior to spincoating low molecular weight P3HT (Rieke Metals) solutions in chlorobenzene (Aldrich). After deposition, the samples were annealed at 225 °C in N_2 for different times to enhance infiltration into the nanorods and to enhance the crystallinity of the P3HT. A thin PEDOT layer was spin coated onto the polymer and annealed for 5 min at 120 °C. Finally, 80 nm Ag top electrodes were evaporated in vacuum ($1 \cdot 10^{-6}$ mbar) on top. In total more than 300 devices were fabricated. To guarantee reproducibility and small standard deviation, extra optimal devices were prepared in different batches. Device measurements were performed in air at room temperature, under an AM1.5

illumination of 100 mW/cm² with a Newport Oriel Class A model 91195A solar simulator. To examine the device morphology, scanning electron micrograph (SEM) images were obtained with a FEI Quanta 200FEG-SEM equipped with secondary electron (SE) and back scattered electron (BSE) detectors. Layer thicknesses were determined by means of cross sectional SEM (X-SEM). X-ray photoelectron spectroscopy (XPS) was carried out on a commercial electron spectrometer (PHI-5600LS) to verify the infiltration of the P3HT into the nanorods and to study changes induced by annealing. In a sequence of alternate probing and etching steps (2 min, 5 keV, 2 µA sample current) in the z-direction, the composition of the devices was investigated. After each etching step, an XPS spectrum was taken to identify the element distribution.

Optimization process. The thickness of the hole blocking layer was tuned by deposition of a different number of spincoated dense layers forming the seed layers. The length of the ZnO nanorods from 100 nm up to 1 µm is tuned by varying the reaction time during the hydrothermal synthesis. A linear growth pattern is obtained by increasing the reaction time. The thickness of the electron blocking layer and the cast polymer is tuned by varying the concentration and spincoat speed.

2.5. Supporting information

2.5.1. UV-VIS spectra

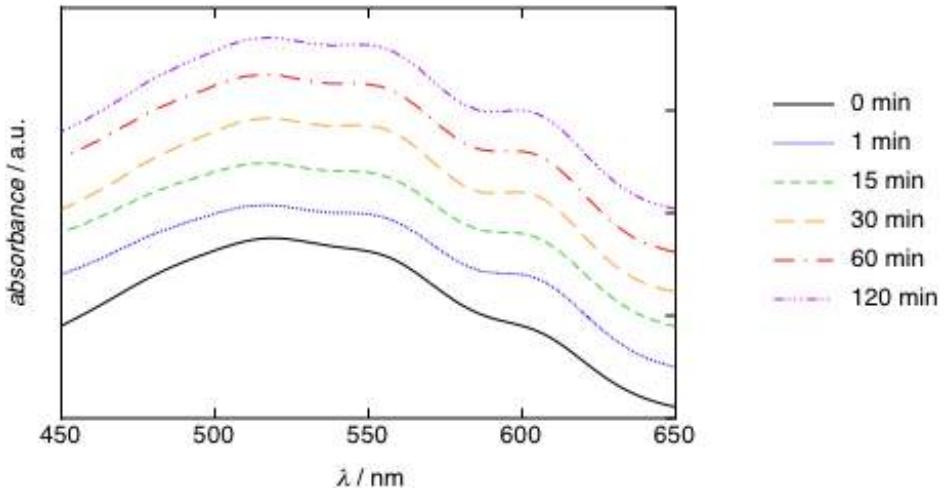

Figure 2.4. UV-Vis spectra of ZnO nanorods/P3HT, for different times at 225 °C. The shoulder at 600 nm that indicates crystallinity is much less prominent in the unannealed case [118, 119]. The other curves are identical, which means that the crystallinity is independent of the annealing time, and no degradation of the polymer occurs, even up to 2 hours.

2.5.2. Optimization parameters

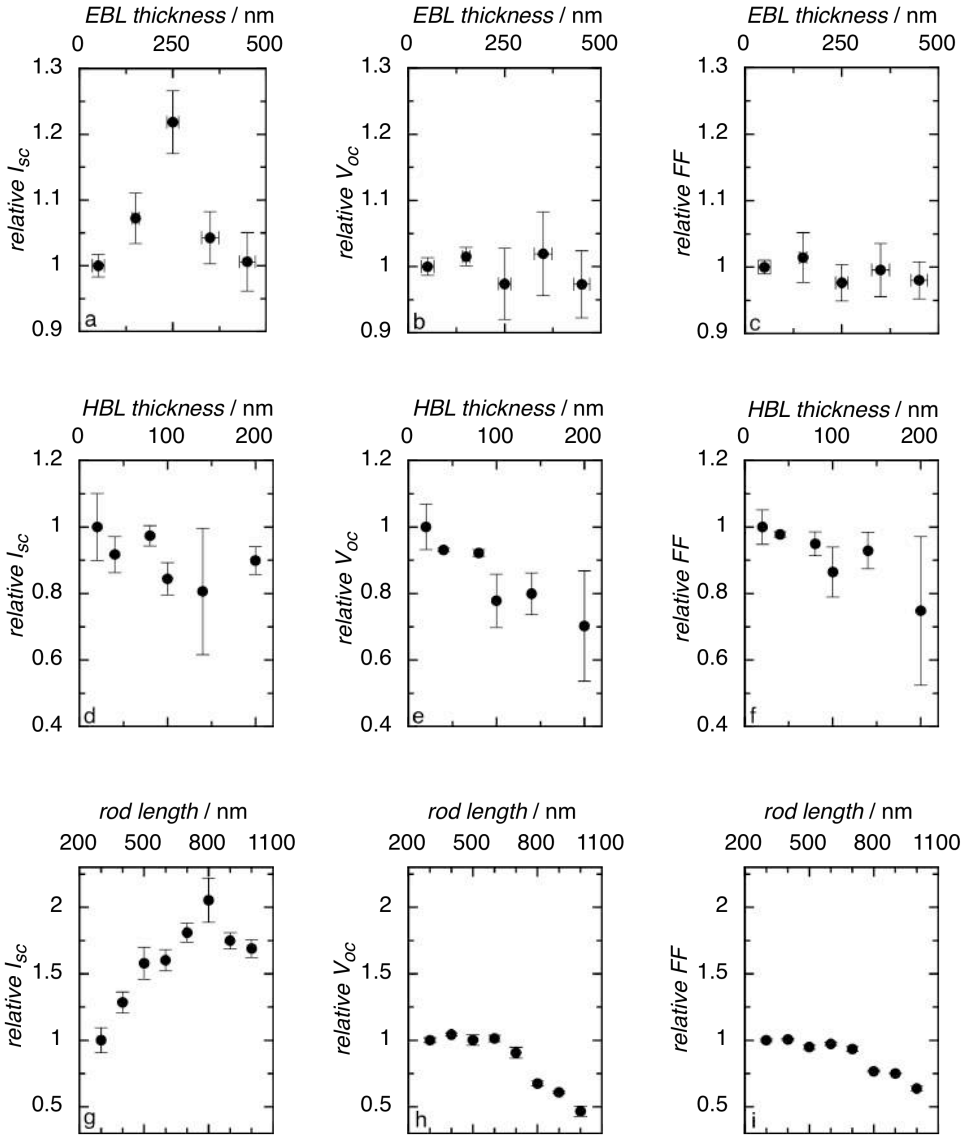

Figure 2.5. I_{sc}, V_{oc} and *FF* as a function of EBL thickness (reference device: 20 nm HBL, 400 nm ZnO rods and the thinnest EBL (50 nm)): (a), (b) and (c), HBL thickness (reference device: 20 nm HBL, 400 nm ZnO rods and 350 nm EBL): (d), (e) and (f) and length of ZnO nanorods (reference device: 20 nm HBL, 300 nm ZnO rods and 50 nm EBL): (g), (h) and (i). All the graphs show normalized values to emphasize the impact of each optimization step individually. Figures (a), (b) and (c) show that the I_{sc} is responsible for the optimum in the EBL layer. The V_{oc} and *FF* are comparable for all

EBL thicknesses. Figures (d), (e) and (f) show that for a thicker HBL, the decrease in efficiency is mainly caused by V_{oc} and *FF*. The optimum in rod length is the result of a competitive process between an increase in I_{sc} (g) and a decrease in V_{oc} and *FF* with increasing rod length ((h) and (i)).

2.5.3. IV-curve optimal device

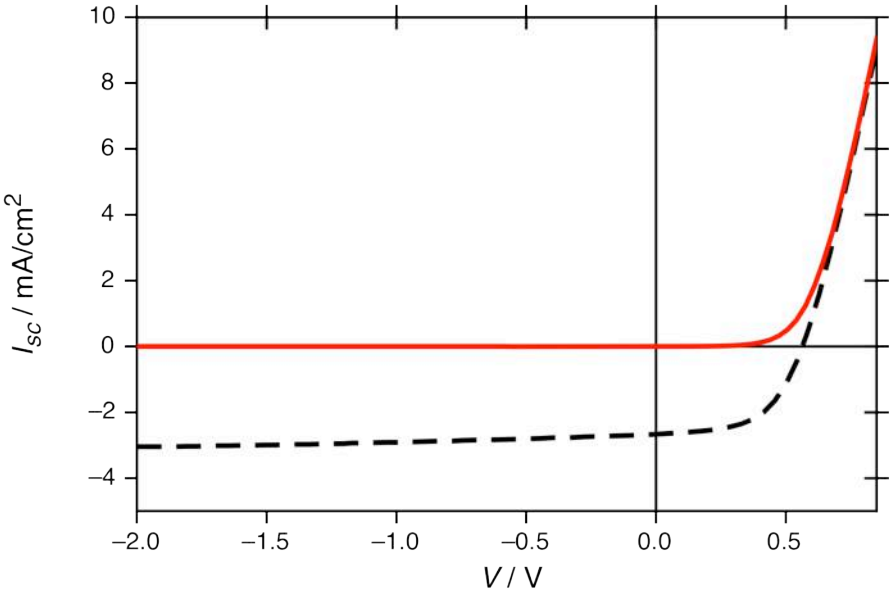

Figure 2.6. IV-curve dark (red) and illuminated (dashed black) of device with optimal parameters (20 nm dense ZnO layer as hole blocking layer, 600 nm ZnO rods, 250 nm P3HT as electron blocking layer).

Chapter 3

Tuning the dimensions of ZnO nanorod arrays for application in hybrid photovoltaics

*L. Baeten, *B. Conings, J. D'Haen, C. D. Dobbelaere, A. Hardy, J. V. Manca, M. K. Van Bael, *ChemPhysChem,* **2012,** DOI: 10.1002/cphc.201200102.

ABSTRACT

ZnO nanorod arrays are a very eligible option as electron acceptor material in hybrid solar cells, owing to their favorable electrical properties and abundance of the available easy and low-cost synthesis methods. In order to become truly effective in this field, a major prerequisite is the ability to tune the nanorod dimensions towards optimal compatibility with electron donating absorber materials. In this work, a water- based seeding and growth procedure is used to synthesize ZnO nanorods. The nanorod diameter is tuned either by modifying the zinc concentration of the seeding solution or by changing the concentration of the hydrothermal growth solution. Consequences of this morphological tailoring in the performance of hybrid solar cells are investigated, leading to a new record efficiency of 0.82 % for hydrothermally grown ZnO nanorods of 300 nm in combination with poly(3-hexylthiophene-2,5-diyl) (P3HT). This improvement is attributed to a combined effect of nanorod diameter and orientation, and possibly to a better alignment of the P3HT backbone, resulting in an improved charge transport.

Despite that the part of this paper comprising the synthesis of the nanorod arrays was carried out in the PhD work of Linny Baeten, it is included in its entirety for the sake of clarity.

3.1. Introduction

As a result of quickly increasing global energy consumption and concerns regarding CO_2 emission, photovoltaics are drawing ever more interest as an alternative and clean energy source.[120] One of the representatives of third generation photovoltaics is the hybrid solar cell, which utilizes a combination of inorganic and organic semiconductors to form the active layer. Generally, an n-type inorganic semiconductor acts as an electron acceptor and the p-type organic polymer serves as light absorber and electron donor.[101] These hybrid solar cells have some compelling benefits compared to fully organic based ones, such as higher electron mobility of the inorganic layer, higher chemical and morphological stability, and the possibility of easy and low cost synthesis of the inorganic layer.[121, 122]

ZnO attracts a lot of interest for the integration into hybrid solar cells, because of its reduced toxicity and higher electron mobility compared to other inorganic semiconductors.[83, 123] However, solar cells based on ZnO nanoparticles can only obtain limited efficiencies because of the trap-limiting electron diffusion process in the nanoparticle network at the grain boundaries.[106] A logical strategy to tackle this problem is to replace the porous nanoparticle network by an array of aligned ZnO nanorods.[85] The one-dimensional structure of the nanorods is capable of providing "highways" for electrons to the electrode with less trapping sites, whilst providing a large interface with the light absorber.[107] Highly ordered structures can be fabricated through various methods such as physical vapor deposition (PVD)[124, 125], chemical vapor deposition (CVD)[126], template-assisted deposition[127], electro-deposition[128], electro-spinning[104] and hydrothermal growth[108, 109, 126, 128, 129] with or without the use of a seed layer.

In order to obtain appreciable efficiencies in nanostructured hybrid solar cells, a substantial donor-acceptor interface area –provided here by the nanorod array– is crucial. Moreover, the spacing of the nanorods in nanostructured arrays needs to be

in the order of twice the exciton diffusion length (typically 10 nm), which means that the nanorods should be fairly closely packed (maximum 20 nm apart).[129, 130] Additionally, to prevent charge transport issues, the nanorods should not be too thin.[131] These requirements taken into account, it is clear that finding the perfect balance between interfacial area and charge transport by controlling the dimensions of the ZnO nanorods is one of the major goals for the development of ZnO/polymer solar cells with higher performances.

Recently, we demonstrated an efficiency of 0.76% (a 40% improvement compared to previous work) for hydrothermally grown ZnO nanorods combined with poly(3-hexylthiophene-2,5-diyl) (P3HT) by optimizing thickness of the hole and electron blocking layers, length of the ZnO nanorods and by tuning the crystalline quality of the infiltrated P3HT.[132] Yet, a further improvement of the efficiency should be achievable by controlling the diameter and packing of the nanorods. In this work, we report on the control of the ZnO nanorod dimensions and packing by a two-step seeding/growth method. The average diameter of the nanorods is tuned either in the seeding step or in the growth step. Furthermore, consequences in the performance of hybrid solar cells as a result of tailoring the nanorod diameter are investigated.

3.2. Results and discussion

3.2.1. Influence of the seed layer

The crystalline ZnO film has a twofold purpose. On the one hand, on non-lattice-matching substrates like glass, SiO_2 or ITO-coated glass substrates, it acts as a seed layer for the nucleation and growth of ZnO nanorod arrays during hydrothermal synthesis.[129] On the other hand, the second function of the dense layer lies in its hole blocking nature in the solar cell by reducing leakage currents resulting from holes reaching the ITO electrode.

A starting point to control the nanorod diameter is through variation of the seed layer's morphology, thereby changing the size of the grains it consists of. The first possible strategy to accomplish this consists of the deposition of multiple layers on top of one another. The XRD pattern (Figure 3.1d) obtained from 0.5 M Zn(II)-precursor indicates the polycrystalline character of a 20 nm thick, dense ZnO layer

after thermal treatment, obtained from a single deposition. AFM analysis (Figure 3.1b) points out that the resulted film forms a dense layer consisting of grains with a diameter around 40 nm.

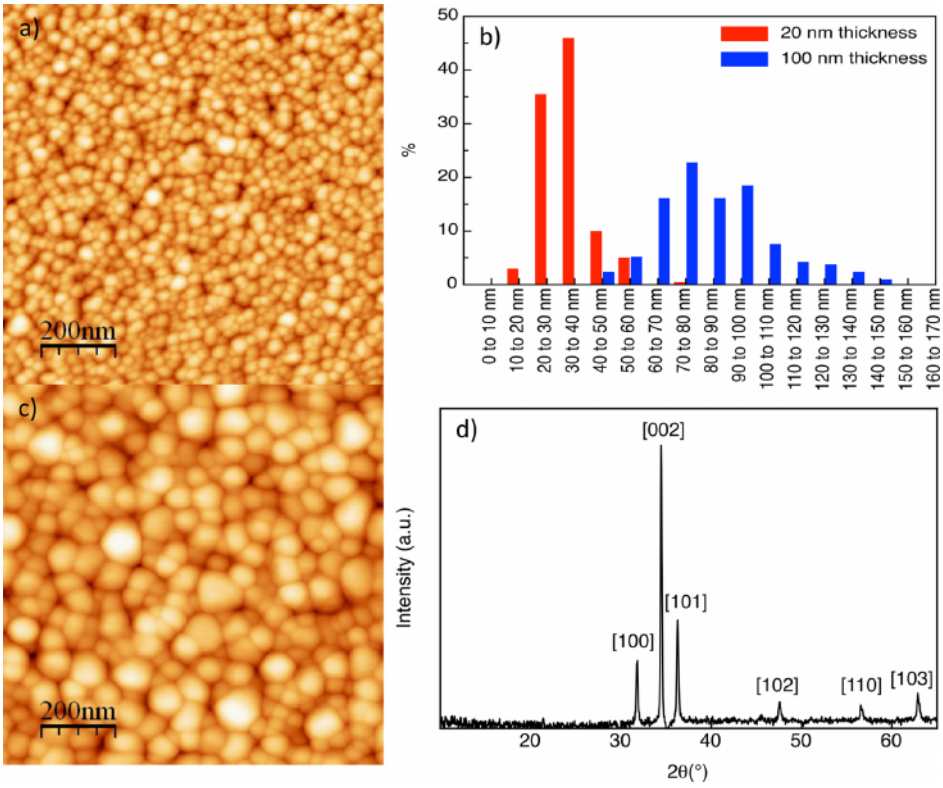

Figure 3.1. a) AFM image of a 20 nm thick ZnO dense film formed after thermal treatment of a 0.5 M Zn(II)-precursor. b) Diameter distribution of the ZnO grains of a 20 nm film (red) and a 100 nm film (blue). c) AFM image of a 100 nm thick ZnO dense film formed after a thermal treatment of a 0.5 M Zn(II)-precursor. d) XRD pattern of a 20 nm dense film after a single deposition.

Depositing a compound seed layer in several subsequent identical steps proves to be of significant influence on the grain size in the resulting dense film. The XRD pattern of thicker layers is similar to those of 20 nm ZnO layers (Figure 3.1d). The AFM analysis and SEM analysis of these seed layers show a direct proportionality between the grain size and the number of deposition cycles (Figure 3.1b). Increasing the thickness of the seed layer from 20 nm to 100 nm also increases the diameter of the ZnO seeds from an average of 40 nm up to a broad distribution between 40 nm and 170 nm (with an

average of 80 nm). The effect of increasing grain size by multiple depositions can be attributed to longer exposure to elevated temperatures, as each deposition cycle requires its own thermal treatment.

To isolate only the influence of the dense layer, all other parameters were kept constant during the hydrothermal growth of the nanorods. The corresponding XRD pattern of the nanorods grown from the seed layers from Figure 3.1a and c are identical and shown in Figure 3.2a. It contains mainly the [002] peak, confirming the preferential growth direction of ZnO along the c-axis[133], indicating that seeds with c-axis orientation normal to the substrate will act as nucleation sites for the grown nanorods. There is a clear correlation between the seed layer's grain diameter and the resulting nanorod diameter. SEM analysis shows an average diameter around 60 nm and 100 nm for the ZnO nanorods grown on a seed layer of 20 nm and 100 nm thickness, respectively (Figure 3.2b-e). It can be seen that the nanorods are well separated, indicating that they grow individually rather than by branching. Nevertheless, the average diameter of the nanorods is larger than the grains in the seed layer, indicating that different grains in the seed layer nucleate to allow for the growth of one nanorods, also observed by Lee et al.[134] Recently, we showed that a 20 nm thick seed layer is the optimal for hole blocking layer in hybrid solar cell.[132] Former results taken into account, it is now apparent that this optimum is not only related to the suppression of leakage current alone, but also to its slightly different morphology, leading to morphology changes in the nanorods array. That is, a higher number of deposition cycles to form the seed layer, thus a larger thickness and grain size, induces thicker nanorods. As a result of the larger diameters, the distance between the nanorods decreases, as can be visually evaluated from Figure 3.2b and d. The optimum at 20 nm may indicate that a certain level of nanorod spacing is needed, even if it exceeds twice the exciton diffusion length. This can be explained by a possible reluctance of polymer chains to infiltrate into insufficiently spaced nanorods, or related issues (*vide infra*).

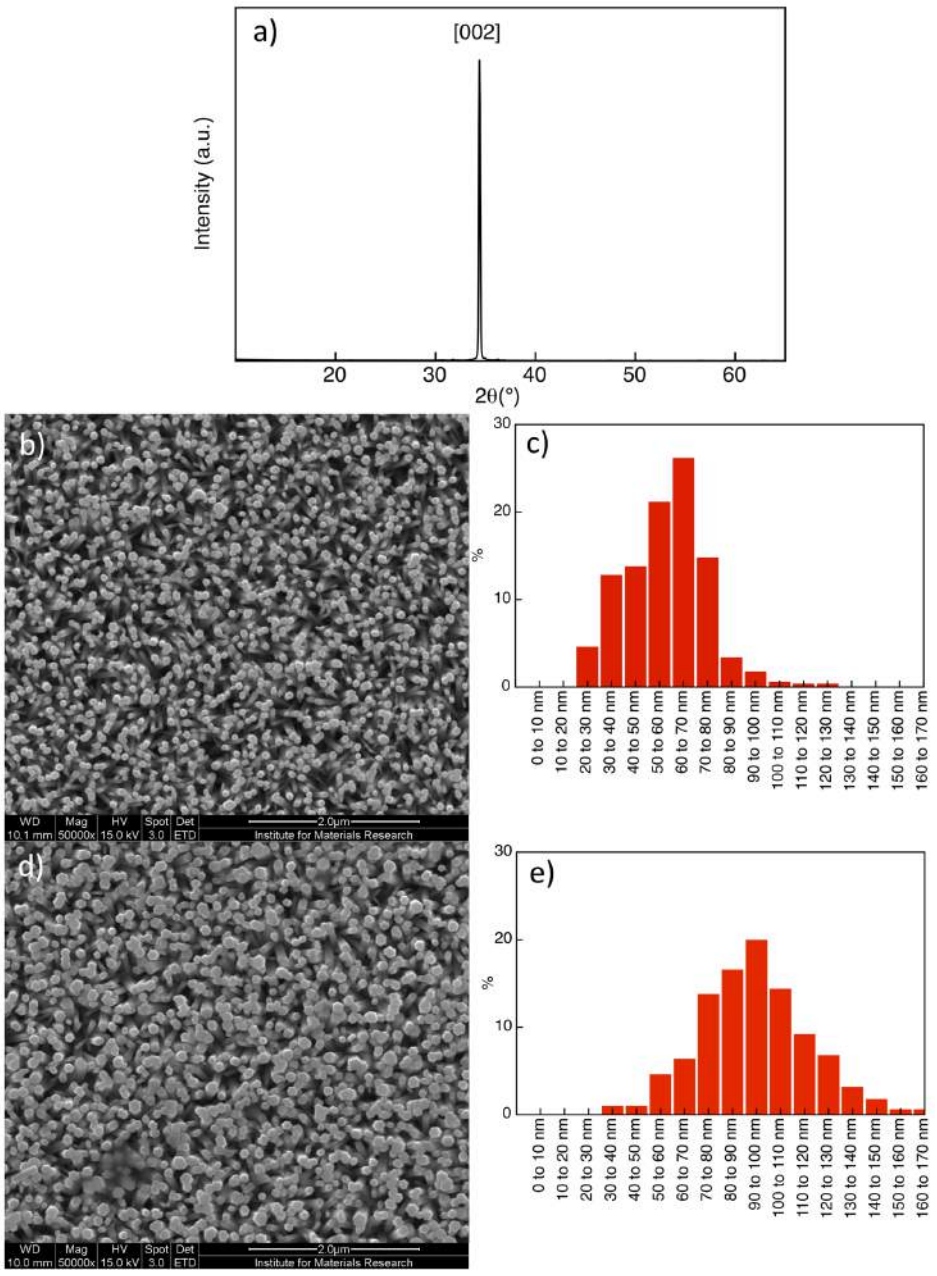

Figure 3.2. XRD pattern of hydrothermally grown nanorods in an equimolar solution of 0.025 M $ZnAc_2$ and HMT. b) Top-view SEM image and c) corresponding diameter distribution of ZnO nanorods on a 20 nm dense layer. d) Top view SEM image and e) corresponding diameter distribution of ZnO nanorods on a 100 nm dense layer.

A second strategy to change the seed layer morphology is the Zn(II)-precursor concentration.[135] Figure 3.3 shows that decreasing the precursor concentration also decreases the grain size. The 0.125 M precursor provides the smallest grain diameter of 25-30 nm in the ZnO seed layer after thermal treatment. A further reduction of the Zn(II)-precursor concentration gave rise to island formation of ZnO grains. This is unacceptable for application in solar cells, as the voids in between the resulting nanorods would completely eliminate the blocking character of the dense ZnO seed layer and, consequently, leakage current would prevail over photocurrent.

Figure 3.4 shows SEM images of the resulting nanorod arrays after hydrothermal growth on the substrates from Figure 3.3. By comparing Figure 3.3 and Figure 3.4, one can roughly state that smaller grains will end up in smaller nanorod diameters, although the shift of the size distributions along precursor concentration is not identical for nanorods versus grains. Additionally, vertical alignment of the nanorods and packing density improve by reducing the grain size. For all cases, the diameter of the nanorods is slightly bigger than the diameter of the grains of the corresponding seed layer, indicating that nanorods on average grow on more than one grain in the seed layer.

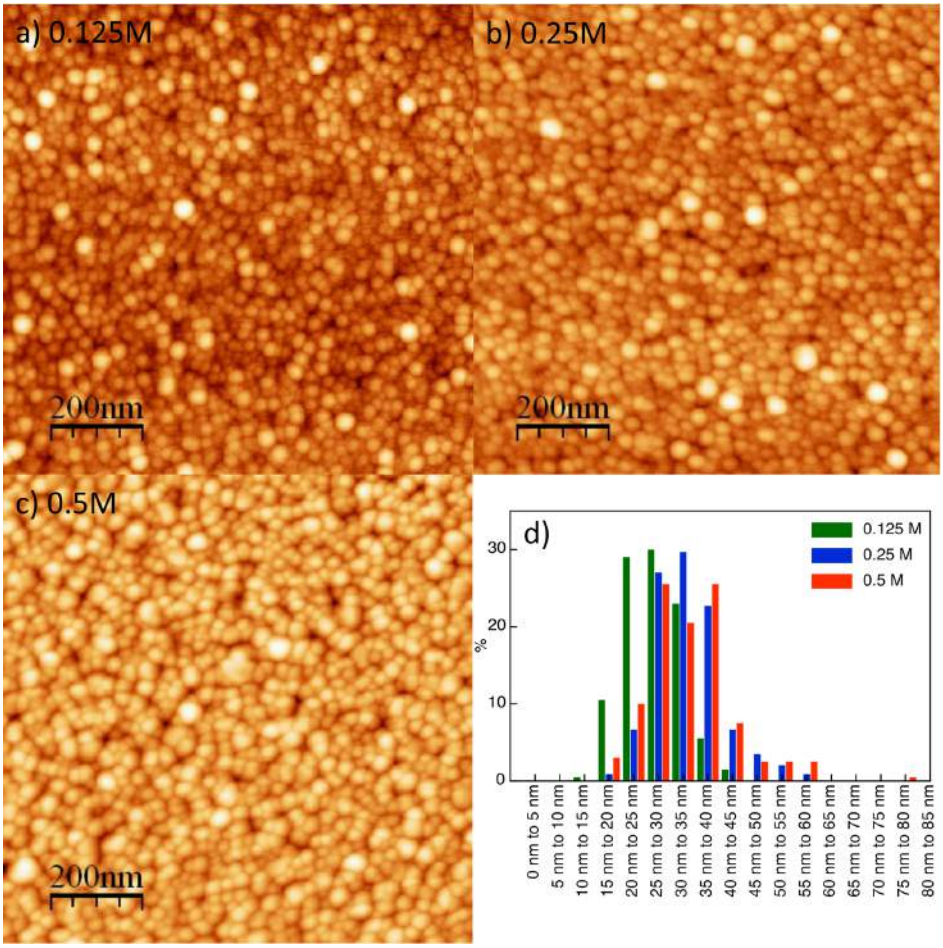

Figure 3.3. AFM image of ZnO dense film starting from a a) 0.125M Zn(II)-precursor, b) 0.25 M Zn(II)-precursor and c) 0.5 M Zn(II)-precursor. d) Diameter distribution of corresponding AFM images.

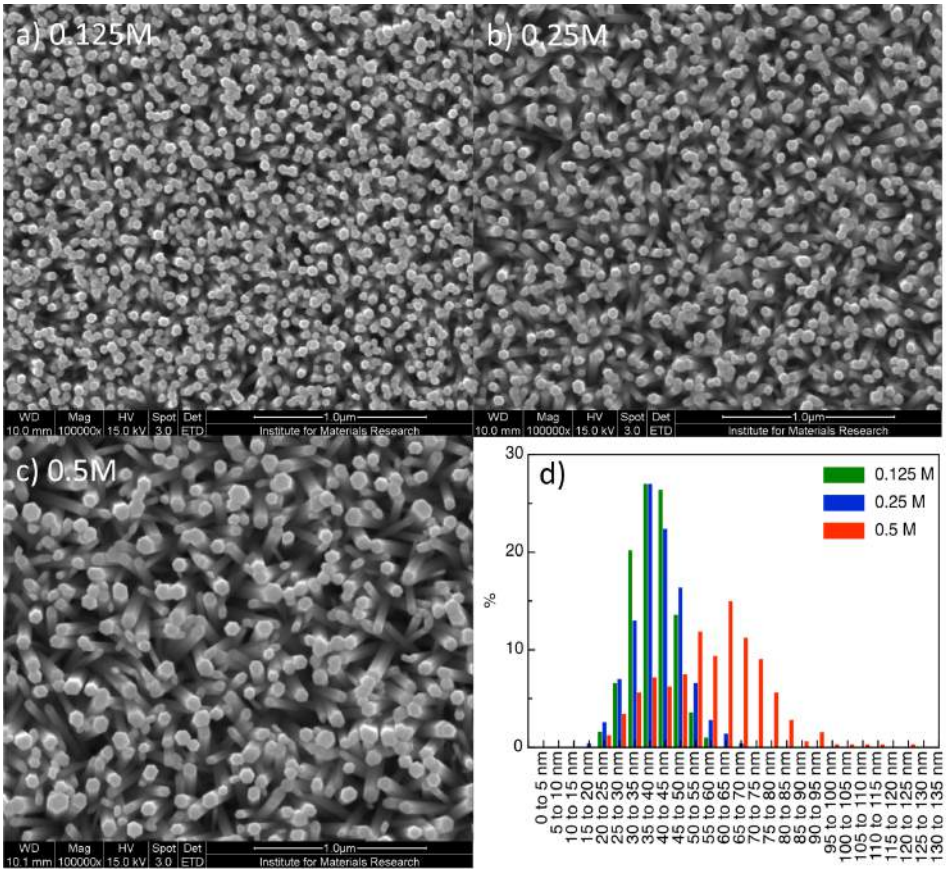

Figure 3.4. SEM images of hydrothermally grown ZnO nanorods in an equimolar solution of 0.025 M $ZnAc_2$ and HMT on a dense film starting from a) 0.125 M Zn(II)-precursor b) 0.25 M Zn(II)-precursor c) 0.5 M Zn(II)-precursor. d) Diameter distribution of the grown ZnO nanorods presented in the SEM images.

3.2.2. Influence of the hydrothermal growth conditions

While the first approach to control the nanorod dimensions was fully based on tuning the seed layer properties, a different approach relies on changing the concentration of the hydrothermal growth solution. In changing this concentration, the resulting nanorod diameter does not increase with longer growth times and the distributions are similar for all lengths of nanorods (not shown). For all samples in this section the 0.5 M based ZnO layer seed as shown in Figure 3.3c is used from which a 300 nm nanorod arrays are grown. SEM images and corresponding histograms of the

nanorods grown with varying hydrothermal growth concentration ranging from 0.0125 M up to 0.1 M are depicted in Figure 3.5. It appears that the lowest concentration (0.0125 M) yields narrow and more slant nanorods, while raising the concentration (0.25 M and 0.5 M) produces increasingly thicker and well-aligned nanorods, up until the highest concentration (0.1 M) in which case the nanorods become so thick they form a continuous layer. This outcome implies that higher concentrations of $ZnAc_2$ and HMT will lead to faster formation of $Zn(OH)_2$, generating an accelerated nucleation and nanorod growth. Furthermore, the more aligned nature of nanorods grown at higher concentrations can be explained by considering the combined effect that (i) as mentioned in the previous section, thicker nanorods must originate from more than one grain, and (ii) the unification of several grains on average rectifies their individual off-normal orientation and thus their tendency to grow a tilted nanorod.

Latter results show clear evidence that diameter and packing density hinge on the variation of precursor concentration (thus seed layer morphology) and hydrothermal growth concentration. Building on this premise, one would expect narrow, highly packed and aligned nanorods through combination of concentration of 0.125 M of the Zn(II)-precursor for the dense layer and 0.0125 M for hydrothermal growth. Nevertheless, the corresponding SEM image (Figure 3.6) shows that for these conditions narrow nanorods with a diameter between 10 nm and 45 nm are formed but the density is low, indicating that other, unknown parameters can have an additional influence on the density and diameter of the nanorods array and require further research.

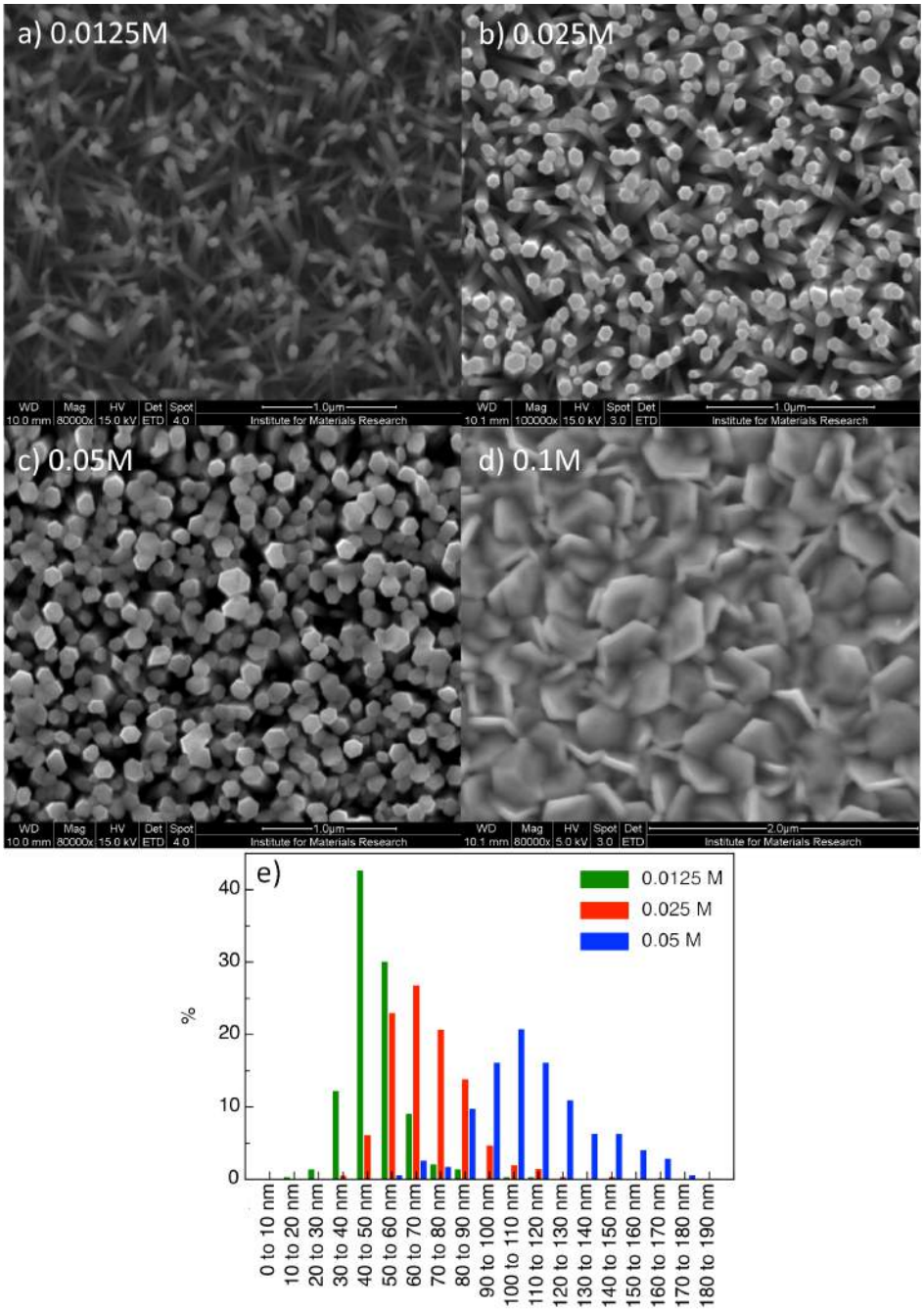

Figure 3.5. SEM images of hydrothermally grown ZnO nanorods on a dense ZnO film starting from a 0.5 M Zn(II)-precursor in an equimolar solution of a) 0.0125M $ZnAc_2$ and HMT, b) 0.05 M, c) 0.025 M, d) 0.1 M, forming a continuous layer. e) Diameter distribution of the grown ZnO nanorods.

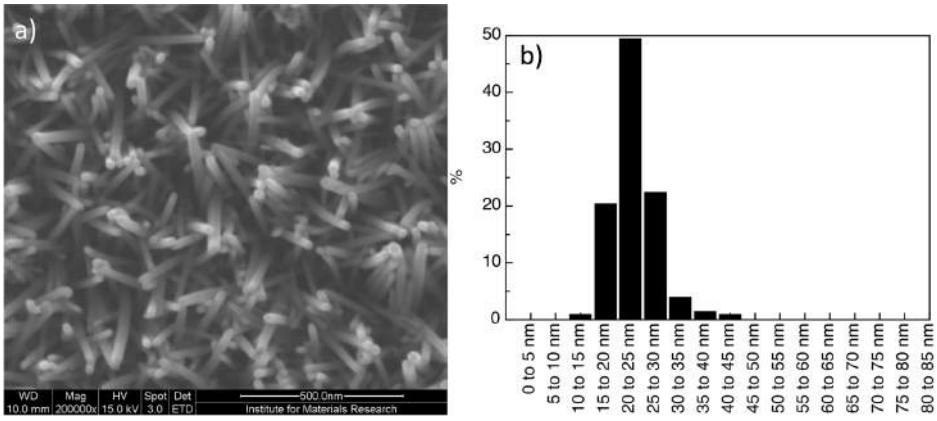

Figure 3.6. a) SEM image of the nanorod array based on a seed layer from a 0.125 M precursor and a hydrothermal growth concentration of 0.0125 M. b) Corresponding distribution of nanorod diameter.

3.2.3. Solar cell characteristics

To gain insight in the consequences of nanorod morphology on photovoltaic performance of the resulting ZnO nanorod/P3HT solar cells, the photovoltaic parameters of devices with variable nanorod diameter and density are compared. Table 3.1 summarizes the photovoltaic parameters of 5 devices, together with a reference to their corresponding SEM images. The IV-curves can be found in Figure 3.7. Devices A, B and C differ in the concentration of hydrothermal growth of their nanorods (0.05 M, 0.025 M and 0.0125 M, respectively). Comparing device A and device B, it is immediately clear that the enhanced efficiency of B stems from a higher short circuit current I_{sc}, which is unmistakably the result of a difference in interface area, owing to their different average nanorod diameter (see Figure 3.5b (device B) and Figure 3.5c (device A)). Taking device C in the comparison, the story changes. While the nanorod diameter of this device is significantly lower than the other two, also the nanorod density is significantly lower (see Figure 3.5a). Although this combined effect results in an inferior interface area for device C compared to device A and B, with 0.82% it reaches the highest efficiency of this work, owing to a remarkably I_{sc}. Even more startling is the fact that this efficiency exceeds the 0.76% we could formerly only achieve with nanorods of 600 nm, which had higher density, diameter

Table 3.1 : IV-characteristics for devices with different morphology.

Device [a], [b]	I_{sc} (mA/cm^2)	V_{oc} (V)	*FF*	η (%)	SEM	<diam.> (nm)
A DL: 0.5 M HT: 0.05 M	0.43	0.608	0.54	0.14	Fig. 5c	110
B DL: 0.5 M HT: 0.025 M	1.57	0.603	0.59	0.56	Fig. 5b	70
C DL: 0.5 M HT: 0.0125 M	2.64	0.565	0.55	0.82	Fig. 5a	50
D DL: 0.125 M HT: 0.025 M	1.05	0.608	0.60	0.38	Fig. 4a	40
E DL: 0.125 M HT: 0.0125 M	0.95	0.549	0.57	0.30	Fig. 6a	25

[a] DL is the concentration of the precursor in the dense layer process [b] HT is the concentration $ZnAc_2$ and HMT during hydrothermal growth)

and length compared to the nanorod array from device C).[132] Three possible explanations can be given: i) due to the tilted nanorods, more scattering of the incident light can occur. ii) Conings et al. reported a difference in orientation of the P3HT chains on the side planes of the nanorods, which has a negative effect on the transport.[136] By tilting the nanorods as in device C, the orientation of the P3HT chains with respect to the desired charge transport direction changes, leading to a possibly better alignment of the P3HT. iii) related to point (ii), the lower nanorod density itself may also induce a better alignment of polymer chains by virtue of the extra space in the more open nanorod array, causing a higher fraction of the polymer behaving as bulk rather than interfacial (hence a higher portion of the polymer is in the crystalline

state). This hypothesis could be supported by the observation that device D exhibits a lower I_{sc} than device A, B, and C: its nanorod density is high (and well-aligned), loosely compensating for a possible loss of interfacial area due to a lower average nanorod diameter, but at the same time leaving little room for polymer chains to align conveniently in between nanorods and thus inducing inferior transport. On the other hand, this argument is predicated on a fully infiltrated array, which might not be the case. Finally, device E, performs rather disappointingly. Building on the fact that this device, which contains nanorods of 25 nm average diameter, is the sibling of device C (also randomly oriented, low density, but 50 nm average nanorod diameter), and resting on the excellent performance of the latter one, a very likely explanation for device E's inferior performance is the inability of its narrow nanorods to transport electrons effectively to the electrode.[131] Additionally, the nanorods of device E (see Figure 3.6a) seem more clustered which will decrease the interface area even more, which is also a detrimental factor for device performance.

Based on these new insights, and the result from former optimization,[132] the nanorods length of device C was increased to 600 nm to attempt a further efficiency enhancement. Unfortunately, this new device showed a decrease in device performance (not shown), which could be attributed to the inability of the narrow nanorods to transport charges over such long distances. Rigorous theoretical foundations that link electro-optical and morphological characteristics can open the door to a better understanding and therefore systematic optimization of these devices.

The performance comparison of this set of devices, prepared based on the acquired knowledge regarding tuning of the nanorod dimensions, points to an optimum in nanorod thickness and orientation. Somewhat counter intuitively, randomly tilted nanorods with an average thickness of 50 nm appear to be the optimal configuration that can be produced with the techniques described in this work. A possibility to enhance the photocurrent even more would be to create narrow and much shorter nanorods with higher density. Narrow width and high density ensure a high interfacial area, and by virtue of the short length, transport issues related to nanorod thickness

and polymer orientation would be minimized, while polymer infiltration would stay fairly easy.

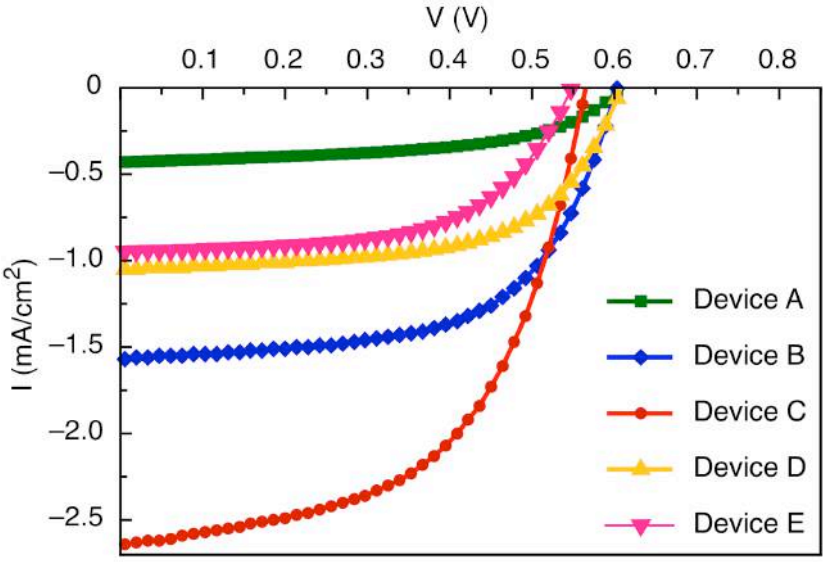

Figure 3.7. IV-curves of photovoltaic devices presented in Table 3.1.

3.3. Conclusion

In this work, we report on the manipulation of ZnO nanorod array dimensions and packing by a two-step seeding/growth method. The average diameter of the nanorods can be tuned either in the seeding step or in the growth step. Furthermore, consequences in the performance of hybrid photovoltaics as a result of tailoring the nanorod diameter are investigated, leading to a new record efficiency of 0.82% for untreated ZnO nanorod arrays in combination with P3HT. Unexpectedly, the improvement is attributed primarily to the orientation of the nanorods. Tilted nanorods can lead to more scattering of the incident light and to a possible better alignment of the P3HT backbone, which has a positive effect on the transport. It can be concluded that the morphological and electro-optical interplay between the ZnO nanorods and the P3HT, as caused by the nanorod template, is far from straightforward, but the current work offers a leading edge toward more thorough apprehension by delineating the effect of a cogent set of synthesis parameters.

3.4. Experimental section

3.4.1. Materials and methods

Patterned ITO (15 Ω/sq, Every Rich Enterprise Limited) on glass was successively cleaned by sonication in a soap solution, deionized water, acetone and in boiling isopropanol, 10 minutes each. In order to improve the wettability of the substrate for the aqueous precursor solution, this wet cleaning was followed by a 15 minutes UV-ozone treatment before deposition of the seed layer. P3HT was obtained from Rieke Metals and dissolved in chlorobenzene (Merck) by stirring at 50 °C. ZnO nanorods were synthesized using a two-step process consisting of seeding with an aqueous precursor and hydrothermal growth. Starting materials for the preparation of the aqueous Zn(II)-precursor solution were zinc oxide (ZnO, Aldrich), citric acid ($C_6H_8O_7$, Aldrich), ethylenediamine ($C_2H_4(NH_2)_2$, Merck). Zinc acetate dihydrate ($ZnAc_2.2H_2O$, Aldrich) and hexamethylenetetramine ($(CH_2)_6N_4$, HMT, Aldrich) in deionized water were used to perform the hydrothermal growth.

3.4.2. Seed layer

For the preparation of the aqueous Zn(II)-precursor with different Zn(II)-concentrations ranging from of 0.125 M up to 0.5 M, ZnO and citric acid (1:1 molar ratio) were dissolved in deionized water and the pH was adjusted to 7 using ethylenediamine.[21] The seed layer was formed by spin coating the Zn(II)-precursor at 3000 rpm for 30 seconds, followed by a subsequent thermal treatment on hot plates at 300 °C and 500 °C for 1 minute and 5 minutes, respectively. Depending on the thickness of the desired dense seed layer, this process was repeated several times. Finally, the substrates were annealed in a horizontal tube furnace for 1 h at 550 °C in an oxidizing atmosphere of dry air.

3.4.3. ZnO nanorods arrays

ZnO nanorods were formed by a hydrothermal treatment at 95 °C of seeded substrates in an equimolar aqueous solution of $ZnAc_2$ and HMT in deionized water. The length of the nanorods was tuned to 300 nm by optimizing the hydrothermal reaction time. Afterwards, the solution was cooled naturally for 1 h before the

samples were removed. The samples were then rinsed with deionized water and dried at 60 °C for 1 h.[16] The length of the nanorods scales linearly with the hydrothermal growth time and can be varied from 200 nm (27 minutes) up to 3.5 μm (225 minutes) in one growth cycle, though in the scope of this work the length is kept constant at 300 nm for every sample, as this is a relevant length for application in hybrid solar cells.

3.4.4. Photovoltaic devices

The freshly prepared ZnO arrays on ITO substrates were heated at 150 °C for 20 minutes in air and cooled with N_2 flow prior to spin coating of a P3HT solution.[22] After deposition, the samples were annealed at the melting temperature of P3HT (225 °C) in N_2 for 1 minute to enhance infiltration into the nanorod array and to enhance the crystallinity of the P3HT. Finally, 80 nm Ag top electrodes were evaporated in vacuum (10^{-6} mbar).

3.4.5. Characterization techniques

The scanning electron micrographs (SEM) of the ZnO arrays were obtained with a FEI Quanta 200FEG-SEM. The thickness of the layers was measured with cross-section SEM. X-ray diffraction (XRD) patterns were measured, using a Siemens D-5000 diffractometer with Cu-$K_{\alpha 1}$ (0.154056 nm) radiation. The atomic force micrographs (AFM) were obtained with a Veeco Dimension microscope equipped with a Digital Instruments Nanoscope III controller. Scans are performed in non-contact (tapping) mode using Si tip cantilevers with a resonance frequency of 320 kHz and a force constant of 42 N/m. Images are evaluated using the WSxM software package.[23] IV characterization was performed in air at room temperature, under an AM1.5 illumination of 100 mW/cm^2 with a Newport Oriel Class A model 91195A solar simulator.

Chapter 4

Influence of interface morphology onto the photovoltaic properties of nanopatterned ZnO/poly(3-hexylthiophene) hybrid solar cells - an impedance spectroscopy study

B. Conings, L. Baeten, H.-G. Boyen, D. Spoltore, J. D'Haen, L. Grieten, P. Wagner, M. K. Van Bael, J. V. Manca, *J. Phys. Chem. C* **2011**, *115*, 16695.

ABSTRACT

This paper focuses on the characterization of the ZnO/poly(3-hexylthiophene) (P3HT) interfaces in nanostructured hybrid solar cells aiming to elucidate the relationship between thermal treatment, local morphology and device performance. An equivalent impedimetric model for the device is proposed allowing to extract information about the ZnO/P3HT interface morphology and its impact onto the photovoltaic properties by comparing devices with and without nanopatterning. It is found that the influence of thermal treatment on performance lies solely in the interface, resulting from a different interfacial morphology of P3HT depending on which crystal direction of ZnO is present.

4.1. Introduction

In current generation organic and hybrid solar cells, the bulk heterojunction (BHJ) concept is by far the most successful one.[69, 137-140] It consists of a network of two interpenetrating phases of which typically one absorbs light and transports hole-like carriers while the other transports electrons. One of the key issues on the way to efficient BHJ photovoltaic cells is thus to gain control over the morphology of both phases and their degree of phase separation.[40, 141, 142] On the one hand, the nanoscale domain size should not exceed the exciton diffusion length in the light absorber, as part of the excitons would be lost due to recombination prior to reaching an interface for charge separation. On the other hand, an excessively small domain size would impair charge transport to the electrodes. The big challenge thus remains to harvest as much light as possible without harming charge percolation.[143-145] In that respect, vertically aligned nanostructures are well accepted to offer a great potential in the development of next-generation hybrid solar cells. A large donor-acceptor interface area is guaranteed through the high density of nanostructures and, equally important, a direct pathway towards the electrodes after exciton dissociation is assured (in contrast to BHJs). Several types of nanorod arrays (predominatly ZnO and TiO_2) have been successfully used in different types of solar cells, ranging from liquid dye-sensitized solar cells to solid-state hybrids.[85, 103, 132, 146-148] Although the highest efficiencies so far were obtained with TiO_2, the potential of ZnO cannot be overlooked. First of all, hydrothermal synthesis of single-crystalline ZnO nanorods allows for straightforward and low-cost production.[108, 109] Moreover, ZnO has a higher electron mobility than TiO_2 and it is easier to finetune its morphology.[107, 149-151]

However, TiO_2-based photovoltaics are currently well ahead of ZnO-based ones since the interfaces between the metal oxide and the electron donors are still less understood and, thus, not optimized yet in the latter case.[79, 152] At any interface in a solar cell, physical and electrical phenomena largely influence the overall performance of the device at hand and, herein, the donor-acceptor interface is the most critical one. As excitons are split close to that interface, the local morphology of the dye or polymer in the vicinity of the metal oxide is crucial for the device properties and, when optimized, can drastically increase the efficiency.[87, 89, 90, 152, 153]

To gain more insight into the different components and interfaces in complex hybrid structures, impedance spectroscopy is a popular technique. Its power results from its ability to separate events that occur at different time scales or rates, which can be exploited to isolate diffusion and recombination processes.[154, 155] Traditionally, it has been used in dye-sensitized solar cells and, more recently, in organic solar cells and hybrid structures as well.[104, 156-162] Elaborate theoretical understanding of the technique for solar cell applications is aptly described.[155, 157]

For solid-state hybrid solar cells, a particular difficulty is that the light-absorbing polymer has to be infiltrated into the already synthesized nanorod array.[87, 163] In case of P3HT as the absorber material, solvent annealing and thermal annealing have been proposed to ensure full infiltration, where the latter one is the most effective so far.[86, 87, 132] In this contribution, impedance spectroscopy will be applied to study hybrid solar cells based on ZnO nanorod arrays and P3HT, thereby focusing on interface properties and their relation with device performance upon thermal treatment. Furthermore, Charge Extraction in a Linearly Increasing Voltage (CELIV) is performed as complementary technique to obtain additional information about the charge carrier mobility of P3HT as used in devices with and without nanopatterning.

4.2. Results and discussion

Recently, we reported on the influence of thermal treatment during the fabrication of ZnO nanorod/P3HT hybrid solar cells on their photovoltaic efficiency.[132] It was discovered, that heating the polymer above its melting temperature (T_m = 225°C) for 1 minute enables it to fully infiltrate the nanorod array. Annealing considerably longer than 1 minute was found to deteriorate the device performance severely. Since UV/VIS measurements did not show any change in the optical properties of the polymer upon melting treatment, the decreasing device performance was attributed to the specific alignment of the polymer chains on top of the nanorods as discussed by Dag and coworkers,[113] thereby impeding charge transfer in the vertical direction.

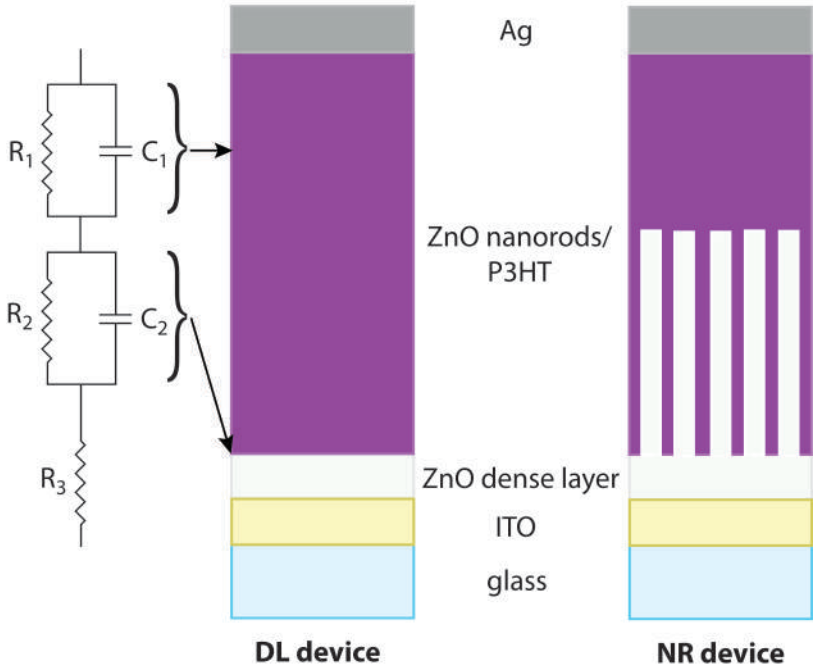

Figure 4.1. Experimental setup of a dense layer device (DL) and a nanorod device (NR), together with the proposed impedimetric model.

The basic setup of the different sample architectures (DL, NR) is sketched in Figure 4.1 together with the equivalent circuit model used to analyze the experimental data. Briefly, an ITO base electrode is covered by a dense ZnO film used as a hole blocking layer, followed by either a ZnO nanorod array filled with P3HT as the photoactive layer plus an additional P3HT layer used as electron blocking layer (NR device) or just by a pure P3HT film (DL device). In both cases, a thin Ag top electrode terminates the photovoltaic device.

In order to better understand the fundamental contributions to an impedance spectrum arising from specific parts of our device architecture, measurements were performed first on devices without nanostructuring. Figure 4.2a shows the Nyquist plot of a series of spectra acquired on a DL device for different bias-voltages (full symbols). Despite the presence of four different materials (ITO, ZnO, P3HT and Ag) and three interfaces (ITO/ZnO, ZnO/P3HT and P3HT/Ag), the spectra only contain two main features: two semi-circles with the left one revealing a small offset on the real

axis. These spectra can be analyzed according to the model proposed in Figure 4.1, thereby assuming two parallel combinations of resistors and capacitors (C_1-R_1 and C_2-R_2 representing the two semi-circles) in series with a resistor R_3 reflecting the observed small offset. The capacitors are treated as Constant Phase Elements (CPE) which allows to obtain better fits.[154, 164, 165] A CPE's impedance is defined as a complex number $Z = Q^{-1}(i\omega)^{-n}$ with Q representing a constant, ω the angular frequency and n a number between 1 (ideal capacitor) and 0 (pure resistor). A CPE is in fact a generalized imperfect capacitance that takes into account surface roughness and heterogeneities.[154, 164] In our case, extracted n-values were most often > 0.95, thus implying that deviations from a perfect capacitive behavior are negligible.

The first step towards the identification of individual circuit elements is achieved by analyzing a device with ZnO dense layer but missing polymer interlayer (see inset to Figure 4.2a). In this case, a purely ohmic behavior can be recognized with a resistance of nearly 3 Ωcm^{-2}, a value which agrees well with the serial resistance R_3 required to describe a DL device with P3HT interlayer ($3\pm1.5\ \Omega cm^{-2}$). Thus, R_3 can be assigned to the combined effect of all contributing parts with high charge carrier density and mobility (Ag top electrode, ITO base electrode, ZnO dense layer). In order to access the origin of the left semi-circle in Figure 4.2a, the thickness of the P3HT interlayer has systematically been varied from 0.65 – 1.1µm. Figure 4.2c summarizes the extracted values of C_1 as function of bias voltage for the different P3HT thicknesses. While C_1 is found to be independent of the applied bias voltage, a noticeable decrease in capacitance is observed with increasing polymer layer thickness d. This decrease in capacitance scales well with 1/d, thereby identifying the P3HT film as dielectric layer in a simple parallel plate capacitor. This picture is also confirmed by the corresponding R_1 value which is found to be directly proportional to the polymer thickness d. Consequently, the remaining elements in our impedimetric model, C_2 and R_2, are related to the right-side semi-circle, which can be assigned to the remaining ZnO/P3HT (semiconductor/semiconductor) interface, i.e. that part of our solar cell which is in the focus of interest here.

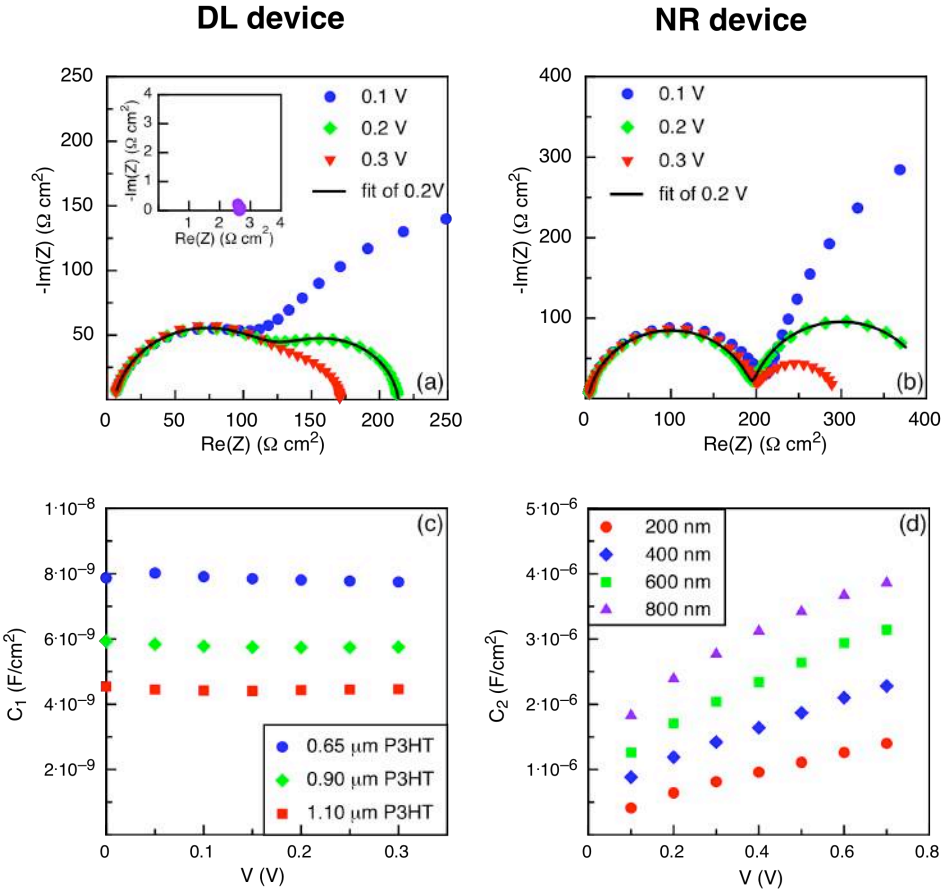

Figure 4.2. Experimental impedance spectra acquired at different bias voltages (full symbols) and corresponding fits (solid lines) of a DL device (a) and a NR device (b) applying the impedimetric model introduced in Figure 4.1; the inset to (a) shows the spectrum of a dense ZnO layer sandwiched between two electrodes (i.e. without polymer). (c) Extracted capacitance C_1 associated with the left semi-circle for different layer thicknesses of the P3HT interlayer. (d) Capacitance C_2 associated with the right semicircle in the impedance spectra for different nanorod lengths.

Turning our attention now to the NR devices, the more complex setup of the nanostructured solar cells surprisingly does not induce any additional spectral features as can be recognized in Figure 4.2b. As before, the spectra reveal two semi-circles, with the left-sided one (representing R_1 and C_1) again being independent of the applied bias voltage but shifted by a small off-set on the real axis (representing R_3), and the right-sided one being strongly bias-dependent (R_2, C_2). Since the latter

reflects the properties of the ZnO/P3HT interface, a sequence of nanostructured samples was studied in order to unravel the correlation between (R_2, C_2) and the length of the ZnO nanorods. Figure 4.2d displays the extracted C_2 value as function of bias-voltage for the different lengths. Obviously, an increased interface capacitance is induced for rising nanorod length, which indeed can be expected due to an enlarged ZnO/P3HT interfacial area. The strong dependence of C_2 on the bias voltage furthermore agrees well with observations reported earlier for donor-acceptor interfaces of several kinds of solar cells.[104, 158, 166] Longer nanorods also provide a larger interface area for charge carriers to travel through, which is expressed in a reduction of the extracted R_2 value with increasing rod length (not shown here). These results confirm the proper impedimetric description of the ZnO/P3HT interface by means of an (R, C) combination, which is also supported from a theoretical point of view.[157] Consequently, impedimetric parameters can be used as valuable tools to study changes in photovoltaic efficiency upon specific sample treatments as described in the following.

A series of DL and NR solar cells were prepared for which the melting time of the P3HT during device fabrication was varied from 1 minute to 30 minutes. Figure 4.3a and b show current-voltage (I-V) curves for both series of devices as a function of P3HT melting time. Clearly, a striking difference between both architectures can be observed: while the efficiency of the DL devices is found to dependent only weakly on the time the polymer has been in the molten state, in case of the NR devices, the short-circuit current and the open-circuit voltage both collapse upon annealing. In order to better understand the underlying changes in sample morphology, all annealing steps were monitored by impedimetric characterization as well. When analyzing the corresponding spectra using the impedimetric model as described before, important conclusions can be drawn from the extracted parameters: (i) R1 and C1 representing the dielectric properties of the polymer do not depend on melting time neither for the DL nor the NR devices. This behavior is consistent with the ability of P3HT to withstand prolonged melting times, with no change in the level of crystallinity.[132] Additional XPS measurements performed to verify the chemical state of P3HT after such heat treatments furthermore did not show any hint for

degradation effects like, e.g., the oxidation of the involved sulfur atoms, thereby indicating a high chemical stability of the polymer during melting as well. (ii) The values of R2 and C2 representing the ZnO/P3HT interface, together with the associated time constant τ (= RC), derived at a bias voltage corresponding to the open-circuit voltage, show subtle differences between the two device architectures. This is demonstrated in Figure 4.3c and d where, for DL devices, the relative values of R_2 and C_2 remain roughly constant for extended annealing times. This results in a fairly constant value of τ which nicely correlates to a nearly constant photovoltaic efficiency as seen in Figure 4.3a. In contrast, in case of the NR devices (Figure 4.3d), the extracted parameters R_2 and C_2 (and thus τ) are clearly decreasing which also correlates to a reduction in efficiency with increasing annealing time (Figure 4.3b).

Since τ can be taken as a measure for recombination processes occurring at the donor-acceptor (P3HT/ZnO) interface, a decreasing value of τ suggests that the thermal treatment considerably promotes recombination in NR devices (lower τ means higher recombination rates) whereas in DL devices it has almost no effect.[157] Since DL and NR devices only differ in the interfacial area between ZnO and P3HT, the pronounced decrease of τ observed for NR devices should be related to subtle differences in their interface morphology. While a nano-crystalline dense layer of ZnO (as used for the DL devices) consists of adjacent grains with a large distribution of crystal directions, the nanorod array is characterized by single-crystalline pillars which all are (nearly) perfectly oriented into the [002] direction (see Supporting Information on page 68). Consequently, in the former case, the morphology of the P3HT near the ZnO will reflect the statistical distribution of crystal directions of the grains, and in the latter case, the P3HT will attach to the [100]-type surfaces of the ZnO rods in the same manner all over the entire interface area (i.e., polymer backbone $\perp$ nanorods).[113] Therefore, according to the sketch depicted in Figure 4.1, for NR devices, the polymer strands in contact with the ZnO surface basically orient into the horizontal direction with superior electrical conduction along individual chains (i.e. in horizontal direction), but significantly reduced conduction in normal direction between neighboring chains after exciton splitting. This interpretation explains the decrease in photovoltaic efficiency with annealing time as being due to a reduced hole conduction towards the

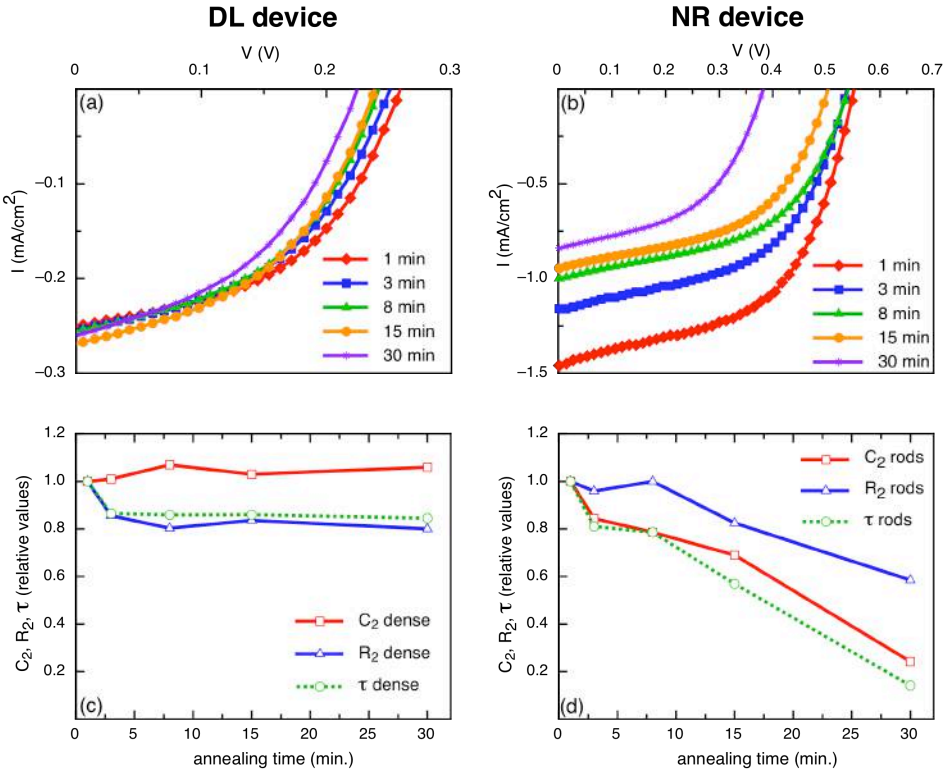

Figure 4.3. I-V curves of DL (a) and NR (b) devices that were annealed for different times during fabrication. (c) and (d) show C_2, R_2, and corresponding τ (at V_{oc}) for the devices presented in (a) and (b), respectively.

top electrode in the vicinity of the nanorod surfaces (where the excitons are split) resulting in an increased recombination rate (reduced life time) of holes which are localized on individual chains and which are able to easily move back towards the (negatively charged) nanorods. Further support for such a picture arises from the observed trends in R_2. The more time the polymer strands are provided to attach perpendicularly onto the nanorods during melting, the higher the number of pathways across the interface will be, thus explaining the decreasing value of R_2. Unfortunately, the drop in interface capacitance C_2 can hardly be explained without an appropriate theoretical treatment. On the other hand, for DL devices, the modification of interface properties as a consequence of changing P3HT morphology

is much weaker as only a small fraction of the interface area shares the same [100] direction and, thus, the resulting preferential P3HT morphology.

In order to further support the conclusions drawn above, additional measurements were performed aiming to access the hole mobility μ_h of the P3HT for the different device configurations. Charge Extraction in a Linearly Increasing Voltage (CELIV) measurements were carried out by ramping a voltage (applied to the outer electrodes) thereby probing both, the bulk and the interfacial polymer, respectively. Figure 4.4 summarizes the μ_h values acquired on three different samples: a pure P3HT layer sandwiched between ITO and Ag electrodes, a DL device and a NR device (all annealed for 30 minutes at 225°C). Obviously, the mobilities of holes in pure P3HT and P3HT within a DL device are identical, implying that the presence of a dense ZnO layer does not cause a change in the polymer's electrical properties. In contrast, μ_h in case of the NR device drops severely by a factor of 4, evidencing that the origin of the reduced mobility lies exclusively in the presence of a significantly different interface (morphology) which hinders vertical transport of holes towards the top electrode, most likely due to the alignment of the polymer chains perpendicular to the ([100]-type) nanorod surfaces as predicted earlier.[113] Although, at present, the results from the current work strongly support this latter premise, a final proof needs to be provided requiring a detailed analysis of the phase morphology and reorganization of P3HT near the different ZnO facets.

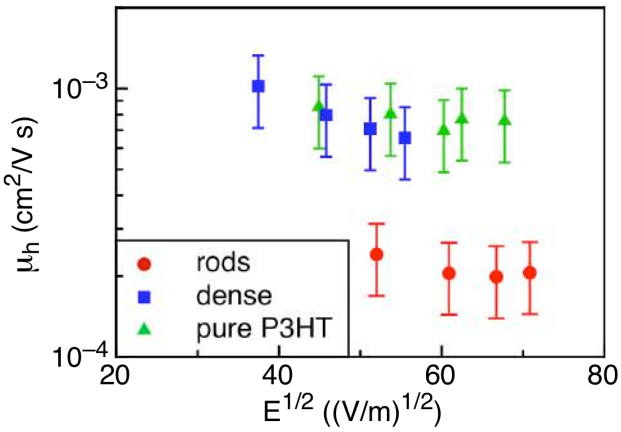

Figure 4.4. Hole mobility as a function of electric field for pure P3HT (sandwiched between ITO and Ag electrodes), for a DL device and a NR device.

4.3. Conclusion

In summary, an impedimetric model is proposed for the characterization of nanostructured ZnO/P3HT based solar cells, and its basic elements are successfully related to their physical origin. The comparison between ZnO dense layer (DL) and ZnO nanorod (NR) devices allows to investigate the response of such hybrid solar cells to a heat treatment which is required for device fabrication. The efficiency of DL devices is almost independent of the melting time of the polymer, whereas in NR devices the efficiency decreases severely upon annealing. By localizing the impedimetric parameters representing the ZnO/P3HT interface, the origin of the degradation can be traced back as being likely due to the alignment of the polymer chains perpendicular to the [100] crystal direction of the ZnO nanorods, causing increased interfacial recombination of adjacent charge carriers.

Turning this argument around, the efficiency of nanostructured hybrid solar cells might significantly be improved in the future by precisely engineering the morphology of the polymer at the nanorod/polymer interface using self-organization strategies combined with suitable organic interlayers.

4.4. Materials and methods

ZnO nanorod synthesis. ZnO nanorods were synthesized as described earlier using a two step process consisting of seeding and hydrothermal growth.[132] Briefly, the seed layer was deposited by an aqueous sol-gel method onto patterned ITO (15 Ω/sq, Every Rich Enterprise Limited). In order to improve the wettability of the substrate for the aqueous precursor solution, the wet cleaning was followed by a 15-minute UV-ozone treatment before spin coating. Next, the substrates were thermally treated to obtain a thin ZnO film of 20 nm. To vary the seed layer thickness up to 140 nm, the latter steps were repeated a number of times. The hydrothermal growth was executed at 95°C for different times, depending on the desired nanorod length, in an equimolar aqueous solution of zinc acetate dihydrate (Aldrich) and hexamethylenetetramine (Aldrich) in deionized water. Afterwards the solution was cooled down naturally for 1 h before the samples were removed. The samples were then rinsed with deionized water and dried at 60 °C for 1 h.

Photovoltaic devices. The freshly prepared ZnO coated ITO substrates were heated at 150 °C for 20 minutes in air and cooled down with N_2 flow prior to spincoating low molecular weight P3HT (Rieke Metals) solutions in chlorobenzene (Aldrich).[87] After deposition, the samples were annealed at the melting temperature of P3HT (225 °C) in N_2 for different times to enhance infiltration into the nanorods and to enhance the crystallinity of the P3HT.[132] Finally, 80 nm Ag top electrodes were evaporated in vacuum ($1 \cdot 10^{-6}$ mbar).

Solar cell characterization. IV-characterization was performed in air at room temperature, under an AM1.5 illumination of 100 mW/cm² with a Newport Oriel Class A model 91195A solar simulator. Impedance spectra (100 Hz - 5 MHz) were obtained using a HP 4194A Impedance/gain-phase analyzer, all in dark, with an oscillating voltage of 25 mV. The spectra were analyzed with ZSimpWin software (version 3.1, Princeton Applied Research). CELIV measurements were carried out applying a ramp voltage on the sample (supplied by a function generator (Tektronix AFG 3101)) and monitoring the current transient response using a digital oscilloscope (Tektronix TDS 620B). The ramp amplitude was varied which allows to extract the charge carrier mobility as a function of electric field.[167]

4.5. Supporting information

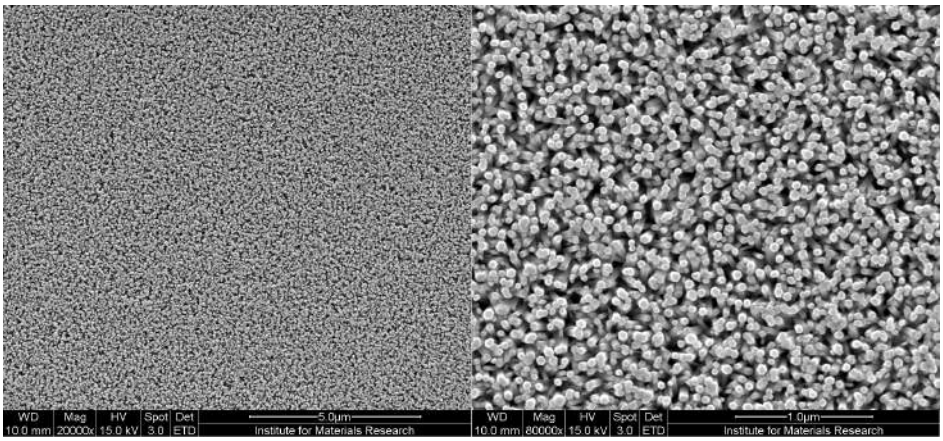

Figure 4.5. Scanning Electron Microscopy images of a ZnO nanorod array.

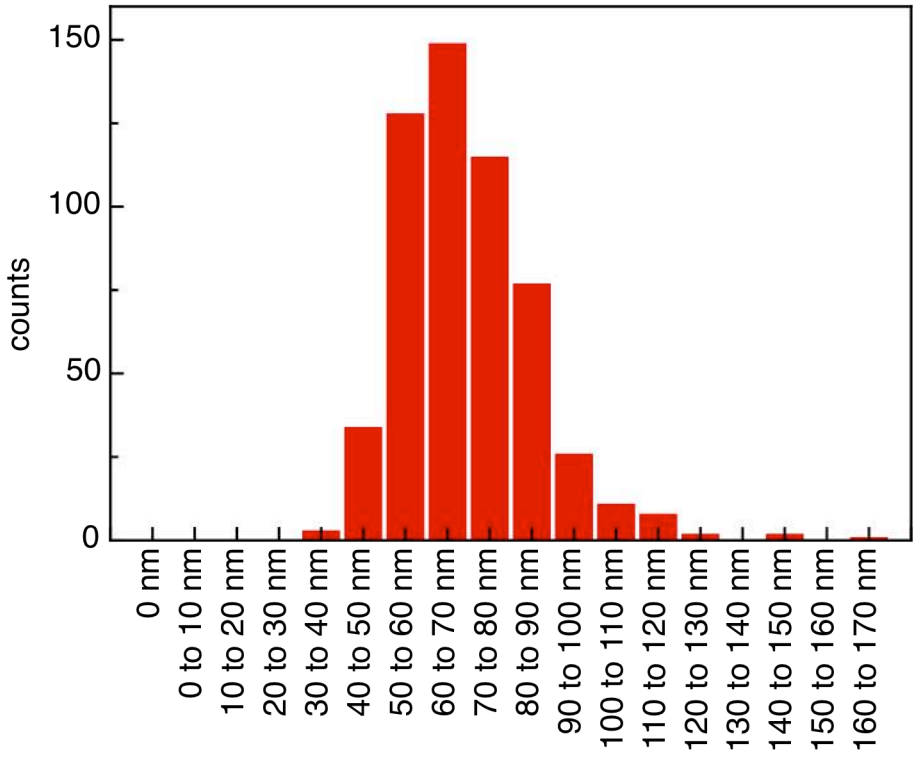

Figure 4.6. Histogram of the nanorod diameter for arrays as in Figure 4.5.

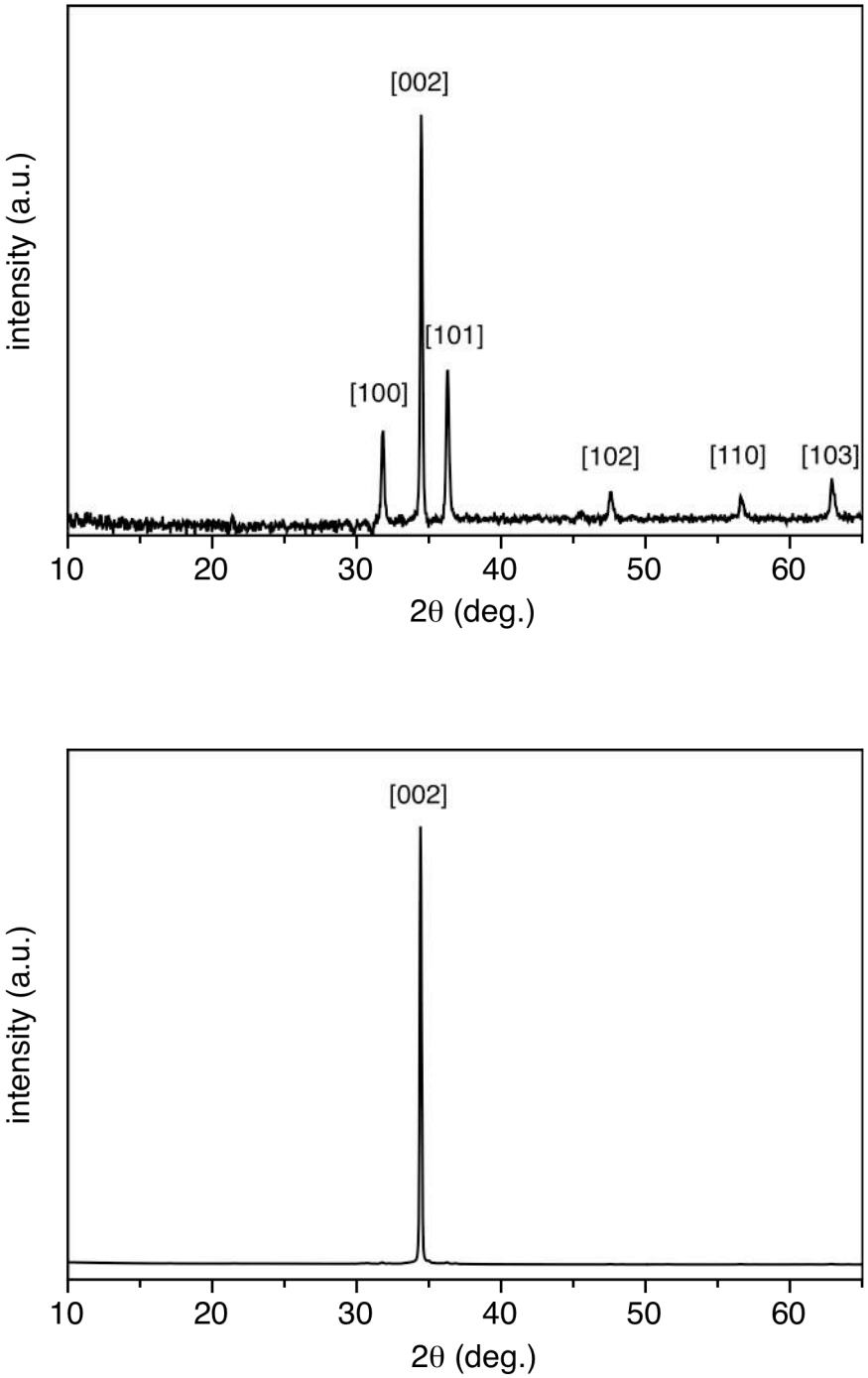

Figure 4.7. XRD spectrum of a dense ZnO layer (top) and a nanorod array (bottom).

Chapter 5

Generalized approach to the description of recombination kinetics in bulk heterojunction solar cells – extending from fully organic to hybrid solar cells

B. Conings, L. Baeten, H.-G. Boyen, D. Spoltore, J. D'Haen, M. K. Van Bael, J. V. Manca, **2012,** *under revision*.

ABSTRACT

Lately, research efforts in photovoltaics towards hybrid solar cells based on nanostructured metal oxides and conjugated polymers have been intensifying. However, very limited effort has been spent so far to investigate their recombination kinetics in comparison with their fully organic counterpart. In this work, impedance spectroscopy under different illumination intensities is used to probe the recombination kinetics of hybrid solar cells based on ZnO nanorod arrays and poly(3-hexylthiophene). A recombination-based model developed for fully organic solar cells is successfully applied in our hybrid solar cells, demonstrating their similarity in device physics and establishing the nanorod array/polymer compound as true bulk heterojunction.

5.1. Introduction

Photovoltaics have proven to be a key contender to meet the world's need for clean and sustainable energy.[168] Silicon-based solar cells find their origin in the 1950's but are still under development, the main goals now being directed not only toward performance improvement but also very much toward cost-effectiveness, which is a challenge.[3, 169] Consequently, despite their performance-wise inferiority compared to their silicon counterparts, newer types of solar cells like organic and hybrid solar cells are gaining ground primarily because of their potential for cheaper fabrication.[5, 170] The most mature device type in this respect is the organic bulk heterojunction (OBHJ) solar cell, the active layer of which consists of an interpenetrating network of a light absorbing electron-donating material and an electron-accepting material, typically a conjugated polymer and a fullerene-derivative, respectively.[171, 172] However, these OBHJ devices are more prone to temperature-driven phase separation, thus degradation, whereas hybrid (organic/inorganic) solar cells are intrinsically more stable due to their template-based morphology.[173, 174] It is well established that for OBHJ solar cells, non-geminate recombination is the main loss mechanism that limits their performance.[31, 175, 176] For hybrid solar cells, however, recombination related studies are rather scarce,[177] leaving the identification of the underlying loss mechanisms (as compared to their fully organic counterpart) still an open question. Consequently, in order to optimize hybrid solar cells in a systematic manner, the understanding of recombination dynamics in such devices urgently needs to be improved.

In this work, we demonstrate with varying light intensity impedance spectroscopy measurements that for hybrid solar cells based on ZnO nanorod arrays and poly(3-hexylthiophene) (P3HT), the presiding mechanism that governs the open circuit voltage is a strongly light intensity- and charge carrier density-dependent non-geminate recombination, together with a virtual absence of non-geminate recombination at short circuit conditions. Based on these results we demonstrate that the approach used to describe recombination kinetics in fully organic P3HT:1-(3-

methoxycarbonyl)propyl-1-phenyl-[6,6]-methano fullerene(PCBM) devices can be generalized and extended to hybrid solar cells.

In order to uncover the device physics of OBHJ solar cells, the combination of P3HT and PCBM has been and still is the most frequently used model system, even though its performance has been surpassed by combinations of low-bandgap polymers and novel PCBM-derivatives.[20, 94] In contrast to the widespread assumption of a simple binary mixture of both materials within a corresponding thin film,[34, 178] a thin layer of P3HT:PCBM is dominated by a rather complex film morphology comprising crystalline P3HT domains, crystalline PCBM domains, and compound domains of both amorphous P3HT and PCBM, being subject to both horizontal and vertical phase separation.[40, 41] The formation of these different kinds of domains is inherent to solution processing, for which the resulting film microstructure is strongly dependent on solvent, drying time, possible additives and annealing treatments.[40, 179-181] Naturally, microstructure affects device performance, and much effort has been undertaken to reveal correlations between domain size and photocurrent as well as charge recombination.[178, 182, 183] However, the intricacy of controlling domain size and structure makes the investigation of recombination dynamics equally challenging. Template-based solar cells enable more control over morphology as they are fabricated in a two-step process where the "template" acceptor part is pre-synthesized and subsequently infiltrated by the donor part.[85, 132] This type of devices could thereby help designing recombination dynamics-related experiments that rely on careful control over morphology. A suitable platform for this purpose is the combination of ZnO nanorod arrays and P3HT, which was introduced in 2006 by Olson and co-workers, followed by regular improvements in performance and basic understanding.[85, 136, 184] We demonstrated recently that by tuning the morphology of the nanorod array together with the bulk and interfacial P3HT morphologies, the performance of these devices can be systematically manipulated and optimized, with efficiencies passing 0.8 % so far.[136, 185]

5.2. Results and discussion

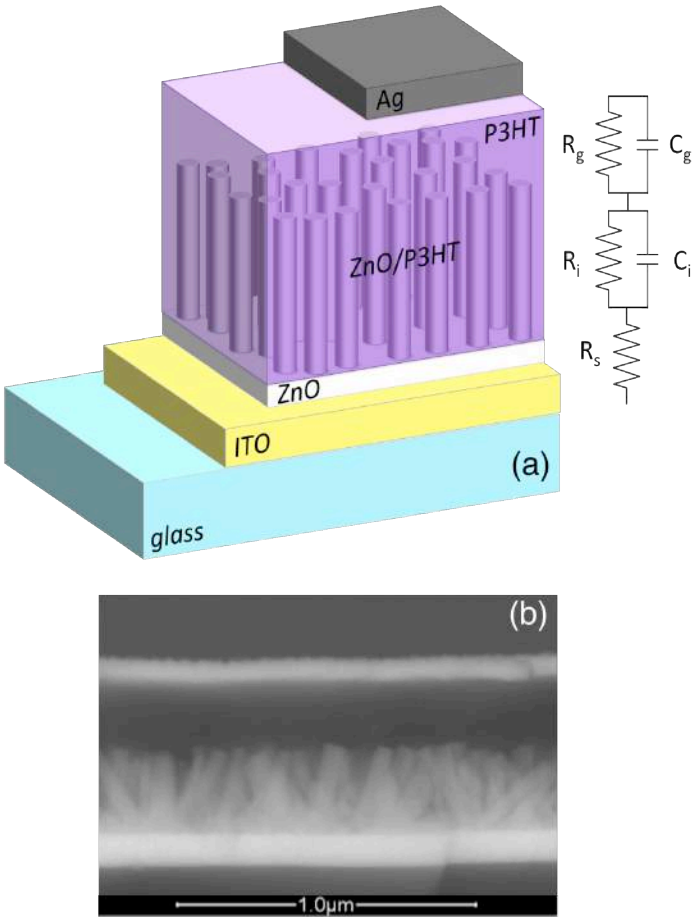

Figure 5.1.(a) Hybrid ZnO nanorod array/P3HT device structure with corresponding equivalent circuit and (b) Cross-section Scanning Electron Micrograph of a typical device.

Figure 5.1a illustrates the device setup of such solar cells, together with their equivalent circuit as identified earlier, part of which will be further exploited in this work.[136] A corresponding SEM image is depicted in Figure 5.1b, where the brightest areas delineate the ITO (bottom) and the Ag (top) electrode. For this work a range of devices was prepared, thereby varying parameters such as nanorod length, diameter

and spacing, as well as thermal treatment of the polymer, as described elsewhere.[132, 185]

A first hint towards the recombination behavior of photo-excited charge carriers is provided by the dependence of the short circuit current J_{sc} as well as the open circuit voltage V_{oc} on light intensity. A representative example is given in Figure 5.2, covering a wide range of light intensities varying from 0.001 to 1 sun. J_{sc} follows a power law dependence on illumination intensity, $J_{sc} \sim I^{\alpha}$ with $\alpha > 0.95$, which is very similar to values reported for P3HT:PCBM cells in the literature.[183, 186] This indicates a very limited presence of space-charge buildup[187, 188], and suggests the absence of a strong non-geminate recombination at short circuit conditions.[175] Simultaneously, V_{oc} depends linearly on the logarithm of the light intensity, as was also observed for fully organic solar cells.[189] The slope of the curve is unaffected by processing conditions, which implies a steady amount of trap-assisted recombination.[190, 191]

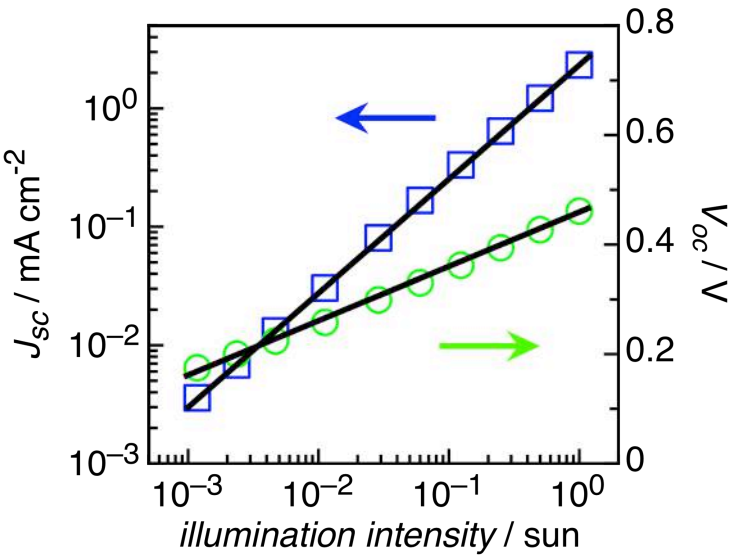

Figure 5.2. Light intensity dependence of short circuit current and open circuit voltage for a typical hybrid ZnO nanorod array/P3HT device. The black lines indicate their power law and logarithmic behavior, respectively.

Aiming to unravel the similarities/differences between hybrid and organic solar cells regarding recombination kinetics, we adopt a model recently developed for organic solar cells by the Durrant group, which is based on matching the flux of photogenerated charges with the flux of non-geminate recombination.[175] Accordingly, the total current extracted from a solar cell can be considered to arise from two contributions, namely the photocurrent (resulting from illumination) and, in opposite direction, the loss current.[175, 192]

$$J(V) = J_{photo}(V) + J_{loss}(V) \quad (5.1)$$

The loss current J_{loss} can be estimated from the charge carrier density and lifetime under illumination by[175, 193]

$$J_{loss} = ed\frac{n(V_{oc})}{\tau_n(V_{oc})} \quad (5.2)$$

e representing the elementary charge, *d* the active layer thickness, *n* the average charge carrier density, and τ_n the average charge carrier lifetime.

Charge carrier densities and loss mechanisms in solar cells have been investigated before by a variety of techniques, including transient absorption spectroscopy[194-196],

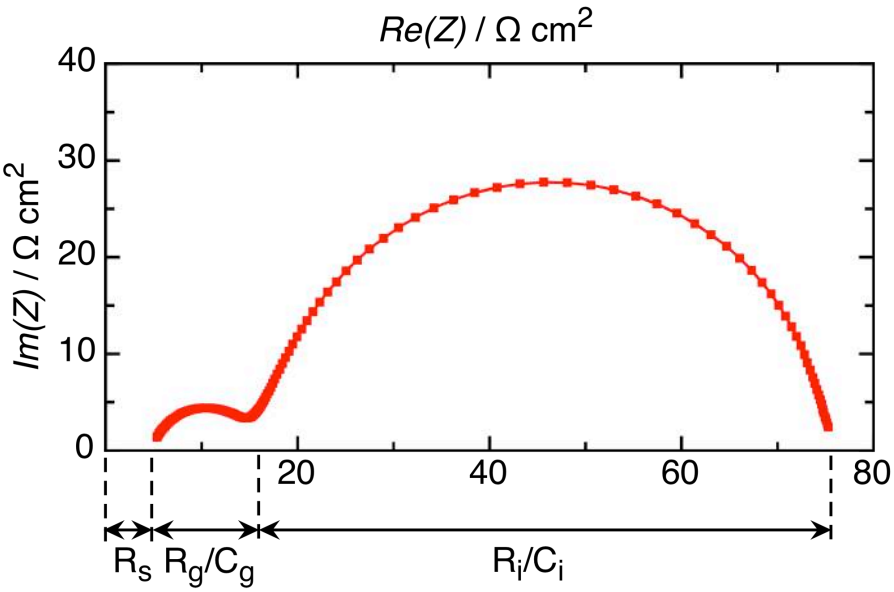

Figure 5.3. Typical impedance spectrum revealing the equivalent circuit elements as indicated in Figure 5.1a.

transient photovoltage (TPV) and photocurrent (TPC)[195, 197-199], time-of-flight[200-202] and impedance spectroscopy[161, 191, 203]. Here, we use impedance spectroscopy to probe the charge carrier densities and lifetimes for ZnO nanorod array/P3HT solar cells. The main asset of impedance spectroscopy is that it can easily distinguish between different phenomena occurring in the same device, such as diffusion and recombination processes. During a measurement, a signal consisting of a small sinusoidal voltage $V_{ac}(\omega)$ superimposed on a bias voltage V_{dc} is applied to the device, thereby allowing to measure the current output $J_{ac}(\omega)$ with high precision using lock-in technology. The complex impedance is then given by:

$$Z(\omega) = Z'(\omega) + iZ''(\omega) = \frac{V_{dc}+V_{ac}(\omega)}{J_{ac}(\omega)} \quad (5.3)$$

Acquiring $Z(\omega)$ for ZnO nanorod array/P3HT solar cells for a range of frequencies yields spectra that typically contain features as can be seen in Figure 5.3. These spectral features can be used to identify the underlying physical parameters, which allows to assign them to circuit elements as indicated in Figure 5.1a.[136] Here, resistor R_s represents the series resistance created by the electrodes (offset on the real axis, thus representing a purely ohmic contribution). The parallel combination of R_g and C_g stands for the geometric (volume) contribution of the polymer (left semicircle), while the parallel elements R_i and C_i put forward the interface between ZnO and P3HT (bias-dependent right semicircle). It is the latter R_i and C_i combination that will be focused on in this work as it provides easy access to the photogenerated carrier recombination (R_i) and storage (C_i) at the donor/acceptor interface. Additionally, it defines a time constant $\tau_{\Delta n} = R_iC_i$ that represents the corresponding small-perturbation charge carrier lifetime.

Charge carrier density and lifetime are highly dependent on solar cell working conditions, and can only be properly obtained by considering a small perturbation of a steady-state.[204] This steady-state condition is created, for each light intensity, by biasing the cell with the appropriate V_{oc}, i.e., the voltage which allows to completely suppress the total current flowing through the cell. Subsequently, a small perturbation is created by superimposing a small oscillating voltage V_{ac} thus giving impedance spectroscopy the intrinsic advantage that the measurement is not affected

by charging effects that are known to cause problems in TPV and TPC measurements.[191] Repeating this procedure for different light intensities thus enables to access the dependence of the charge carrier density *n* and small-perturbation lifetime $\tau_{\Delta n}$ on V_{oc} by using the following relations:[175]

$$n = n_0 e^{\gamma V_{oc}} \tag{5.4}$$

$$\tau_{\Delta n} = \tau_{\Delta n_0} e^{-\beta V_{oc}} \tag{5.5}$$

Here, *n* is calculated by integration of the capacitance C_i at each V_{oc} value:

$$n = \frac{1}{ed} \int_0^{V_{oc}} C_i(V) \mathrm{d}V \tag{5.6}$$

with *d* the active layer thickness. This is an established technique also used in case of TPV, and equivalent to a direct measurement of *n* using charge extraction (CE).[166, 175, 195] Inserting now Equation 5.4 and 5.5 into Equation 5.2 and considering that the effective lifetime depends on the small-perturbation lifetime as $\tau_n = (1+\beta/\gamma)\tau_{\Delta n}$[175, 205] results in an alternative expression of the loss current:

$$J_{loss} = \frac{e d n_0 e^{V_{oc}(\beta+\gamma)}}{(1+\beta/\gamma)\tau_{\Delta n_0}} \tag{5.7}$$

By taking into account that, at open circuit condition, $J_{loss} = J_{sc}$,[175, 206] from Equation 5.7 an expression for V_{oc} can be derived:

$$V_{oc} = \frac{1}{\beta+\gamma} ln \left[\frac{(1+\beta/\gamma)\tau_{\Delta n_0} J_{sc}}{e d n_0}\right] \tag{5.8}$$

Figure 5.4a shows *n* and $\tau_{\Delta n}$ as a function of V_{oc} for a typical solar cell. *n* shows an exponential behavior with respect to V_{oc}, which justifies a fit according to Equation 5.4 to extract the values of n_0 and γ. A negative exponential trend is observed for $\tau_{\Delta n}(V_{oc})$, allowing to obtain $\tau_{\Delta n_0}$ and β by fitting to Equation 5.5. Inserting these values in Equation 5.8 ultimately results in an independent prediction of V_{oc}, using exclusively the above mentioned circuit elements derived experimentally by means of impedance spectroscopy. This now enables us to compare with V_{oc} values extracted directly from corresponding J/V curves and, therefore, to critically test the applicability of the model (which was established using purely organic solar cells) to hybrid photovoltaic devices. Figure 5.4b contains the V_{oc} values extracted using the above formalism as compared to experimentally determined V_{oc} values measured on a number of solar cells prepared in various degrees of optimization.[132, 185] The

correlation between measured and calculated values of V_{oc} is excellent, with an average deviation of 10 mV. This result gives strong confidence that the most essential conceptions with respect to recombination kinetics of organic photovoltaics are also valid in metal-oxide/polymer solar cells. The successful application of the model suggests that the idea of a sustained quasi-Fermi level for holes in the strongly p-doped P3HT and a light intensity dependent quasi-Fermi level for electrons, as adopted for P3HT:PCBM, is also valid for the hybrid ZnO/P3HT system and substantiates the equivalency of PCBM and ZnO in this sense.[31, 166, 206] In both cases, the presiding mechanism that governs the open circuit voltage is a strongly light intensity- and, thus, charge carrier density-dependent non-geminate recombination, together with a virtual absence of non-geminate recombination at short circuit conditions as evidenced by the nearly linear dependence of J_{sc} on light intensity (Figure 5.2).[175] Additionally, the nanorod array/polymer compound can now be morphologically considered as true bulk heterojunction since the presence of direct pathways for charge carriers instead of sinuous percolative ones does not appear to induce a divergent recombination signature.

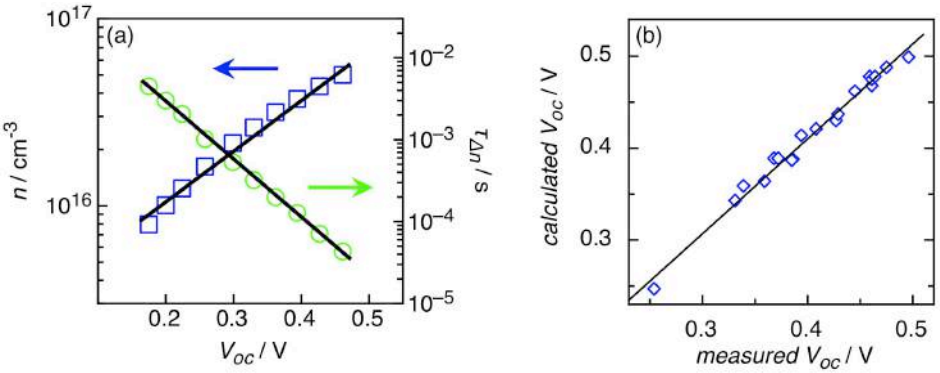

Figure 5.4. Typical behavior of charge carrier density and small-perturbation carrier lifetime obtained from impedance spectroscopy measurements as a function of $V_{oc.}$ Black lines are fits to the data. (b) Calculated values of V_{oc} by means of Equation 5.8 versus measured values of V_{oc} for a representative selection of solar cells in various degrees of optimization.[132, 185]

5.3. Conclusion

In summary, a light intensity-dependent study reveals for the first time that hybrid solar cells based on ZnO nanorod arrays and P3HT function according to the same basic principles of photo-excitation and recombination as found for the model system P3HT:PCBM. This finding is achieved by extracting voltage-dependent charge carrier densities and lifetimes by means of impedance spectroscopy, serving as input parameters for a recombination model developed for purely organic solar cells. The predicted values for V_{oc} are accurately confirmed by experiment, thereby extending the validity range of the recombination model towards inorganic/organic hybrid solar cells and, consequently, towards a more general applicability. This result conclusively demonstrates that hybrid and organic photovoltaics can be treated equally from a device physics point of view and thus provides confidence that fundamental recombination-related insights are interchangeable between them.

5.4. Experimental details

ZnO nanorod synthesis. ZnO nanorods were synthesized using a two step process consisting of seeding and hydrothermal growth.[132] In short, after a wet cleaning, the seed layer was deposited by an aqueous sol-gel method onto patterned ITO (15 Ω/sq, Every Rich Enterprise Limited). After spincoating, the substrates were thermally treated to obtain a thin ZnO film of 20 nm. The hydrothermal growth was executed at 95°C for different times, depending on the desired nanorod length, in an equimolar aqueous solution of zinc acetate dihydrate (Aldrich) and hexamethylenetetramine (Aldrich) in deionized water. Afterwards the solution was cooled down naturally for 1 h before the samples were removed. The samples were then rinsed with deionized water and dried at 60 °C for 1 h. To obtain different rod thicknesses, the concentration of the precursor solutions was varied, as described elsewhere.[185]

Photovoltaic devices. Freshly prepared ZnO coated ITO substrates were heated at 150 °C for 20 minutes in air and cooled down with N_2 flow prior to spincoating low molecular weight P3HT (Rieke Metals) solutions in chlorobenzene (Aldrich).[87] After deposition, the samples were annealed at the melting temperature of P3HT (225 °C) in N_2 for different times to enhance infiltration into the nanorods and to enhance the

crystallinity of the P3HT.[132] Finally, 80 nm Ag top electrodes were evaporated in vacuum ($1 \cdot 10^{-6}$ mbar).

Impedance Spectroscopy. Impedance spectra (100 Hz - 5 MHz) were obtained using a HP 4194A Impedance/gain-phase analyzer, with an oscillating voltage of 25 mV. A 40W white LED, in combination with a neutral density filter, was used to light the solar cells with varying light intensity from 0.001 to 1 sun. Impedance spectra were analyzed with ZSimpWin software (version 3.1, Princeton Applied Research).

Chapter 6

Relation between morphology and recombination kinetics in nanostructured hybrid solar cells

B. Conings, L. Baeten, H.-G. Boyen, J. D'Haen, M. K. Van Bael, J. V. Manca, **2012,** *submitted*.

ABSTRACT

Systematic performance improvement of excitonic solar cells hinges on thorough knowledge of their main loss mechanisms. Accordingly, the study of recombination kinetics is indispensable, enabling to identify and quantify what is considered the most important loss pathway for such devices. In contrast to the advances made in controlling the morphology of organic bulk heterojunction solar cells, it remains challenging to establish a robust correlation between morphology and recombination kinetics. Most obvious culprits are the rather disordered nature of most heterojunctions and the absence of phase purity. In that respect, hybrid solar cells based on ZnO nanorod arrays and poly(3-hexylthiophene) can offer a convenient means to study recombination, as their morphology is easier to control and to quantify. Therefore, tunability of bulk and interfacial morphology of such solar cells is utilized in this work to evidence a direct relation between morphology, recombination kinetics and device performance.

6.1. Introduction

In recent years, organic photovoltaics (OPV) have been catching the attention of many scientists, arising from their potential to supersede today's most marketable Si solar cells.[207] The key asset of OPV is the possibility to print them roll-to-roll on flexible substrates (mostly PET and even paper[208]), providing a high throughput and low cost manufacturing process compared to the challenging task of producing Si solar cells.[11] High efficiency operation of an organic solar cell relies upon many aspects, with one of the most important being meticulous control over active layer morphology.[138] Often used strategies to finetune the morphology are solvent optimization, thermal annealing, solvent annealing and the addition of additives to the blend solution.[209-212] Many advances have been made in the determination of the microstructure in such devices. Atomic Force Microscopy (AFM), Bright Field Transmission Electron Microscopy (BF-TEM), Energy-Filtered TEM (EF-TEM) as well as Electron tomography (ET) have provided many useful insights.[41, 69, 179, 213-217] However, they do not provide easy access to the understanding of recombination behavior, a key aspect for device performance that is also related to the active layer microstructure. Changes in blend morphology, as detected by imaging methods, have been shown to significantly influence geminate[218] and non-geminate recombination[183]. However, deducing recombination behavior directly from imaging is not straightforward and certainly not quantitative. Hamilton et al. elaborated on this issue by using numerical modeling to demonstrate that the difference in device performance between pristine and annealed poly(3-hexylthiophene) (P3HT):PCBM can be explained solely by varying extents of recombination due to a change in domain size.[183] The necessity for numerical modeling to unravel the correlation between microstructure and recombination parameters illustrates the inherent investigative hurdle arising from the disordered morphology.

This paper investigates the influence of microstructure on recombination kinetics by exploiting the tunability and easy-to-evaluate morphology of nanorod array-based hybrid solar cells, enabling to pinpoint the relation between active layer morphology and charge carrier density/lifetime. Several sets of ZnO/P3HT solar cells are prepared and characterized with impedance spectroscopy, allowing us to extract device

parameters using a previously deduced equivalent circuit model[136] and to relate the results to the morphology and the performance of the devices.

6.2. Results and discussion

In the quest for the ultimate bulk heterojunction morphology, nanorods arrays have been deemed the most favorable choice, as they assist in charge transport and heterojunction area enhancement.[219] Among others, this concept is being applied in hybrid solar cells based on P3HT-infiltrated nanorod arrays of ZnO. We demonstrated the effect of morphological variations in both the bulk materials and at the heterojunction interface on device performance.[132, 185] Impedance spectroscopy was introduced as a powerful characterization tool to relate changes in device performance to local morphology[136] and, most recently, to examine the recombination behavior of such devices in comparison with fully organic disordered bulk heterojunctions.[220] Here we explore how morphological changes affect the recombination kinetics of ZnO nanorod array/P3HT solar cells by taking advantage of their widely controllable morphology. The basic device architecture is illustrated in Figure 6.1, which shows a typical cell with 300 nm long nanorods with average diameter of 70 nm. To this end, 3 sets of devices were prepared, with individual cells of each set varying in one key aspect. For each cell, relevant properties and photovoltaic parameters are given in Table 6.1. Set A consists of four solar cells with different thermal history during fabrication, set B comprises three solar cells with different nanorod length, and set C contains four solar cells with different nanorod diameter and spacing. It is well known that, upon device fabrication, a thermal treatment is required to ensure full infiltration of P3HT into a nanorod array.[87] We found that the best efficiency is reached by annealing for 1 minute at the melting temperature of P3HT (225°C), with a longer treatment being detrimental for device performance.[132] An impedimetric study performed in the absence of light suggested that this phenomenon is induced by the local morphology of the P3HT at the interface with ZnO.[136] Here, we revisit this experiment as a function of light intensity to find out the impact on the kinetics of recombination, aiming to define more accurately the electronic impact of thermal treatment.

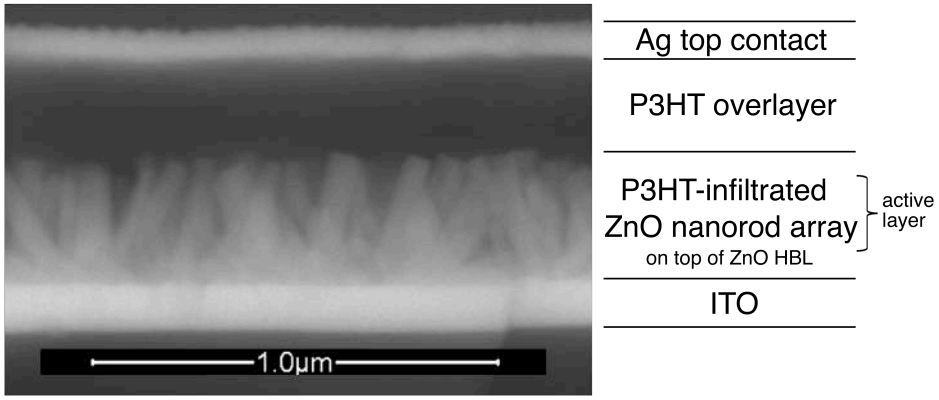

Figure 6.1. SEM image of cell A2, with indications of each part. The ZnO seed layer, which also serves as hole blocking layer (HBL) is not separately indicated because of its small thickness (20 nm).

Table 6.1. Nanorod array characteristics and photovoltaic parameters obtained under AM 1.5 illumination for all solar cells in this work.

device	rod length (nm)	rod diameter (nm)	area enhancement factor [a]	anneal time (min)	J_{sc} (mA/cm^2)	V_{oc} (V)	*FF*	η (%)
A0	300	70	10.9	0	0.77	0.431	0.483	0.160
A1	300	70	10.9	1	1.77	0.630	0.546	0.608
A8	300	70	10.9	8	1.28	0.485	0.523	0.325
A15	300	70	10.9	15	1.15	0.326	0.462	0.174
B300	300	70	10.9	1	1.41	0.604	0.598	0.509
B450	450	70	18.9	1	1.95	0.580	0.595	0.674
B600	600	70	24.9	1	2.73	0.544	0.548	0.814
C1	300	40	10.9	1	1.05	0.608	0.607	0.388
C2	300	70	10.9	1	1.57	0.603	0.598	0.565
C3	300	110	4.20	1	0.43	0.608	0.541	0.141
C4	300	50	3.40	1	2.64	0.565	0.547	0.818

[a] the area enhancement factor denotes the ratio of actual donor-acceptor area to device area.

To this end, sample set A was prepared, which consists of devices that differ only in P3HT melting time during device fabrication. The charge carrier lifetime $\tau_{\Delta n}$ (which is established by a small perturbation of a steady state, *ergo* V_{oc})[157] of devices A1 through A4 is presented in Figure 6.2 as a function of charge carrier density *n*. Here, $\tau_{\Delta n}$ results from the resistor-capacitor combination in the impedance spectrum that represents the heterojunction interface, and is referred to as the small-perturbation charge carrier lifetime.[136, 220] The charge carier density *n* [cm^{-3}] is calculated by the differential capacitance according to:

$$n = \frac{1}{ed}\int_0^{V_{oc}} C(V)\mathrm{d}V \qquad (6.1)$$

where e is the elementary charge and d the active layer thickness.[175, 195]

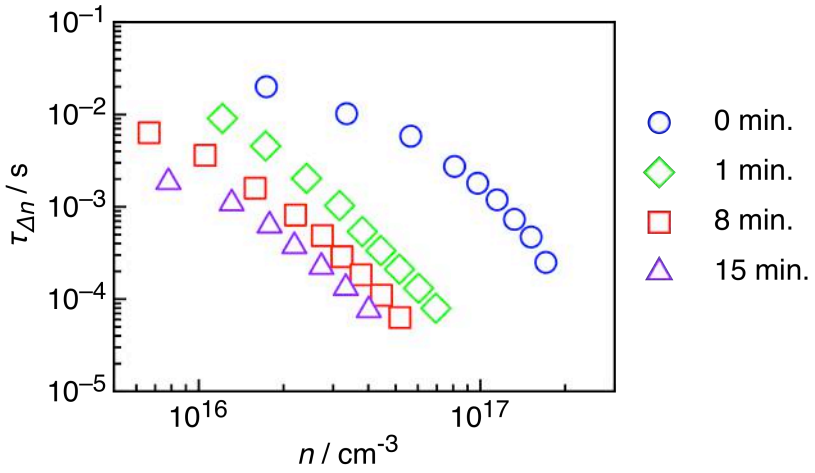

Figure 6.2. Charge carrier lifetime $\tau_{\Delta n}$ versus charge carrier density n for device set A. The legend indicates the P3HT melting time for each cell during device fabrication.

Comparing cells A1 (1 minute of annealing), A8 (8 minutes) and A15 (15 minutes), clearly there is a decrease in *n* upon melting time, albeit a modest one, while $\tau_{\Delta n}$ decreases up to one order of magnitude. These observations are in accordance with the reduction in performance upon melting time, and support our former hypothesis that the interface morphology of P3HT stimulates recombination. At first glance, the behavior of $\tau_{\Delta n}(n)$ for the 0-minute case (A0) seems surprising. Despite the low performance of this solar cell, it exhibits markedly higher charge carrier densities and

lifetimes than the other devices of set A. An explanation for this contrasting response must lie in the less intimate contact between ZnO and P3HT, which is known to be the case for pristine (unannealed) devices.[87, 132] Additionally, unannealed P3HT has a significantly lower mobility,[221] which hinders proper charge transport and could thus induce a higher local charge density.

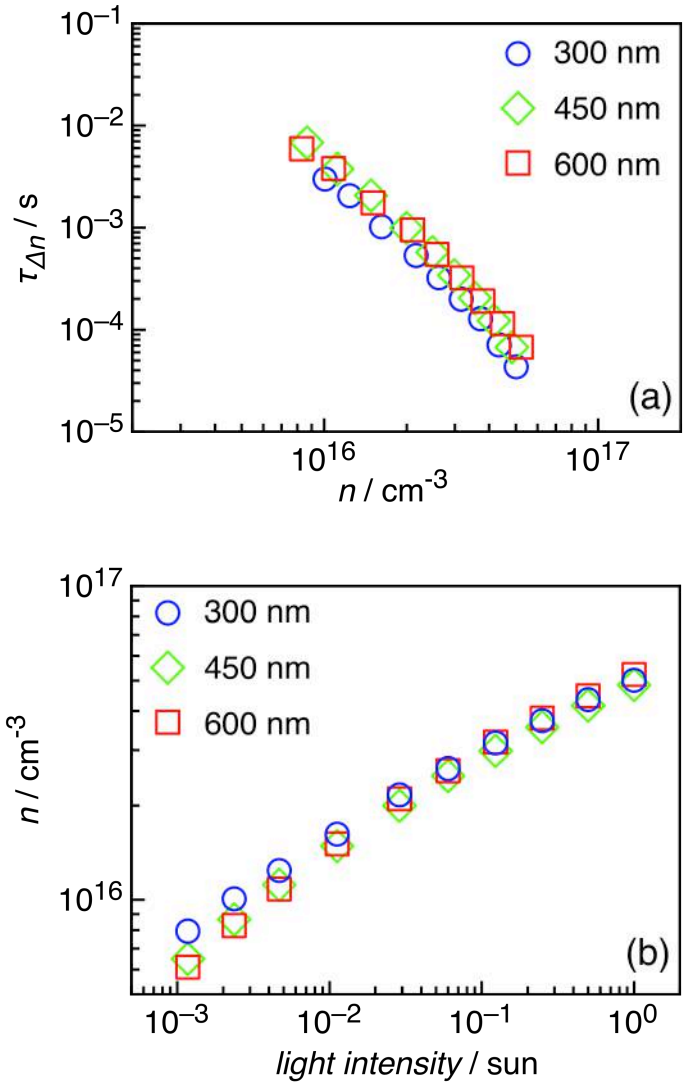

Figure 6.3. (a) Charge carrier lifetime as a function of charge carrier density devices of set B (differing in nanorod length, see legend) and (b) corresponding dependence of the charge carrier density on the light intensity.

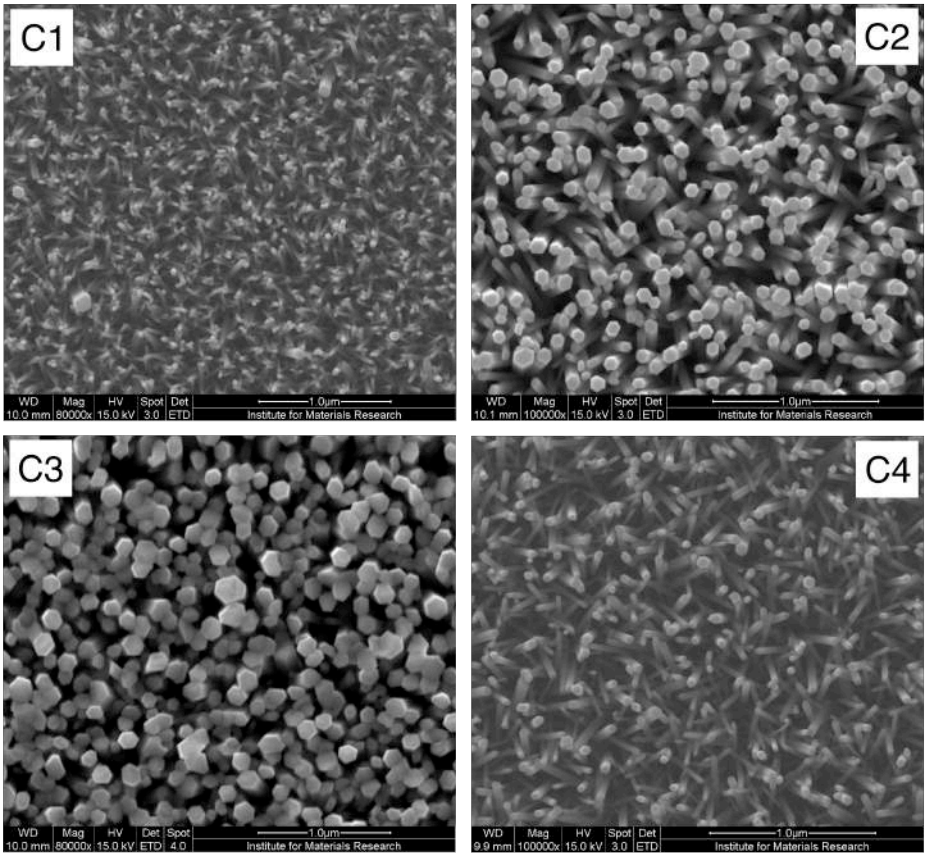

Figure 6.4. SEM images of nanorod arrays used for the devices of set C (see Table 6.1).

Two additional device sets B and C were prepared in which the hydrothermal growth conditions of the nanorods were varied.[185] Set B consists of three devices with different nanorod length (B300, B450 and B600) and set C contains four devices with different nanorod diameter and spacing (see Figure 6.4). In Figure 6.3a, it can be seen that the data from all three cells of set B are nearly coinciding. From this observation, and realizing that the calculation of the charge carrier density (Equation 6.1) takes into account the thickness d of the active layer (as indicated in Figure 6.1), it can be inferred that varying the nanorod length has very little influence on the recombination kinetics. This proves that the amount of recombination is directly proportional to the interfacial area of ZnO and P3HT (keeping in mind that the side planes of the nanorod have much larger area than the top). Straightforward as

this seems, it cannot be demonstrated for P3HT:PCBM because of its three-phase character, and even for true two-phase bulk heterojunctions the interfacial area of donor and acceptor is hard to control. Moreover, the observation implies that the transport properties must be unchanged, i.e. increasing nanorod length does not impede proper charge transport (at least up to 600 nm), otherwise there would be differences in n and $\tau_{\Delta n}(n)$. Figure 6.3b shows that at the same light intensity, the charge carrier density for each device of set B is virtually identical, which is an additional confirmation of their mechanistic equivalence.

Set C offers the possibility to further elaborate the relation between interfacial area and recombination. Each cell of this set contains ZnO nanorods with different diameter and spacing, which is reflected in a different interfacial area with P3HT. Table 6.1 contains the area enhancement factor of the nanorod arrays (ratio of actual interfacial ZnO/P3HT area to device area), determined with image analysis software from corresponding SEM images (see Figure 6.4). Significant shifts in $\tau_{\Delta n}$ and n appear to exist along the cells of set C, as judged by a. The same trend is found when plotting n versus the light intensity. Within a simplified picture, one would expect that the effective charge carrier density within the active layer (as indicated in Figure 6.1) is higher in a device with more donor-acceptor interfacial area, provided that the nanorod length is unchanged. Therefore, and building on the fact that interfacial area is governed by nanorod diameter and spacing, it makes sense to reprocess Figure 6.5, now correcting for the specific interfacial area enhancement of each individual cell. Figure 6.6 shows the same data as Figure 6.5, but $\tau_{\Delta n}$ is now expressed as a function of the area-corrected charge carrier density n_{corr}, expressed in units cm^{-2} (active layer interfacial donor-acceptor area). Focusing first on devices C1-C3, it is immediately clear that their $\tau_{\Delta n}(n_{corr})$ curves (Figure 6.6a) neatly coincide, as do their dependencies of n_{corr} on light intensity. This equivalency, revealed solely by correcting for the area enhancement factor, points to the fact that the dynamics of recombination are identical, and uninfluenced by the different nanorod diameter and spacing. Cell C4 is different from the rest of set C in the sense that it contains considerably more tilted nanorods with very low area enhancement factor (*ergo* low donor-acceptor interfacial area). Despite the latter, this device is the most efficient one of the set.

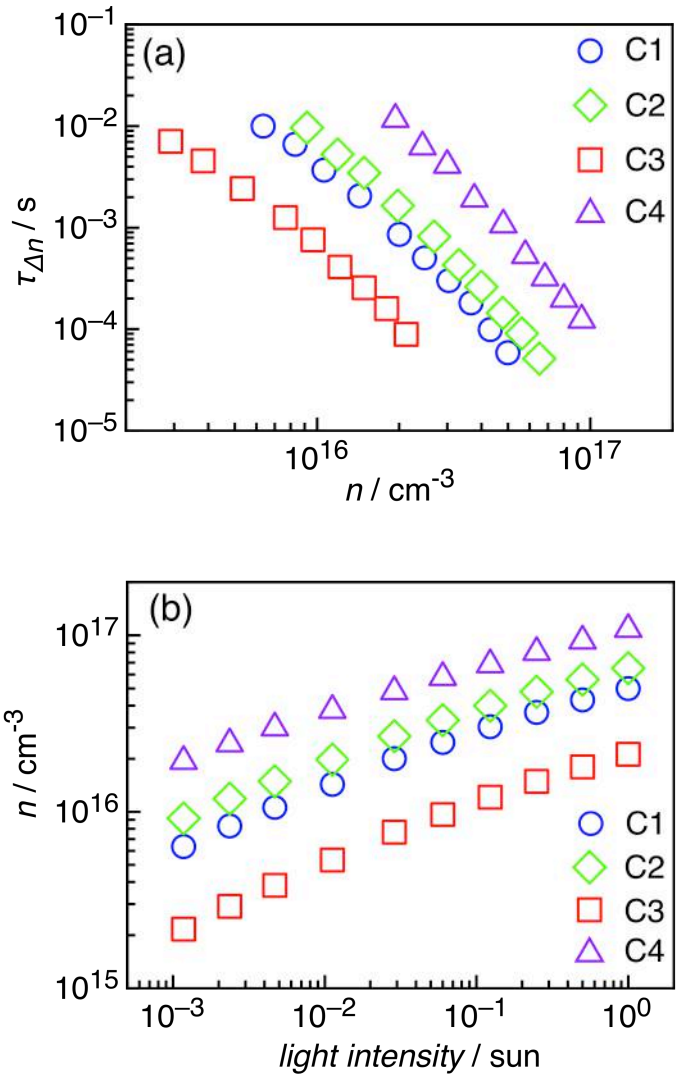

Figure 6.5. (a) Charge carrier lifetime versus charge carrier density for device set D with (b) the corresponding dependence of the charge carrier density on the light intensity.

This is further illustrated in Figure 6.7, where the short circuit current for devices of set B and C are plotted against the area enhancement factor. All devices exhibit a nearly linear dependence on area enhancement factor, which supports the rest of our findings, except device C4 produces an extremely high current as compared to the others. We attributed this effect before to the more disordered nature of the

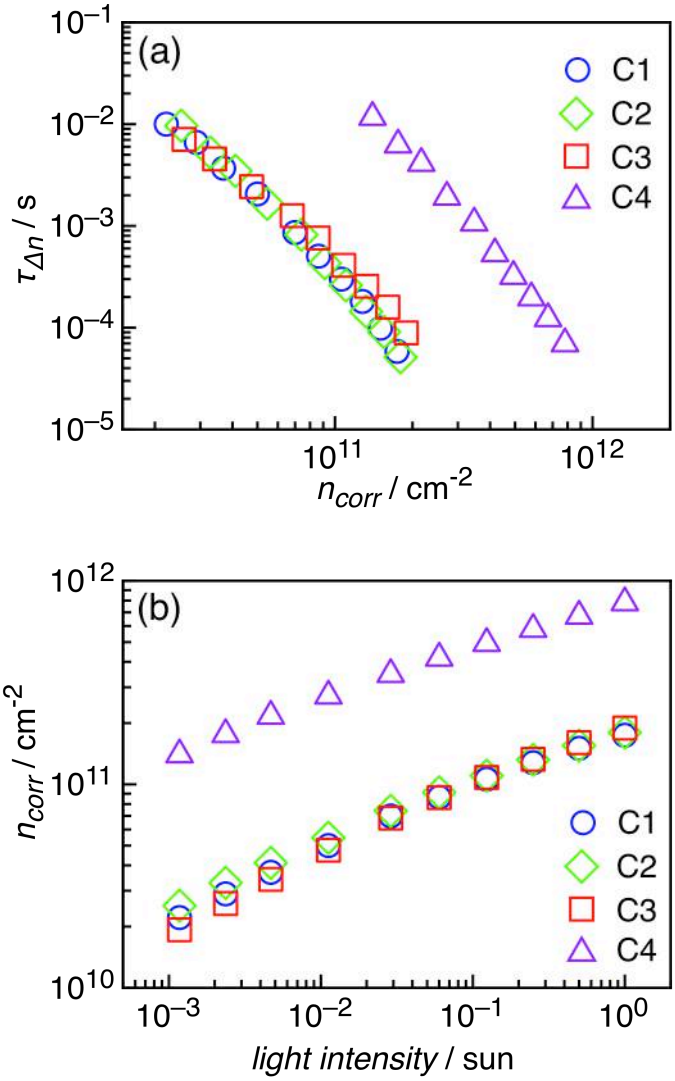

Figure 6.6. (a) Charge carrier lifetime as a function of the charge carrier density, which is corrected for the area enhancement factor and (b) the corresponding dependence of the area enhancement factor corrected charge carrier density on light intensity.

nanorod array, possibly inducing more light scattering and better charge transport.[185] Figure 6.5 and Figure 6.6 now show that cell C4 also exhibits a very high charge carrier density and lifetime. When correcting for interfacial area (Figure 6.6), the $\tau_{\Delta n}(n_{corr})$ curve of C4 does not coincide with the other devices in set C, and the difference with C1-C3 is even more pronounced than in Figure 6.5. For the same light intensities,

$\tau_{\Delta n}(n_{corr})$ of device C4 is two orders of magnitude higher than in case of C1-C3, and n_{corr} itself is almost one order of magnitude higher. This clearly shows that in cell C4 more than one additional effect plays a major role compared to the rest of set C. In any case it is plausible that increased light scattering could cause a higher charge carrier density *via* an enhanced light absorption. The higher lifetime is most likely a consequence of (i) more appropriate interfacial morphology or (ii) better bulk ordering of P3HT in between the low-density nanorods as a consequence of the considerably different relative donor/acceptor volume in favor of the P3HT.[175] Regardless of which is the cause of the higher lifetime, the observations suggest that the increased performance of device C4 is a combined effect, where probably *n* is increased by enhanced light scattering, possibly inducing higher hole mobility this way,[222] and $\tau_{\Delta n}$ is increased through more beneficial P3HT morphology.

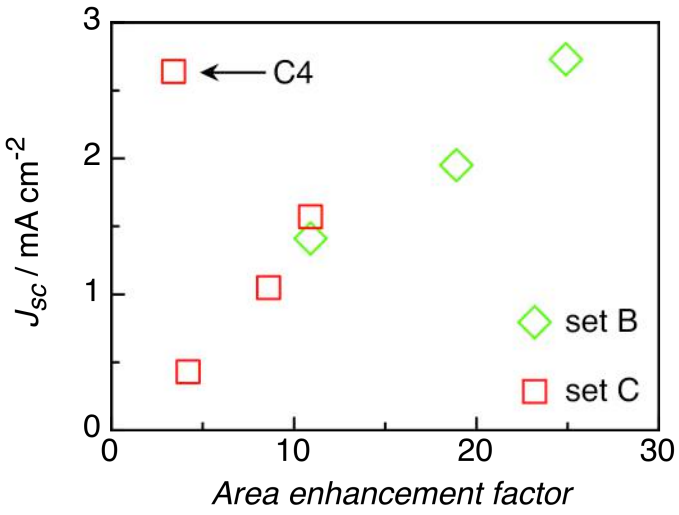

Figure 6.7. Relation between the area enhancement factor and short circuit current for devices from set B and set C. Device C4 is indicated, and does not fall within the same regime as the other devices.

6.3. Conclusion

In summary, hybrid solar cells based on P3HT-filled nanorod arrays of ZnO are prepared, hereby varying appropriate synthesis parameters to allow for systematic investigation of the morphology dependence of recombination kinetics. Interfacial P3HT morphology, induced by varying the melting time during device fabrication, appears to slightly reduce charge carrier lifetime and density, supporting our findings from previous work. More randomly oriented low-density nanorods are found to cause a divergence of the general behavior, exhibiting significantly higher charge carrier densities and lifetimes, suggesting that improved light scattering and more appropriate P3HT morphology, respectively, are the cause for the superior performance in the devices, despite the reduced donor-acceptor area. Taking advantage of the tunability of the interfacial area (by varying nanorod length and diameter) it is shown (by normalizing for effective interfacial area) that the recombination behavior of cells with different morphology is often identical, which suggests that differences in recombination observed for organic blends could in many cases also simply be the consequence of unequal heterojunction interface. This is consequential in the understanding of both types of solar cells, envisioning further improvements. Finally, this work shows that, by virtue of their more controlled morphology and interfacial area, template-based nanostructured hybrid solar cells can act as convenient means to investigate otherwise difficultly accessible in-depth working principles, thereby enabling to provide useful insights toward their fully organic analog.

6.4. Materials and methods

Synthesis of ZnO nanorod arrays. A seed layer was deposited by spincoating an aqueous Zn(II)-precursor on patterned ITO (15 Ω/sq, Every Rich Enterprise Limited), followed by thermal treatment on a hot plate at 300 °C and 500 °C for 1 minute and 5 minutes, respectively. A subsequent annealing step at 550 °C was done in a tube furnace for 1 hour in dry air. Next, the samples were transferred to an equimolar solution of zinc acetate (Sigma Aldrich) and hexamethylenetetramine (Sigma Aldrich) in deionized water and held at 95 °C for hydrothermal growth of the nanorods. The

growth time was varied to obtain the desired nanorod length, and the concentration of the hydrothermal growth solution was varied to adjust the average nanorod diameter and spacing. After the growth process, the samples were rinsed with deionized water and dried at 60 °C for 1 hour. Further details can be found elsewhere.[185]

Photovoltaic devices. The freshly prepared ZnO nanorod array-coated ITO substrates were heated at 150 °C for 20 minutes in air and cooled down with N_2 flow prior to spincoating P3HT (Rieke Metals) solutions in chlorobenzene (Aldrich).[87] After deposition, the samples were annealed at the melting temperature of P3HT (225 °C) in N_2. The annealing time was varied as required for each individual cell. Finally, 80 nm Ag top electrodes were evaporated in vacuum ($1 \cdot 10^{-6}$ mbar).

Image analysis. Scanning Electron Micrographs (SEM) of the ZnO arrays were obtained with a FEI Quanta 200FEG-SEM. To estimate the area enhancement factor from the SEM images, the open-source image processing software package ImageJ (version 1.45s) was used.

Solar cell characterization. JV-characterization was performed in air at room temperature using a Keithly 2400 SourceMeter under AM1.5 illumination of 100 mW/cm² with a Newport Oriel Class A model 91195A solar simulator. Impedance spectra (100 Hz - 5 MHz) were acquired using a HP 4194A Impedance/gain-phase analyzer, with an oscillating voltage of 25 mV, while illuminating with a 40W white LED with varying intensity. Impedance spectra were analyzed with ZSimpWin software (version 3.1, Princeton Applied Research), allowing to extract relevant parameters for recombination by fitting the spectra to a previously derived equivalent circuit.[136] Charge density values were obtained by differential capacitance technique.[195]

Chapter 7

Impact of photoelectron current on the determination of energy level alignment at ZnO/P3HT interfaces - a photoemission study

B. Conings, H. Yin, M. D'Olieslaeger, J.V. Manca, H.-G. Boyen, **2012**, *in preparation.*

ABSTRACT

A pivotal element in the successful operation of a solar cell is the favorable position of its donor and acceptor's energy levels relative to each other. Perhaps the most used technique to investigate this is photoelectron spectroscopy. While most photoemission studies are performed with disregard of the interfacial morphology or crystallographic facets, in this work we use well-defined ZnO single crystals as a platform for the deposition of P3HT, in order to mimic the ZnO/P3HT interface as it is present in the corresponding ZnO nanorod array/P3HT solar cell. We scrutinize the determination of relevant electronic parameters by investigating the impact of sample current, and thereby reveal a pitfall in photoemission measurements of such materials. This leads to novel recommendations for future photoemission studies, which can prevent faulty conclusions regarding the relation between energy level alignment and device performance.

7.1. Introduction

Organic/inorganic (hybrid) solar cells currently attract tremendous interest as they can be considered as an appealing alternative to fully organic solar cells based on, e.g., P3HT:PCBM bulk heterojunctions.[122] Hybrid solar cells comprising P3HT and ZnO as donor/acceptor materials promise excellent photovoltaic performance because of ZnO's superior transport properties as well as the higher level of chemical and morphological stability of the resulting hybrid devices.[83, 107] Moreover, ZnO can easily be patterned into nanorod arrays, thereby offering a significantly increased interfacial area between the different materials.[82, 84, 223] Consequently, a higher flux of charge carriers and, subsequently, a highly efficient charge transport towards the electrode can be expected after photoabsorption in the polymer.

Surprisingly, efficiencies of state-of-the-art devices are still in their infancy with efficiencies up to around 0.8 % for ZnO nanorod array/P3HT solar cells[86, 132, 185], and 2% for a ZnO/P3HT blend.[69] While interface morphology could be identified as one of the crucial factors giving rise to this rather limited performance,[89, 136] the role of energy level alignment at the donor/acceptor interface still remains unclear. Here, we report on an experimental study of the electronic structure at the P3HT/ZnO interface by means of photoelectron spectroscopy, intended to shed more light onto the coupling/alignment of electronic states between the two different materials.

In a hybrid solar cell, the exposed crystallographic facet of ZnO is a crucial factor for efficient charge generation at the ZnO/polymer interface.[136] ZnO nanorods usually grow in the thermodynamically favorable c-axis direction (in wurtzite crystal structure) with the (1,0,-1,0) surface forming the active interface.[129] Therefore, (1,0,-1,0)-oriented single crystals are exploited as substrates for the subsequent deposition of ultra-thin P3HT layers. This contrasts to previous work where (non-epitaxial) sputter-deposited films[224] or nanoparticle films[225] were used for similar studies, with the surface morphology remaining unclear. In our case, atomically flat terraces extending over macroscopic areas can be achieved by annealing single crystals at elevated temperature (1100°C) within a ZnO box kept under oxygen flow, following a method adapted from Ruther et al..[226] Thus, well-defined

surfaces/interfaces are available, providing a reliable platform for the determination of the electronic structure and related parameters.

7.2. Experimental section

7.2.1. Ultraviolet Photoelectron Spectroscopy (UPS)

In UPS, a sample kept in ultra-high vacuum is irradiated with UV photons typically generated by a noble gas discharge lamp (e.g., He-I with hν = 21.2 eV). The incident light excites electrons from occupied into unoccupied states, and those with a kinetic energy above the vacuum level of the sample (E_{vac}(s)) can reach and pass the surface without further scattering with other electrons (denoted “primary electrons”) provided their excitation took place within the information depth of the technique (few nm). A hemi-spherical energy analyzer (“detector”) then measures their residual kinetic energy thereby allowing to map the distribution of occupied electronic states and, thus, the electronic structure of the sample within the probed volume. Figure 7.1 illustrates the basic principle of electron spectroscopy and its application to determine the electronic structure of, e.g., a semiconductor. Electrons in the highest occupied states (i.e. at E_F in case of a metal, or below E_F for a semiconductor) escape from the sample with the highest measurable kinetic energy, E_K(max). On the other hand, the minimal measured energy, E_K(min), results from electrons which, upon photoexcitation, are left with only just sufficient energy to escape from the solid (primary electrons), or from electrons which have been excited deeper inside the sample and which have lost energy via scattering on their way to the sample surface, designated "secondary electrons".

Since there is electrical contact between the sample and the energy analyzer/detector, the Fermi level E_F (which defines the zero point of the binding energy scale) is constant throughout the system. As follows from Figure 7.1, E_K(min) can be used to extract the work function Φ_s of a sample from an experimental UPS spectrum once the work function Φ_d of the energy analyzer has been determined (typically by detecting the Fermi level cut-off measured on a gold or silver reference sample) :

$\Phi_s = \Phi_d + E_K(min)$ (7.1)

In a semiconductor the highest occupied states are situated well below E_F. The resulting energetic difference between those states and E_F defines the valence band maximum (VBM) (or the highest occupied molecular orbital (HOMO) in case of a polymer). From a corresponding UPS spectrum, the VBM or HOMO level can be determined by making use of the high kinetic energy cut-off $E_K(co)$ in the spectrum:

$E_K(max) - E_K(co) = E_F - VBM$ (7.2)

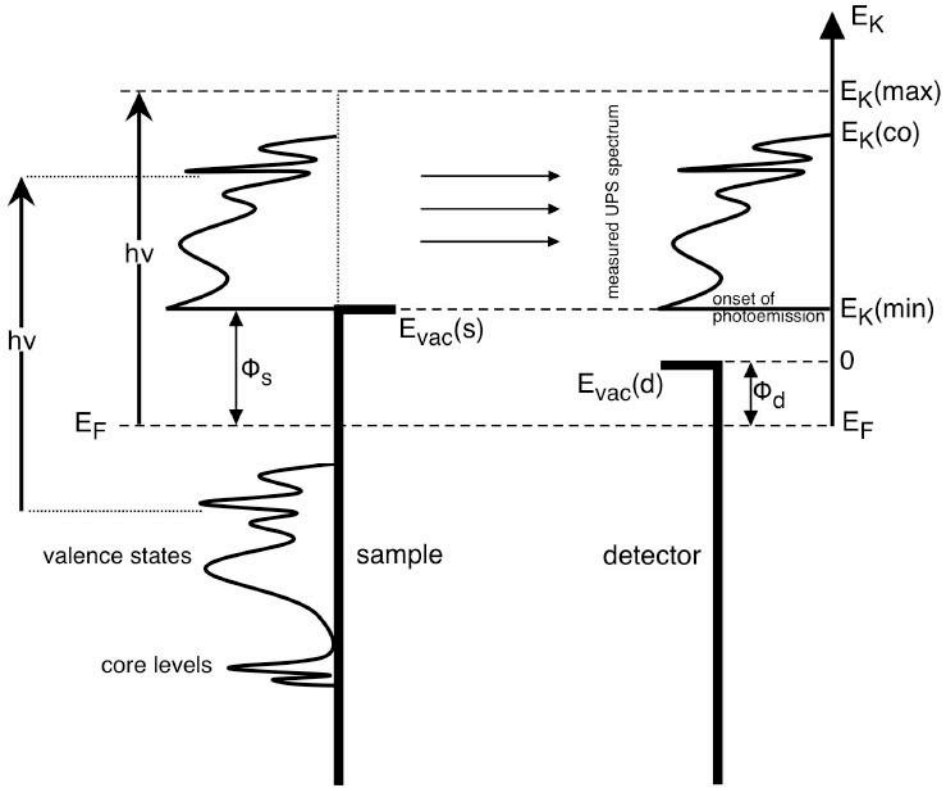

Figure 7.1. Photoemission process and UPS spectrum of a semiconductor. (Adapted from [227])

7.2.2. Sample preparation

ZnO single crystals with (1,0,-1,0)-orientation were purchased from MTI Corporation. Surface contaminants were removed from a single crystal by a short sonication in demineralized water, prior to transferring it to a ZnO box (Lesker) for a thermal

treatment at 1100 °C in a tube furnace for 2 hours under oxygen atmosphere in order to induce atomically flat terraces.[226] Subsequently, the sample was transferred to a commercial electron spectrometer (Physical Electronics 5600LS equipped with a monochromator X-ray source and a gas discharge lamp) with minimal exposure to ambient atmosphere (<10 sec) followed by a chemical analysis using X-ray photoelectron spectroscopy (XPS, photon energy 1486.6 eV) and the determination of the electronic structure by means of UPS (photon energy 21.2 eV). In a second step, a dilute solution of P3HT (Rieke) was spincoated on the single crystal in a nitrogen-filled glovebox, targeting a thickness of few nm, followed by XPS and UPS measurements after minimal delay. To mimic the processing conditions of ZnO/P3HT solar cells, in a third step, the sample was heated for 1 minute at 225°C in N_2 and transferred back to the electron spectrometer for its final analysis.

7.3. Results and discussion

A band diagram for the ZnO/P3HT bilayer system comprising the valence band/ conduction band edges of ZnO as well as the HOMO/LUMO levels of P3HT has been proposed earlier based on photovoltaic parameters derived from appropriate solar cells.[88] In that work, changes in energy level alignment were speculated to result from interface dipoles and their response to different sample treatments. An accurate energy level diagram, however, requires in addition the precise knowledge of the related vacuum levels, which can be determined by measuring the work function/ionization potential before and after depositing the P3HT on top of the ZnO substrate. Pitfalls in measuring work functions using photoelectron spectroscopy have recently been highlighted by Helander et.al. who pointed out the importance of a proper sample alignment with respect to the energy analyzer.[228] Here, we will demonstrate another effect which is of crucial importance for a precise determination of electronic parameters and which has not been reported so far: an energy correction taking into account the finite (non-zero) current of photo- and secondary electrons leaving the sample surface as will be demonstrated in the following.

A UPS spectrum representing the top region of the valence band of a clean (1,0,-1,0)-ZnO single crystal is shown in Figure 7.2 (left side). In case of the red curve which has

been acquired with maximum photon flux of the discharge lamp in order to obtain a high signal-to-noise ratio (resulting in an emission current of 47 nA), a cutoff at about 3.4 eV below the Fermi level E_F can be recognized thus defining the valence band maximum (VBM) of the n-type semiconductor. Simultaneously, a secondary electron cutoff at 3.6 eV above E_F can be identified (Figure 7.2, right side) representing its vacuum level, thereby defining its work function (Φ). On the other hand, when minimizing the photon flux in order to drastically reduce the emission current (factor of 4), a significant spectral shift by about 0.15 eV can be detected without inducing additional spectral features (blue curves). After depositing a thin layer of P3HT (~2 nm) on top of the single crystal, the UPS spectrum reveals new spectral features arising from the semiconducting polymer (Figure 7.3). The cutoff below E_F now defines the highest occupied molecular orbital (HOMO) of the P3HT. Again, when changing the photon flux in order to tune the emission current, significant spectral shifts of the HOMO and the vacuum levels are detected which appear to be even more pronounced as compared to the case of the pristine ZnO (0.3 eV).

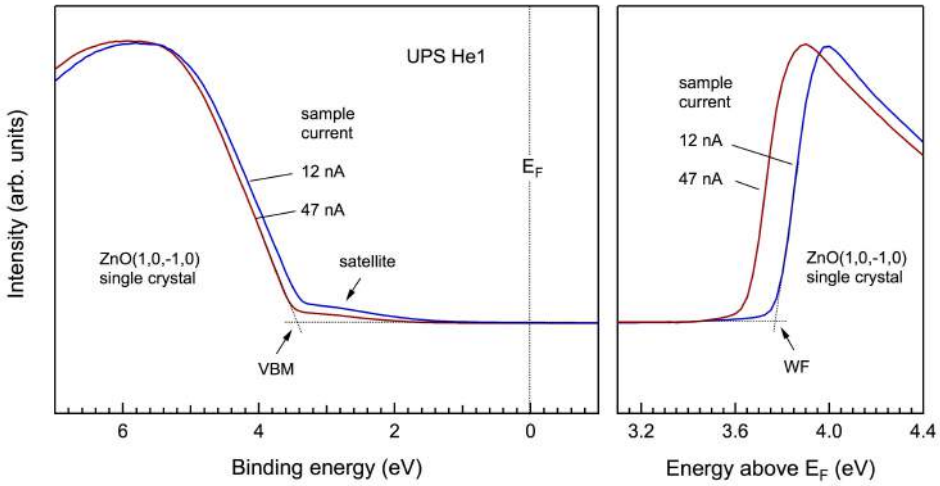

Figure 7.2. UPS spectrum of a (1,0,-1,0)-ZnO single crystal, for emission currents of 12 nA (blue) and 47 nA (red).

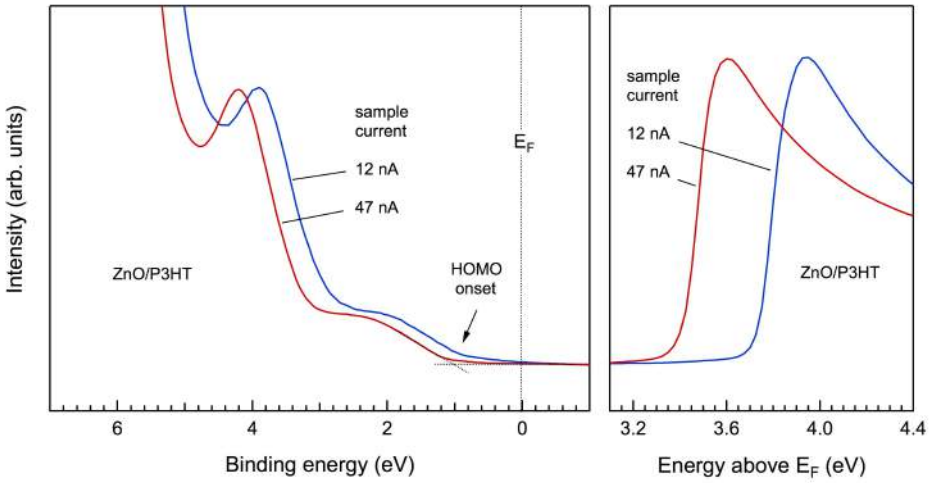

Figure 7.3. UPS spectrum of a (1,0,-1,0)-ZnO single crystal covered with a thin layer (~2 nm of P3HT), for emission currents of 12 nA (blue) and 47 nA (red).

To map this effect more in depth, the aforementioned electronic parameters are systematically evaluated as a function of sample current. First of all, Figure 7.4a presents the VBM of the pristine ZnO single crystal for a current ranging between 12 and 47 nA. At the highest (and generally considered most suited) photon flux the VBM is determined to be at 3.42 eV below E_F. However, a highly linear dependence on sample current is found, and an extrapolation to zero emission yields a energy value for the VBM of only 3.28 eV. Next, a similar experiment is performed after adding a very thin layer of P3HT to the single crystal yielding, this time, the HOMO level of the P3HT. Figure 7.4b shows again a strictly linear dependency on sample current with the highest value of the HOMO level at 1.05 eV below E_F obtained for maximum emission current and an extrapolated value of 0.66 eV below E_F for vanishing emission current, which is again a notable difference.

It was discovered before that a thermal treatment of the P3HT induces a vast performance improvement in a ZnO/P3HT solar cell, the proclaimed optimal treatment being 1 minute at the melting temperature of P3HT (225 °C).[132] It can assist in the infiltration of the P3HT into a porous structure or nanorod array, as well as enhance its crystallinity, thereby improving the short circuit current (J_{sc}), open-circuit voltage (V_{oc}) and fill factor of the resulting cell. To examine its impact onto the

interfacial electronic structure and ultimately striving to explain the resulting photovoltaic consequences, this thermal step in the fabrication of the corresponding solar cells was mimicked for the P3HT-covered single crystal. In Figure 7.4b, the data points for the annealed sample also show a linear behavior with respect to the emission current, yielding an extrapolation to zero sample current of 0.83 eV below E_F.

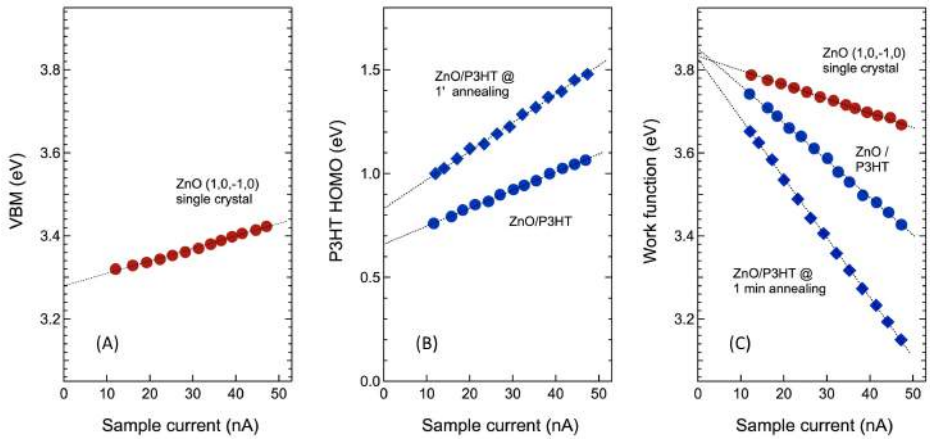

Figure 7.4. As a function of sample current, (a) the VBM of the ZnO single crystal, (b) the HOMO of pristine and annealed P3HT and (c) the work function of each of them.

To provide a complete picture of the interfacial electronic structure, first another vital parameter is determined: the work function (Φ). As was the case for the VBM of the single crystal, also the measured value of Φ appears to be dependent on the induced sample current (see Figure 7.4c). The same holds when the single crystal is coated with a thin layer of P3HT, both in the pristine and annealed case. The slope of the linear relations changes upon polymer addition and again upon thermal treatment, such that extrapolation of all data yields the same value of Φ at zero sample current (Φ = -3.82 eV). This is a remarkable result because it indicates that there is no chemical interaction taking place between the two materials. The vacuum levels are identical for all cases, hence the presence of an interface dipole can be ruled out. This is in clear contrast with the conclusions drawn from ZnO/P3HT bilayers[88] as well as with a previous report on this material system where ZnO nanoparticles were used rather than single crystals.[229] These results highlight the importance of a properly

defined surface as well as of a systematic evaluation of spectra for different emission currents in order to reliably evaluate the electronic structure of such kind of samples. The linear behavior of the electronic parameters versus sample current can be interpreted as an expression of Ohm's law. In case of (highly conductive) metallic samples, the emission current will not have much impact on the electronic structure determination, whereas for less conductive samples such as metal oxides and organic materials, a non-zero slope is expected resulting in current-induced shifts of the surface potential (equivalent to a voltage drop) and, thus, of the kinetic energy of the escaping photo- and secondary electrons.

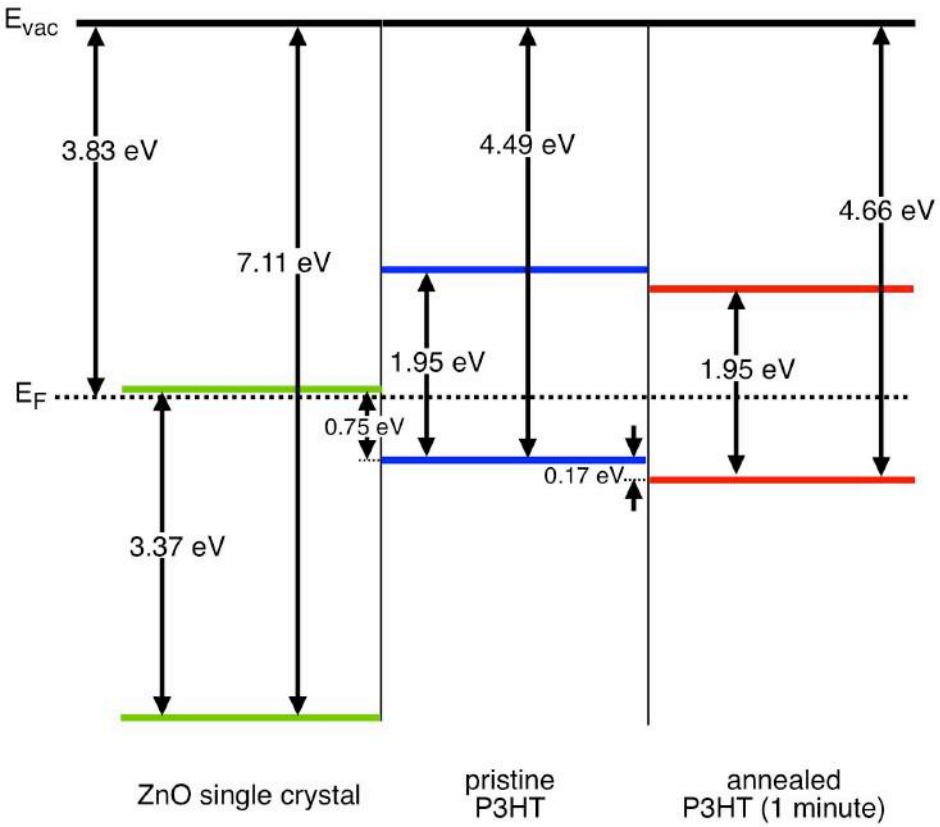

Figure 7.5. Energy level diagram of ZnO, pristine P3HT and annealed P3HT (1 minute), based on UPS measurements where the relevant parameters are extrapolated towards zero sample current.

Summarizing all obtained parameters, an accurate energy level diagram of the ZnO/P3HT interface can be assembled, as shown in Figure 7.5. The conduction band of ZnO and the LUMO of P3HT are calculated by adding the optical gap to the respective VB and HOMO level. HOMO and LUMO levels for both the unannealed and the annealed case are included in the diagram. The offset between the conduction band of ZnO (electron acceptor) and the HOMO level of the P3HT (electron donor) is related to the V_{oc} of the resulting solar cells.[29] When comparing pristine and annealed P3HT on ZnO, the difference in this offset is 0.17 eV, a value that corresponds very well to the difference in V_{oc} of the corresponding solar cells,[132] suggesting that a shift in the HOMO/LUMO-levels of the interfacial P3HT might be solely responsible for the improved V_{oc} in such devices. Note that this is under the assumption that the same energy offset is required for charge separation in both cases, which would be between 0.2 and 0.3 eV, corresponding well with previous reports.[230]

7.4. Conclusion

Our analysis demonstrates that an unambiguous determination of electronic structure parameters can only be achieved by measuring photoemission spectra for a range of sample currents, determining the desired parameters for each current, followed by an extrapolation to zero current that will provide the actual correct parameter values. This is an important observation that leads to the recommendation that electronic structure determinations should always be carried out as such, in order to deliver a sound and undebatable picture. Obviously, the zero current situation coincides with the V_{oc} in the current-voltage characteristic of the corresponding solar cell, and a correct comparison between different energy level diagrams corresponding to photovoltaic material combinations can thus only be made for this steady-state condition.

Chapter 8

Summary and outlook

ABSTRACT

Chapter 8 gives a concise recapitulation of the results described in this PhD work. Based on the main conclusions and on the current general status in the field of hybrid photovoltaics, several suggestions are made to prompt further progress.

8.1. Summary

Template-based hybrid solar cells pose a valid alternative to their fully organic counterparts by virtue of their morphological rigidity (*ergo* stability), as well as their more controllable morphology. Convenient implementation of elongated continuous carrier pathways, like nanorod arrays, in such solar cells clears the road to their further optimization. This thesis focuses on the preparation and characterization of hybrid solar cells based on ZnO nanorod arrays, infiltrated with P3HT, a widely investigated and well-documented workhorse polymer used in fully organic solar cells. Since the efficiency of these hybrids is still falling behind on the fully organic cells, a vast optimization is necessary for the former to have any prospect of competing with the latter. A step in this direction is provided by tuning fundamental morphological properties, leading to a significant improvement compared to literature values. First of all, the nanorod length is varied to find the best compromise between light absorption and charge transport, resulting in an optimum of 600 nm (nanorod diameter of 70 nm was constant throughout these experiments). This value significantly exceeds expectations based on the absorption capability of P3HT (which is sufficient to absorb nearly 100 % of the light in a layer of about 200 nm), yet it makes sense as the nanorods are transparent for most of the solar spectrum and act as a waveguide to transport light deeper into the cell. A second part of the optimization entails tuning the thicknesses of HBL and EBL, resulting in optima of 20 nm and 250 nm, respectively. As abundant presence of donor/acceptor interfaces is a pivotal requirement for successful solar cell operation, an elementary necessity for optimization is to achieve full infiltration of the polymer into the nanorod array, in most cases by providing a thermal treatment. This issue is often a concern, and is usually investigated solely by imaging (SEM or TEM), which is inadequate for unambiguous evaluation. To shed light onto this matter, a compositional depth profile of solar cells with different thermal history is made by XPS, allowing to determine the most beneficial treatment towards performance. Making a juxtaposition between a pristine solar cell and a treated one proves to be challenging, as the sputtering rate of P3HT is dependent on its degree of crystallinity, which in turn depends on thermal history. It was conclusively demonstrated, however, that full infiltration (into a

nanorod array of 600 nm) occurs after 1 minute of annealing at 225 °C, leading to an efficiency of 0.76%. Longer treatments appear to be not only redundant for infiltration, but even detrimental for device performance, despite that no differences can be found in infiltration, crystallinity or chemical integrity. The reason for the reduced performance in those cases is attributed to the local P3HT morphology near the interface with ZnO.

Pursuing a validation of this supposition, impedance spectroscopy is explored as characterization technique. In order to access specifically the interfacial properties, in the first place an equivalent circuit model has to be deduced, allowing to correctly interpret the impedimetric data. Eventually, the resistor/capacitor equivalent of the ZnO/P3HT interface follows the trend of device performance upon annealing, evidencing that increasingly detrimental interfacial P3HT morphology is responsible for the reduced performance, as ZnO is not affected by the used annealing temperature. This effect is suspected to relate to a reported theoretical study, which shows that P3HT is inclined to direct itself with its backbone perpendicular to the crystallographic facet of the sideplane of a nanorod, thereby implying that proper charge transport in the desired (vertical) direction would be impeded in our nanorod array-based solar cells. We find support for this hypothesis by carrying out mobility measurements, showing that the mobility in the vertical direction is reduced for P3HT inside a nanorod array compared to pure P3HT or P3HT on top of a flat ZnO layer.

The derived impedimetric model is also utilized for a study of the recombination kinetics of ZnO/P3HT solar cells. Impedance spectra are acquired under open-circuit (steady-state) conditions (i.e. no net current) for a number of light intensities, gaining access to the density and lifetime of charge carriers. A model for organic solar cells is adopted that allows to predict the V_{oc}, based on a number of recombination parameters obtained from the V_{oc}-dependence of charge carrier density and lifetime. The prediction of V_{oc} appears to work equally well for ZnO/P3HT hybrids, successfully demonstrating the broader validity of the model, and leading to the conclusion that hybrid and organic solar cells exhibit very similar recombination characteristics. This opens the door for the application of template-based hybrid solar cells to investigate device physics, by conducting experiments that rely on careful control over

morphology. A first step to put this into practice is taken by exploiting the tunable morphology of ZnO nanorod arrays by preparing different sets of devices that each vary in one specific morphological aspect. Varying the nanorod length from 300 nm to 600 nm has no influence on charge carrier density and lifetime, which indicates that charge transport properties are unchanged within this length range. For a fixed nanorod length, variations in diameter and spacing at first glance seem to induce large differences in recombination behavior. However, when expressing the charge carrier density as a function of effective interfacial area (estimated from SEM images), the apparent dissimilarity is cancelled out, proving the high extent of equivalence between those cells. An exception to this observation is the device with randomly oriented nanorods with very low density. Judging by its higher carrier lifetime and density, its disproportionately high performance (0.82%) compared to the other devices (certainly when considering its low donor/acceptor interface) is attributed to more beneficial P3HT morphology and increased light scattering.

It is shown that interface morphology has a major influence on device performance, but the role of energy level alignment at the ZnO/P3HT interface is not fully clear so far. Therefore, the electronic structure at this interface is determined by means of photoelectron spectroscopy, to elucidate the coupling/alignment of electronic states between the two materials. Since ZnO nanorods usually grow in the thermodynamically favorable c-axis direction (in wurtzite crystal structure) with the (1,0,-1,0) surface forming the active interface in hybrid solar cells, (1,0,-1,0)-oriented single crystals are exploited as substrates for the subsequent deposition of ultra-thin P3HT layers. This contrasts to previous work where (non-epitaxial) sputter-deposited ZnO films were used for similar studies with the surface morphology remaining unclear, and thus provides the most realistic image of the actual interface as present in the corresponding solar cell. We discover that the lower level of conduction of semiconductors, such as ZnO and P3HT, compared to metals, induces a non-negligible shift in their photoemission spectra for different photoelectron currents, thereby having a large influence on the determination of relevant electronic parameters. It is found that the unambiguous method of determination is to measure them for a range of sample currents, then extrapolating the values to zero current. Consequently, the

band diagram that con be constructed from such information is only valid at the V_{oc} of the corresponding solar cell.

To conclude, an answer can now be formulated to the three research questions posed in the beginning of this thesis (page 19). (i) As demonstrated, morphology plays a key role in device performance. The nanorod length, diameter and spacing predominantly influence the current produced by the solar cell due to varying donor/acceptor interface. Tilted nanorods appear to be successful, even with less heterojunction interface, which is attributed predominantly to improved light scattering. Annealing the polymer for 1 minute at its melting temperature of 225 °C allows to achieve full infiltration into the nanorod array and to improve the polymer's bulk crystallinity. (ii) A model, able to predict the V_{oc} of organic solar cells based on measured recombination parameters is found to be successful for our hybrid devices as well, substantiating the equivalence between organic and hybrid solar cells concerning device physics. Additionally, by benefiting from the tunable morphology of the nanorod arrays, and quantifying the interface with P3HT, it is demonstrated that the underlying recombination behavior of devices with varying nanorod length, diameter and spacing is identical, given that the thermal treatment is unchanged. This gives confidence that also for organic solar cells, where morphological quantification is more difficult, varying extents of recombination could likewise originate from a varying heterojunction area. (iii) Annealing the polymer for more than 1 minute appears to be detrimental for device performance, an effect that is attributable to its interfacial morphology near the ZnO nanorods. It is however possible to manipulate this interface by treating the ZnO with suitable adsorbed molecules, prior to polymer deposition. Furthermore, it is found that the actual energy level alignment at the ZnO/P3HT interface, as measured following a newly developed methodology in photoelectron spectroscopy, correlates well with the resulting V_{oc} of the corresponding solar cells.

8.2. Outlook and future work

Since the three main aspects that govern the device performance of the solar cells presented in this work are (i) the ZnO nanorods, (ii) the polymer and (iii) the interface between them, recommendations for research towards further improvements is subdivided following exactly these aspects.

8.2.1. Nanorod arrays

As already demonstrated in the PhD of Linny Baeten, and mentioned in this work, to attain tight control over nanorod morphology by hydrothermal growth from a seed layer is an arduous task. Targeting a specific set of structural properties more often than not requires an elaborate and labyrinthine optimization, as it is hard to map the interplay between different synthesis parameters. Consequently, it makes sense to resort to nanolithography techniques that allow to deposit discrete seeds of material in a controlled, rather than statistical fashion, prior to growing the nanorods. A possible strategy to control nanorod spacing and diameter is nanosphere lithography, where spheres of (mostly) polystyrene (PS) are deposited in a self-assembled monolayer (SAM) to act as a sacrificial mask for the deposition of ZnO (or metallic zinc that is oxidized afterwards by a thermal treatment), the interstitials between the spheres providing a hexagonally ordered plane of ZnO seeds once the PS template is removed. Figure 8.1 schematically explains the different steps of this process. Figure 8.2 shows an example of a SAM of PS spheres, deposited in this case via dipcoating, however, other techniques such as spincoating or Langmuir-Blodgett could also be viable options. In Figure 8.2 the spheres are quite polydisperse, but obviously monodisperse spheres work better for the purpose at hand.
A PS SAM-coated substrate can then be placed into the vacuum system depicted in Figure 8.3, which was built during this PhD work, for evaporation of zinc. Afterwards, the SAM is removed and the substrate is thermally treated to fully oxidize the metallic Zn islands into ZnO seeds, suited for nanorod growth. As an illustration, Figure 8.4a and b represent a calculation of the relation between the desired seed diameter, the PS sphere radius, the thickness of evaporated Zn and the distance

between the seeds. Note that this is a theoretical picture, limited by fact that the thickness of evaporated Zn must be smaller than the sphere diameter to ensure successful lift-off.

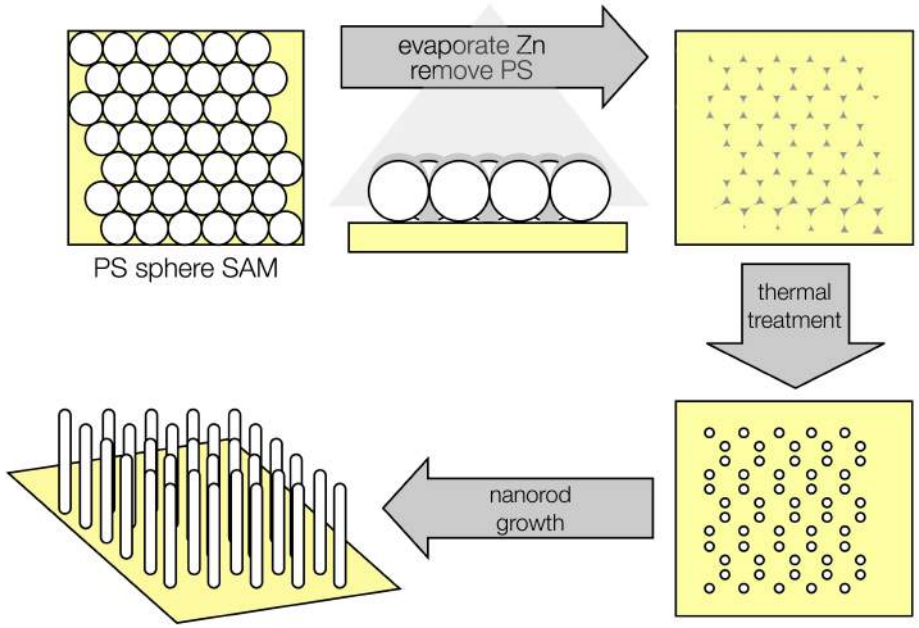

Figure 8.1. Schematic overview for the growth of ZnO nanorod arrays starting from seed arrays fabricated with nanosphere lithography.

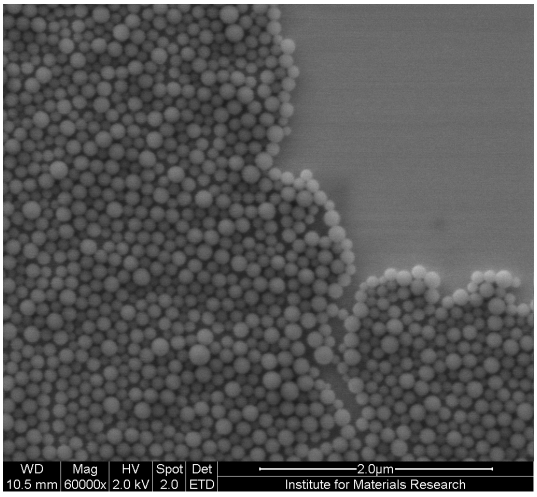

Figure 8.2. Self-assembled monolayer of polystyrene spheres.

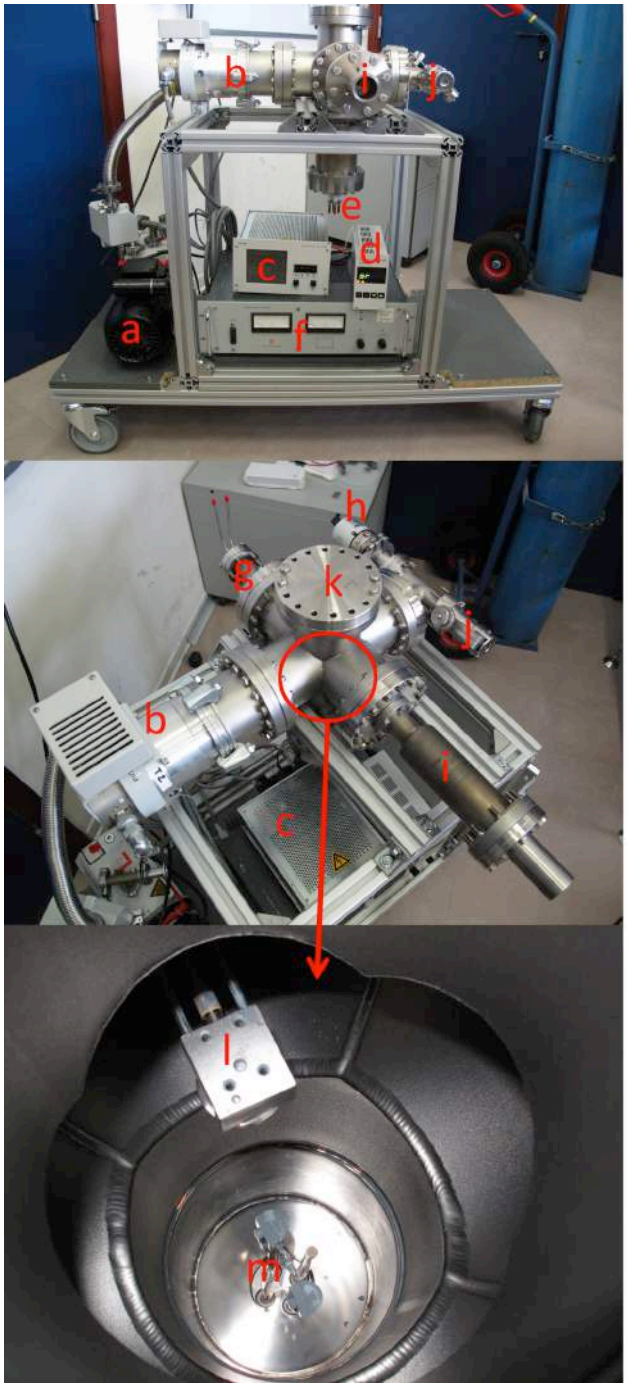

a. rotary pump
b. turbo pump
c. turbo pump controller
d. pressure gauge read-out
e. evaporation electrodes
f. power supply
g. QCM gauge outlet
h. pressure gauge
i. electrode for DC-plasma
j. gas flow control
k. closing flange/sample holder
l. QCM gauge
m. evaporation crucible

Figure 8.3. Vacuum system for evaporation of Zn, with description of important parts. The system also contains a possibility to create a DC oxygen plasma.

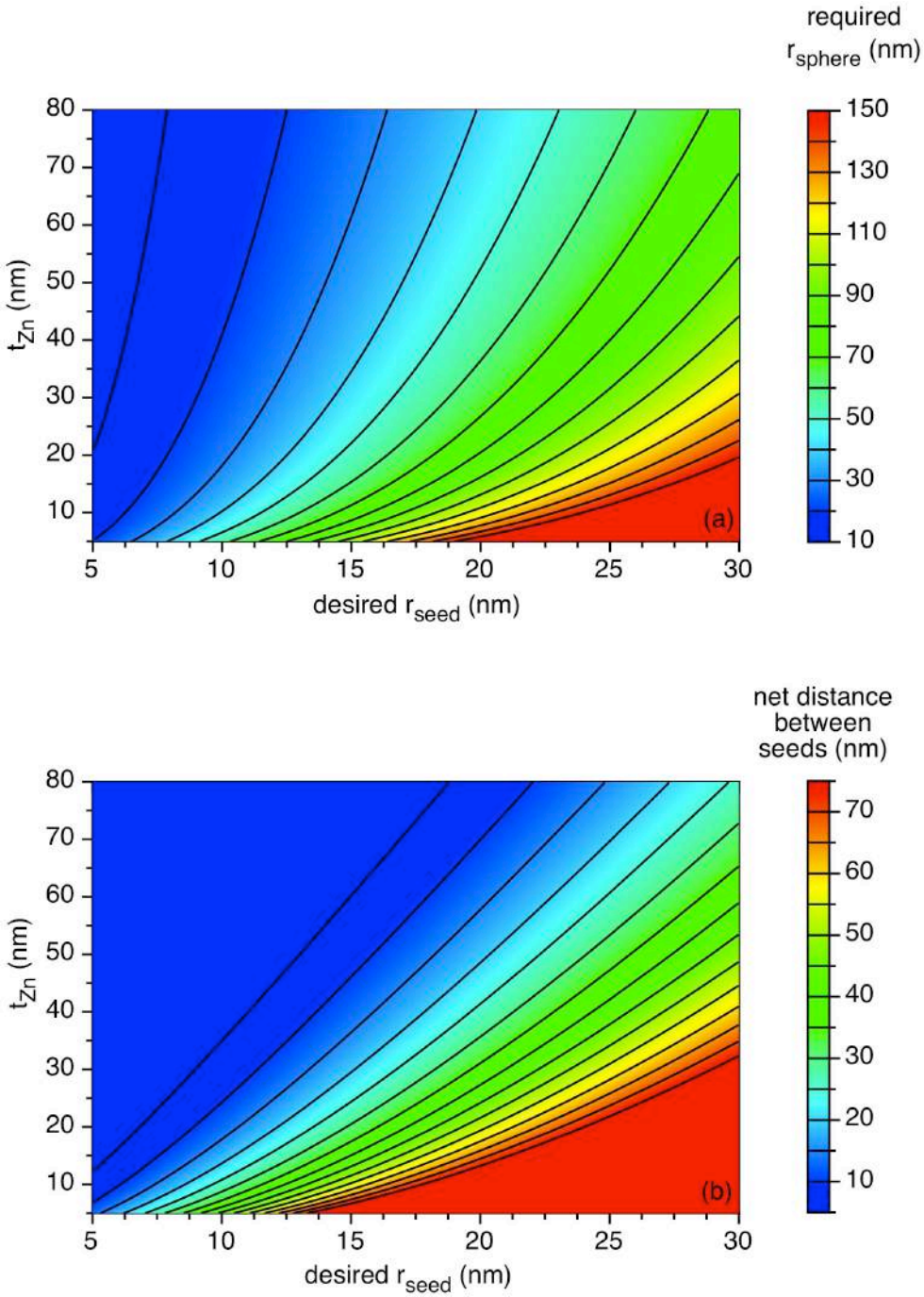

Figure 8.4. (a) Representation of the required PS sphere radius as a function of the desired ZnO seed diameter. (b) Resulting net distance between the seeds, given the values of (a).

The possibility to synthesize aligned nanorod arrays hydrothermally suggests that the growth of such structure has an epitaxial nature. XRD results indeed confirm that the presence of only one crystallographic direction is present in a hydrothermally grown ZnO nanorod array (c-axis), and this property is often considered as one of the main assets of semiconductor arrays in general because of the resulting improved charge carrier mobility. Caution has to be taken, however, as a purely XRD-based evaluation of the crystallographic quality inherently disguises the influence of local defects, which can (wrongfully) lead to the idea of high quality structures while the reality is inferior to this perfect picture. Figure 8.5 illustrates this statement by comparing cathodoluminescence (CL) measurements of a hydrothermally grown nanorod array with a single crystal. The peaks at 3.3-3.4 eV represent the bandgap energy of ZnO. The large sharp peak belonging to the single crystal indicates a high degree of order, while the very broad spread on the peak corresponding to the nanorod array proves that they contain a lot of structural defects, and also that the bandgap energy in the nanorod array is not well-defined. Obviously, this intrinsic property of hydrothermally grown nanorods has an impact on charge transport properties and consequently on device performance. Nanorods synthesized *via* an actual epitaxial growth technique, as in case of vapor-liquid-solid (VLS), could therefore present a more appropriate alternative for the hydrothermal ones, concerning device performance.

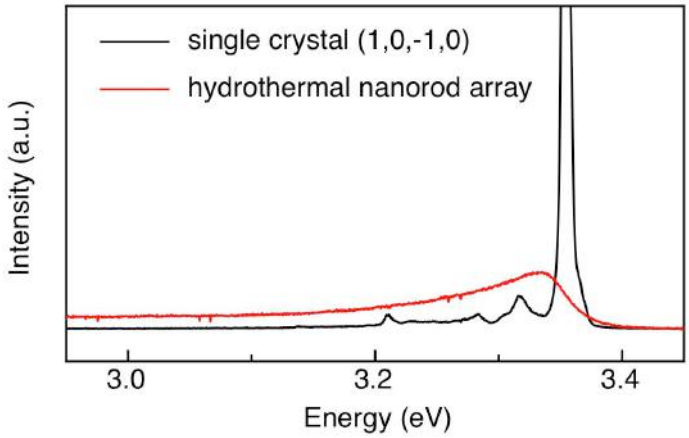

Figure 8.5. Cathodoluminescence spectra of a single crystal of ZnO with (1,0,-1,0)-orientation and a hydrothermally grown ZnO nanorod array.

8.2.2. Polymer

In this work P3HT is used as light-absorbing donor polymer, on account of its status as bestseller in organic photovoltaics, and allowing for more meaningful comparison with our hybrid solar cells. Lately, low bandgap polymers (able to absorb a larger portion of the solar spectrum), such as PCPDTBT, have been gaining ground in the field of organic photovoltaics, so their introduction into hybrid devices is inevitable. Blends of such polymers with PCBM deliver the best performance when processed in a very thin active layer (< 80 nm), as a consequence of their relatively low hole mobility, resulting from their amorphous nature. This could present a problem in hybrid solar cells in their current form, as these typically use considerably thicker active layers, with nanorod arrays that have to be infiltrated all the way to the top. In that sense it would be more appropriate (for low bandgap polymers, but also for P3HT) to create a nanorod array with smaller dimensions (diameter, length and spacing), providing facile infiltration in between short charge carrier pathways whilst still having sufficient donor/acceptor area. Approaching the problem from a different angle, regular nanorods (as used in this work) could also be covered with a thin layer of polymer (in the order of the exciton diffusion length), this way coating the nanorods rather than filling the entire space between them. On the other hand, this strategy can lead to problems with the deposition of the metallic electrode due to the undulated morphology of the polymer-coated nanorod array, and does not leave much room for an EBL. The same holds when the polymer would be replaced by small molecules.

A more fundamental statement that could be given is that polymers exhibiting a more favorable energy level alignment with ZnO than P3HT could definitely result in a performance increase by virtue of an improved V_{oc} and/or more efficient exciton dissociation.

8.2.3. ZnO/polymer interface

It has is shown in this thesis and in literature that interfacial properties have a major influence on device performance of hybrid solar cells. The sensitivity for interface-related phenomena can be turned into an advantage by decorating the interface with

appropriate molecules, allowing to tune donor-acceptor energy level alignment and charge transfer in favor of device performance. A range of organic molecules has been proposed in literature to serve this purpose, but the true mechanisms still remain unclear, which might be part of the reason why interface functionalization is predominantly successful so far in bilayer devices and not so much in nanostructured ones. It may also be illustrative for the fact that the exposed crystallographic facet has crucial impact on the way these molecules attach, the surface coverage, and consequently the way they influence the local morphology of the polymer. In any case, this investigation route is worth looking into, as preliminary results from our lab suggest that the functionalization of ZnO nanorods with the organic molecule 4-tert-butylpyridine is beneficial for device performance (see Figure 8.6a). The increased time constant obtained from the RC-combination related to the ZnO/P3HT interface could point to more beneficial P3HT morphology as a result of the functionalization (Figure 8.6b). In order to obtain fundamental insight into the effects of surface modification, photoelectron spectroscopy would then enable to identify the key parameters determining the efficiency in such devices and, thus, help to push their performance to significantly higher values.

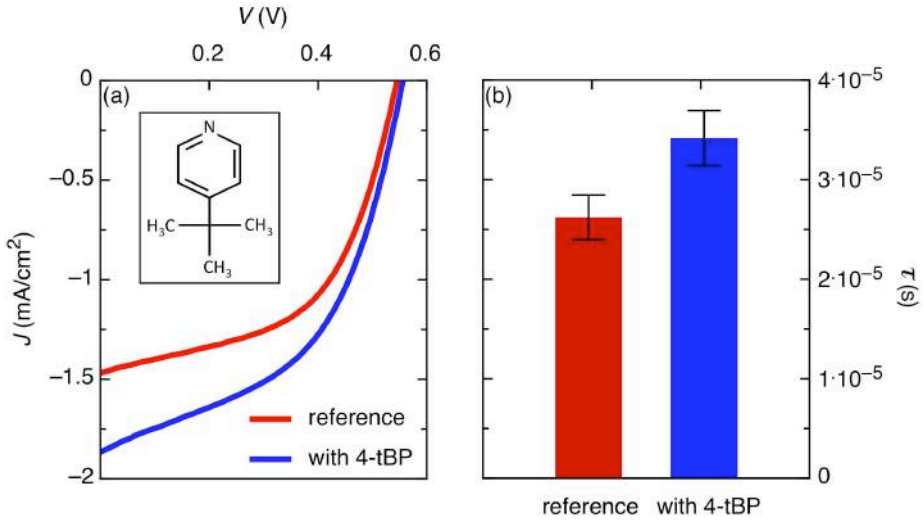

Figure 8.6. (a) JV-curve of a ZnO nanorod array/P3HT solar cell, where the nanorod array is functionalized with 4-tert-butylpyridine (4-tBP), compared to an unmodified reference device. The inset shows the chemical structure of 4-tBP. (b) Time constant related to the ZnO/(4-tBP)/P3HT.

8.3. Nederlandse samenvatting

Sjabloongebaseerde hybride zonnecellen bieden een valabel alternatief voor hun volledig organische tegenhangers op grond van morfologische rigiditeit (dus stabiliteit) en controleerbaardere morfologie. Eenvoudige implementatie van langwerpige continue ladingsdragerswegen (zoals arrays van nanostaafjes) in zulke zonnecellen maakt de weg vrij voor hun verdere optimalisatie. Deze thesis legt zich toe op de preparatie en karakterisatie van hybride zonnecellen gebaseerd op arrays van ZnO nanostaafjes, geïnfiltreerd met poly(3-hexylthiofeen) (P3HT), een breed onderzocht en goed gedocumenteerd referentiepolymeer dat veel in volledig organische zonnecellen wordt gebruikt. Aangezien de efficiëntie van deze hybride zonnecellen nog achterloopt op organische zonnecellen, is hun vermogen om te concurreren met deze laatsten afhankelijk van een extensieve optimalisatie. Er is een stap in deze richting gezet door het afstemmen van fundamentele morfologische eigenschappen, hetgeen leidt tot een significante verbetering ten opzichte van literatuurwaarden. Ten eerste wordt de lengte van de nanostaafjes gevarieerd om het beste compromis te vinden tussen lichtabsorptie en ladingstransport, resulterend in een optimum van 600 nm lengte (met een vaste diameter van 70 nm voor deze experimenten). Deze waarde overstijgt de verwachtingen als men de absorptiecapaciteit van P3HT in beschouwing neemt (200 nm polymeer is voldoende voor praktisch maximale absorptie), doch dit wordt verklaard doordat ZnO nanostaafjes transparant zijn voor het grootste deel van het zonnespectrum en dus het licht dieper in de zonnecel laten doordringen. Een tweede deel van de optimalisatie behelst het vinden van de juiste diktes voor de gatenblokkeringslaag en de elektronenblokkeringslaag, wat optima van respectievelijk 20 nm en 250 nm oplevert. Vermits een overvloedige aanwezigheid van donor/acceptor grensvlakken een hoofdvereiste is voor de succesvolle werking van de zonnecel, is het optimaliseren van polymeerinfiltratie (door thermische behandeling) een absolute noodzaak. Dit aspect is vaak een pijnpunt, en wordt meestal enkel onderzocht met behulp van beeldvormingstechnieken (SEM of TEM), wat onvoldoende is voor een adequate evaluatie. Om verduidelijking te verschaffen hieromtrent wordt er met XPS

een compositorisch diepteprofiel gemaakt van zonnecellen met verschillende thermische voorgeschiedenis, wat toelaat om de meest bevorderlijke behandeling te bepalen ten behoeve van de uiteindelijke celefficiëntie. Het blijkt echter moeilijk om een directe vergelijking te maken tussen een thermische onbehandelde en een behandelde zonnecel omdat de sputtercoëfficiënt van P3HT afhangt van de kristalliniteit, die op haar beurt weer afhangt van de thermische voorgeschiedenis. Desondanks is er onomstotelijk bewezen dat volledige infiltratie (in een array van nanostaafjes van 600 nm) optreedt na een thermische behandeling van 1 minuut bij 225 °C, wat resulteert in een efficiëntie van 0.76 %. Langere behandelingen blijken niet alleen onnodig voor infiltratie, maar zelfs schadelijk voor de efficiëntie, ondanks dat er geen verschillen kunnen worden gevonden voor zowel infiltratie, kristalliniteit en chemische samenstelling/stoëchiometrie. De reden voor de verminderde performantie in deze gevallen wordt toegeschreven aan de lokale morfologie van het P3HT bij het grensvlak met ZnO. Impedantiespectroscopie wordt voorgesteld als karakterisatietechniek om deze veronderstelling te verifiëren. Om specifiek toegang te krijgen tot de grensvlakeigenschappen, wordt eerst een equivalent circuit opgesteld dat toelaat om de impedimetrische resultaten correct te interpreteren. Uiteindelijk blijkt het weerstand/condensator equivalent van het ZnO/P3HT grensvlak de trend te volgen van de celperformantie als functie van thermische voorgeschiedenis. Dit toont aan dat de verslechterende grensvlakmorfologie van het P3HT verantwoordelijk is voor de verminderde performantie, aangezien ZnO niet beïnvloed wordt door de gebruikte temperatuur. Dit effect wordt gerelateerd aan een theoretische studie die laat zien dat P3HT geneigd is om zich te richten met de backbone van de keten loodrecht op het zijvlak van een nanostaafje, wat impliceert dat ladingstransport in de gewenste (dus verticale) richting gehinderd wordt in zonnecellen gebaseerd op arrays van nanostaafjes. Deze hypothese wordt ondersteund door mobiliteitsmetingen die aantonen dat de mobiliteit in de verticale richting lager is voor P3HT dat geïnfiltreerd is in een array van nanostaafjes, vergeleken met P3HT afgezet op een vlakke ZnO-laag.

Het afgeleide impedimetrische model wordt ook aangewend voor studie naar de recombinatiekinetiek van ZnO/P3HT zonnecellen. Impedantiespectra worden

opgenomen onder open-keten (V_{oc}, steady-state) conditie (geen netto stroom) voor een aantal lichtintensiteiten om toegang te verkrijgen tot de dichtheid en levensduur van de ladingsdragers. Een model dat opgesteld werd voor organische zonnecellen, gebaseerd op een aantal recombinatieparameters, verkregen door de V_{oc}-afhankelijkheid van de dichtheid en levensduur van de ladingsdragers, en in staat is om de open-keten spanning te voorspellen, wordt toegepast. De voorspelling van V_{oc} blijkt evengoed te werken voor hybride ZnO/P3HT zonnecellen, hetgeen met succes de bredere geldigheid van het model aantoont, en leidt tot de conclusie dat hybride en organische zonnecellen zeer gelijkaardige recombinatie-eigenschappen vertonen. Dit geeft aanleiding tot de toepassing van sjabloongebaseerde hybride zonnecellen om fysische principes te onderzoeken door experimenten uit te voeren die minutieuze morfologische controle vereisen. Een eerste stap om dit in de praktijk om te zetten wordt genomen door gebruik te maken van de controleerbare morfologie van arrays van ZnO nanostaafjes, door verschillende reeksen zonnecellen te maken die ieder variëren in een specifiek morfologisch aspect. De lengte van de nanostaafjes wijzigen van 300 nm tot 600 nm heeft geen invloed op dichtheid en levensduur van de ladingsdragers, wat impliceert dat hun transporteigenschappen onveranderd blijven in dit lengtebereik. In het geval van een vaste lengte van de nanostaafjes, lijken variaties in diameter en onderlinge afstand op het eerste zicht grote verschillen te induceren in het recombinatiegedrag. Echter, als de ladingsdragersdichtheid uitgedrukt wordt als functie van het effectieve grenslaagoppervlak tussen ZnO en P3HT (geschat van SEM-opnamen) wordt het schijnbare verschil tenietgedaan, wat de hoge graad van equivalentie tussen deze cellen benadrukt. Een uitzondering op deze observatie is de zonnecel met een lage dichtheid aan nanostaafjes, die willekeurig georiënteerd zijn. Afgaande op de hoge ladingsdragersdichtheid en -levensduur in dit geval, wordt de corresponderende disproportioneel hoge efficiëntie in vergelijking met de andere cellen (0.82 %) toegeschreven aan verhoogde lichtverstrooiing en gunstigere P3HT morfologie.

Er is aangetoond dat grensvlakmorfologie een grote invloed heeft op celperformantie, maar de rol van de uitlijning van energieniveaus aan het ZnO/P3HT grensvlak is voorts nog onvoldoende duidelijk. Daarom wordt de elektronische structuur aan dit

grensvlak bepaald door middel van fotoëlektron spectroscopie, om de koppeling/uitlijning van de elektronische toestanden tussen de twee materialen te verduidelijken. Aangezien ZnO nanostaafjes doorgaans groeien in de thermodynamisch gunstige c-as richting (in geval van de wurtziet kristalstructuur), waarbij het (1,0,-1,0)-vlak het actieve grensvlak vormt in hybride zonnecellen, worden (1,0,-1,0)-georiënteerde eenkristallen gebruikt als substraten voor de afzetting van een ultradunne laag P3HT. Dit is in contrast met eerder werk, waar niet-epitaxiale ZnO films (afgezet via sputtering) werden gebruikt voor gelijkaardige studies, waarbij er geen uitsluitsel was omtrent de morfologie van het oppervlak. Onze methode biedt dus het meest realistische beeld van het eigenlijke grensvlak zoals het aanwezig is in de zonnecel. We ontdekken dat de lagere geleidbaarheid van halfgeleiders, zoals ZnO en P3HT, in vergelijking met metalen, een niet-verwaarloosbare verschuiving induceert in hun fotoëlektron spectra, wat een grote weerslag heeft op de determinatie van relevante elektronische parameters. De ondubbelzinnige methode om deze te bepalen, is ze te meten voor een zeker bereik van substraatstromen en vervolgens een extrapolatie uit te voeren naar de situatie waarbij die stroom nul is. Als gevolg is het energieniveauschema dat uit deze informatie kan opgesteld worden enkel geldig bij de open-ketenspanning van de bijhorende zonnecel.

Ter conclusie kan een antwoord geformuleerd worden op de drie onderzoeksvragen die in het begin van deze thesis werden gesteld (pagina 19). (i) Zoals aangetoond, speelt morfologie een sleutelrol in de celefficiëntie. De lengte van de nanostaafjes, diameter en onderlinge afstand beïnvloeden voornamelijk de geproduceerde stroom als gevolg van een variërende oppervlakte van het donor/acceptor grensvlak. Licht gekantelde nanostaafjes blijken succesvol, zelfs met minder heterojunctie-oppervlak, wat hoofdzakelijk toegeschreven wordt aan verbeterde lichtverstrooiing. Een thermische behandeling van het polymeer van 1 minuut bij zijn smelttemperatuur van 225 °C zorgt voor volledige infiltratie en een verbeterde kristalliniteit van het bulk polymeer. (ii) Een model dat in staat is om de V_{oc} van organische zonnecellen te voorspellen op basis van gemeten recombinatieparameters blijkt even succesvol voor onze hybride zonnecellen, wat de equivalentie tussen organische en hybride zonnecellen wat betreft fysische werkingsprincipes benadrukt. Bovendien wordt er,

door gebruik te maken van de controleerbare morfologie van de nanostaafjes arrays, en door kwantificatie van het grensvlak met P3HT, aangetoond dat het onderliggende recombinatiegedrag van zonnecellen met nanostaafjes die variëren in lengte, diameter en onderlinge afstand, identiek is, gegeven dat de thermische behandeling ongewijzigd blijft. Dit ondersteunt het idee dat ook voor organische zonnecellen, waarbij morfologische kwantificatie minder evident is, variërende graden van recombinatie simpelweg een gevolg kunnen zijn van een variërend heterojunctie-oppervlak. (iii) Het polymeer langer dan 1 minuut thermisch behandelen blijkt nefast voor de celperformantie, een effect dat toe te schrijven is aan de morfologie bij het grensvlak met de ZnO nanostaafjes. Wel is het mogelijk de eigenschappen van dit grensvlak te wijzigen door een behandeling met geschikte geadsorbeerde moleculen, alvorens het polymeer af te zetten. Tot slot is er aangetoond dat, rekening houdende met een mogelijke valkuil bij metingen van fotoëlektron spectroscopie, de eigenlijke uitlijning van energieniveau's aan het ZnO/P3HT grensvlak goed correleert met de resulterende V_{oc} van de corresponderende zonnecellen.

References

[1] L. E. Doman, K. A. Smith, J. O'Sullivan, K. R. Vincent, J. L. Barden, P. D. Martin, A. Fawzi, M. L. Mellish, D. R. Kearney, B. T. Murphy, N. Slater-Thompson, P. Gross, V. V. Zaretskaya, G. Jacobs, (Eds: J. Conti, P. Holtberg), International Energy Outlook 2011, US Energy Information Administration, 2011.

[2] S. Teske, A. Zervos, O. Schäfer, *Energy [r]evolution, a sustainable OECD Europe Energy Outlook,* , EREC (European Renewable Energy Council), 2007.

[3] R. W. Miles, G. Zoppi, I. Forbes, *Mater. Today* **2007**, *10*, 20.

[4] W. Shockley, H. J. Queisser, *J. Appl. Phys.* **1960**, *32*, 510.

[5] N. Espinosa, M. Hosel, D. Angmo, F. C. Krebs, *Energy Environ. Sci.* **2012**, *5*, 5117.

[6] G. Li, R. Zhu, Y. Yang, *Nat. Photonics* **2012**, *6*, 153.

[7] G. Yu, K. Pakbaz, A. J. Heeger, *Appl. Phys. Lett.* **1994**, *64*, 3422.

[8] G. Yu, J. Gao, J. C. Hummelen, F. Wudl, A. J. Heeger, *Science* **1995**, *270*, 1789.

[9] R. Gaudiana, C. Brabec, *Nat. Photonics* **2008**, *2*, 287.

[10] F. C. Krebs, *Sol. Energy Mater. Sol. Cells* **2009**, *93*, 394.

[11] R. Søndergaard, M. Hösel, D. Angmo, T. T. Larsen-Olsen, F. C. Krebs, *Mater. Today* **2012**, *15*, 36.

[12] F. C. Krebs, *Org. Electron.* **2009**, *10*, 761.

[13] M. Manceau, D. Angmo, M. Jørgensen, F. C. Krebs, *Org. Electron.* **2011**, *12*, 566.

[14] http://www.heliatek.com, 2012.

[15] K. Vandewal, K. Tvingstedt, O. Inganäs, in *Semiconductors and Semimetals*, Vol. 85 (Eds: M. T. Uli Würfel, R. W. Eicke), Elsevier, 2011, 261.

[16] X. Yang, J. K. J. v. Duren, R. A. J. Janssen, M. A. J. Michels, J. Loos, *Macromolecules* **2004**, *37*, 2151.

[17] S. Bertho, G. Janssen, T. J. Cleij, B. Conings, W. Moons, A. Gadisa, J. D'Haen, E. Goovaerts, L. Lutsen, J. V. Manca, D. Vanderzande, *Sol. Energy Mater. Sol. Cells* **2008**, *92*, 753.

[18] A. J. Moulé, L. Chang, C. Thambidurai, R. Vidu, P. Stroeve, *J. Mater. Chem.* **2012**, *22*.

[19] J. W. Chen, Y. Cao, *Acc. Chem. Res.* **2009**, *42*, 1709.

[20] S. H. Park, A. Roy, S. Beaupre, S. Cho, N. Coates, J. S. Moon, D. Moses, M. Leclerc, K. Lee, A. J. Heeger, *Nat. Photonics* **2009**, *3*, 297.

[21] J. Gilot, M. M. Wienk, R. A. J. Janssen, *Adv. Mater.* **2010**, *22*, E67.

[22] P. E. Shaw, A. Ruseckas, I. D. W. Samuel, *Adv. Mater.* **2008**, *20*, 3516.

[23] D. E. Markov, E. Amsterdam, P. W. M. Blom, A. B. Sieval, J. C. Hummelen, *J. Phys. Chem. A* **2005**, *109*, 5266.

[24] T. J. Savenije, J. M. Warman, A. Goossens, *Chem. Phys. Lett.* **1998**, *287*, 148.

[25] A. Haugeneder, M. Neges, C. Kallinger, W. Spirkl, U. Lemmer, J. Feldmann, U. Scherf, E. Harth, A. Gügel, K. Müllen, *Phys. Rev. B* **1999**, *59*, 15346.

[26] H. Hoppe, N. S. Sariciftci, *Adv. Polym. Sci.* **2008**, *214*, 1.

[27] J. G. Muller, J. M. Lupton, J. Feldmann, U. Lemmer, M. C. Scharber, N. S. Sariciftci, C. J. Brabec, U. Scherf, *Phys. Rev. B* **2005**, *72*.

[28] C. Piliego, M. A. Loi, *J. Mater. Chem.* **2012**, *22*.

[29] C. Deibel, V. Dyakonov, *Rep. Prog. Phys.* **2010**, *73*, 096401.

[30] L. J. A. Koster, V. D. Mihailetchi, P. W. M. Blom, *Appl. Phys. Lett.* **2006**, *88*.
[31] C. G. Shuttle, B. O'Regan, A. M. Ballantyne, J. Nelson, D. D. C. Bradley, J. R. Durrant, *Phys. Rev. B* **2008**, *78*, 113201.
[32] J. D. Servaites, M. A. Ratner, T. J. Marks, *Energy Environ. Sci.* **2011**, *4*.
[33] L. J. A. Koster, E. C. P. Smits, V. D. Mihailetchi, P. W. M. Blom, *Phys. Rev. B* **2005**, *70*, 085205.
[34] K. Maturová, S. S. van Bavel, M. M. Wienk, R. A. J. Janssen, M. Kemerink, *Nano Lett.* **2009**, *9*, 3032.
[35] D. Cheyns, J. Poortmans, P. Heremans, C. Deibel, S. Verlaak, B. P. Rand, J. Genoe, *Phys. Rev. B* **2008**, *77*, 165332.
[36] C. G.A, *Solar Cells* **1983**, *8*, 47.
[37] S. Karg, W. Riess, M. Meier, *Synth. Met.* **1993**, *57*, 4186.
[38] C. W. Tang, *Appl. Phys. Lett.* **1986**, *48*, 183.
[39] C. R. McNeill, S. Westenhoff, C. Groves, R. H. Friend, N. C. Greenham, *J. Phys. Chem.* **2007**, *111*, 19153.
[40] M. Campoy-Quiles, T. Ferenczi, T. Agostinelli, P. G. Etchegoin, Y. Kim, T. D. Anthopoulos, P. N. Stavrinou, D. D. C. Bradley, J. Nelson, *Nat. Mater.* **2008**, *7*, 158.
[41] M. Pfannmöller, H. Flügge, G. Benner, I. Wacker, C. Sommer, M. Hanselmann, S. Schmale, H. Schmidt, F. A. Hamprecht, T. Rabe, W. Kowalsky, R. R. Schröder, *Nano Lett.* **2011**, *11*, 3099.
[42] M. A. Green, K. Emery, Y. Hishikawa, W. Warta, E. D. Dunlop, *Prog. Photovoltaics Res. Appl.* **2011**, *19*, 565.
[43] M. A. Green, K. Emery, Y. Hishikawa, W. Warta, E. D. Dunlop, *Prog. Photovoltaics Res. Appl.* **2012**, *20*, 12.
[44] Y. Sun, G. C. Welch, W. L. Leong, C. J. Takacs, G. C. Bazan, A. J. Heeger, *Nat. Mater.* **2011**, *11*, 44.
[45] L. Y. Park, A. M. Munro, D. S. Ginger, *J. Am. Chem. Soc.* **2008**, *130*, 15916.
[46] X. He, F. Gao, G. Tu, D. G. Hasko, S. Hüttner, N. C. Greenham, U. Steiner, R. H. Friend, W. T. S. Huck, *Adv. Funct. Mater.* **2011**, *21*, 139.
[47] Y. Yang, K. Mielczarek, M. Aryal, A. Zakhidov, W. Hu, *ACS Nano* **2012 DOI: 10.1021/nn3001388**.
[48] B. O'Regan, M. Grätzel, *Nature* **1991**, *353*, 737.
[49] A. Hagfeldt, G. Boschloo, L. Sun, L. Kloo, H. Pettersson, *Chem. Rev.* **2010**, *110*, 6595.
[50] A. Yella, H.-W. Lee, H. N. Tsao, C. Yi, A. K. Chandiran, M. K. Nazeeruddin, E. W.-G. Diau, C.-Y. Yeh, S. M. Zakeeruddin, M. Grätzel, *Science* **2011**, *334*, 629.
[51] H. J. Snaith, L. Schmidt-Mende, *Adv. Mater.* **2007**, *19*, 3187.
[52] H. J. Snaith, A. J. Moule, C. Klein, K. Meerholz, R. H. Friend, M. Gratzel, *Nano Lett.* **2007**, *7*, 3372.
[53] T. Leijtens, I. K. Ding, T. Giovenzana, J. T. Bloking, M. D. McGehee, A. Sellinger, *ACS Nano* **2012**, *6*, 1455.
[54] W. U. Huynh, J. J. Dittmer, A. P. Alivisatos, *Science* **2002**, *295*, 2425.
[55] Y. Zhou, Y. C. Li, H. Z. Zhong, J. H. Hou, Y. Q. Ding, C. H. Yang, Y. F. Li, *Nanotechnol.* **2006**, *17*, 4041.

[56] Z. Wang, S. Qu, X. Zeng, C. Zhang, M. Shi, F. Tan, Z. Wang, J. Liu, Y. Hou, F. Teng, Z. Feng, *Polymer* **2008**, *49*, 4647.
[57] D. H. Cui, J. Xu, T. Zhu, G. Paradee, S. Ashok, M. Gerhold, *Appl. Phys. Lett.* **2006**, *88*.
[58] A. M. Smith, S. Nie, *Acc. Chem. Res.* **2009**, *43*, 190.
[59] I. Gur, N. A. Fromer, C.-P. Chen, A. G. Kanaras, A. P. Alivisatos, *Nano Lett.* **2006**, *7*, 409.
[60] H. Lee, S. Kim, W. S. Chung, K. Kim, D. Kim, *Sol. Energy Mater. Sol. Cells* **2011**, *95*, 446.
[61] H. C. Liao, C. C. Lin, Y. W. Chen, T. C. Liu, S. Y. Chen, *J. Mater. Chem.* **2010**, *20*, 5429.
[62] W. U. Huynh, J. J. Dittmer, W. C. Libby, G. L. Whiting, A. P. Alivisatos, *Adv. Funct. Mater.* **2003**, *13*, 73.
[63] S. Dayal, N. Kopidakis, D. C. Olson, D. S. Ginley, G. Rumbles, *Nano Lett.* **2009**, *10*, 239.
[64] C. Y. Kwong, A. B. Djurišić, P. C. Chui, K. W. Cheng, W. K. Chan, *Chem. Phys. Lett.* **2004**, *384*, 372.
[65] W. J. E. Beek, M. M. Wienk, R. A. J. Janssen, *Adv. Mater.* **2004**, *16*, 1009.
[66] Y. Y. Lin, T. H. Chu, C. W. Chen, W. F. Su, *Appl. Phys. Lett.* **2008**, *92*.
[67] Y. Y. Lin, T. H. Chu, S. S. Li, C. H. Chuang, C. H. Chang, W. F. Su, C. P. Chang, M. W. Chu, C. W. Chen, *J. Am. Chem. Soc.* **2009**, *131*, 3644.
[68] P. A. van Hal, M. M. Wienk, J. M. Kroon, W. J. H. Verhees, L. H. Slooff, W. J. H. van Gennip, P. Jonkheijm, R. A. J. Janssen, *Adv. Mater.* **2003**, *15*, 118.
[69] S. D. Oosterhout, M. M. Wienk, S. S. van Bavel, R. Thiedmann, J. A. L. Koster, J. Gilot, J. Loos, V. Schmidt, R. A. J. Janssen, *Nat. Mater.* **2009**, *8*, 818.
[70] S. D. Oosterhout, L. J. A. Koster, S. S. van Bavel, J. Loos, O. Stenzel, R. Thiedmann, V. Schmidt, B. Campo, T. J. Cleij, L. Lutsen, D. Vanderzande, M. M. Wienk, R. A. J. Janssen, *Adv. Energy. Mater.* **2011**, *1*, 90.
[71] P. A. van Hal, M. P. T. Christiaans, M. M. Wienk, J. M. Kroon, R. A. J. Janssen, *J. Phys. Chem. B* **1999**, *103*, 4352.
[72] A. C. Arango, S. A. Carter, P. J. Brock, *Appl. Phys. Lett.* **1999**, *74*, 1698.
[73] K. M. Coakley, Y. X. Liu, M. D. McGehee, K. L. Frindell, G. D. Stucky, *Adv. Funct. Mater.* **2003**, *13*, 301.
[74] K. M. Coakley, M. D. McGehee, *Appl. Phys. Lett.* **2003**, *83*, 3380.
[75] C. Melis, A. Mattoni, L. Colombo, *J. Phys. Chem. C* **2010**, *114*, 3401.
[76] A. Abrusci, I. K. Ding, M. Al-Hashimi, T. Segal-Peretz, M. D. McGehee, M. Heeney, G. L. Frey, H. J. Snaith, *Energy Environ. Sci.* **2011**, *4*, 3051.
[77] J. A. Chang, J. H. Rhee, S. H. Im, Y. H. Lee, H. J. Kim, S. I. Seok, M. K. Nazeeruddin, M. Gratzel, *Nano Lett.* **2010**, *10*, 2609.
[78] R. Zhu, C. Y. Jiang, B. Liu, S. Ramakrishna, *Adv. Mater.* **2009**, *21*, 994.
[79] J. B. Baxter, E. S. Aydil, *Sol. Energy Mater. Sol. Cells* **2006**, *90*, 607.
[80] X. Feng, K. Shankar, O. K. Varghese, M. Paulose, T. J. Latempa, C. A. Grimes, *Nano Lett.* **2008**, *8*, 3781.
[81] O. K. Varghese, M. Paulose, C. A. Grimes, *Nat. Nanotechnol.* **2009**, *4*, 592.
[82] I. Gonzalez-Valls, M. Lira-Cantu, *Energy Environ. Sci.* **2009**, *2*, 19.
[83] J. Huang, Z. G. Yin, Q. D. Zheng, *Energy Environ. Sci.* **2011**, *4*, 3861.

[84] Q. Zhang, S. Yodyingyong, J. Xi, D. Myers, G. Cao, *Nanoscale* **2012**, *4*, 1436.
[85] D. C. Olson, J. Piris, R. T. Collins, S. E. Shaheen, D. S. Ginley, *Thin Solid Films* **2006**, *496*, 26.
[86] Y.-J. Lee, M. T. Lloyd, D. C. Olson, R. K. Grubbs, P. Lu, R. J. Davis, J. A. Voigt, J. W. P. Hsu, *J. Phys. Chem. C* **2009**, *113*, 15778.
[87] D. C. Olson, Y.-J. Lee, M. S. White, N. Kopidakis, S. E. Shaheen, D. S. Ginley, J. A. Voigt, J. W. P. Hsu, *J. Phys. Chem. C* **2007**, *111*, 16640.
[88] D. C. Olson, Y. J. Lee, M. S. White, N. Kopidakis, S. E. Shaheen, D. S. Ginley, J. A. Voigt, J. W. P. Hsu, *J. Phys. Chem. C* **2008**, *112*, 9544.
[89] M. T. Lloyd, R. P. Prasankumar, M. B. Sinclair, A. C. Mayer, D. C. Olson, J. W. P. Hsu, *J. Mater. Chem.* **2009**, *19*, 4609.
[90] T. C. Monson, M. T. Lloyd, D. C. Olson, Y.-J. Lee, J. W. P. Hsu, *Adv. Mater.* **2008**, *20*, 4755.
[91] Y. Y. Lin, Y. Y. Lee, L. W. Chang, J. J. Wu, C. W. Chen, *Appl. Phys. Lett.* **2009**, *94*.
[92] P. Ruankham, L. Macaraig, T. Sagawa, H. Nakazumi, S. Yoshikawa, *J. Phys. Chem. C* **2011**, *115*, 23809.
[93] P. Tiwana, P. Docampo, M. B. Johnston, H. J. Snaith, L. M. Herz, *ACS Nano* **2011**, *5*, 5158.
[94] M. T. Dang, L. Hirsch, G. Wantz, *Adv. Mater.* **2011**, *23*, 3597.
[95] K. Takanezawa, K. Hirota, Q. S. Wei, K. Tajima, K. Hashimoto, *J. Phys. Chem. C* **2007**, *111*, 7218.
[96] J. Ajuria, I. Etxebarria, E. Azaceta, R. Tena-Zaera, N. Fernandez-Montcada, E. Palomares, R. Pacios, *Phys. Chem. Chem. Phys.* **2011**, *13*, 20871.
[97] S. E. Shaheen, D. S. Ginley, G. E. Jabbour, *MRS Bulletin* **2005**, *30*, 10.
[98] X. Y. Zhu, Q. Yang, M. Muntwiler, *Acc. Chem. Res.* **2009**, *42*, 1779.
[99] L. Schmidt-Mende, S. M. Zakeeruddin, M. Gratzel, *Appl. Phys. Lett.* **2005**, *86*.
[100] U. Bach, D. Lupo, P. Compte, J. Moser, F. Weissortel, J. Salbeck, H. Spreitzer, M. Grätzel, *Nature* **1998**, *395*, 583.
[101] S. Günes, N. S. Sariciftci, *Inorg. Chim. Acta* **2008**, *361*, 581.
[102] J. Bouclé, H. J. Snaith, N. C. Greenham, *J. Phys. Chem. C* **2010**, *114*, 3664.
[103] P. Ravirajan, A. M. Peiro, M. K. Nazeeruddin, M. Grätzel, D. D. C. Bradley, J. R. Durrant, J. Nelson, *J. Phys. Chem. B* **2006**, *110*, 7635.
[104] S. Wu, Q. Tai, F. Yan, *J. Phys. Chem. C* **2010**, *114*, 6197.
[105] Q. Zhang, C. S. Dandeneau, X. Zhou, G. Cao, *Adv. Mater.* **2009**, *21*, 4087.
[106] J. B. Baxter, A. M. Walker, K. van Ommering, E. S. Aydil, *Nanotechnol.* **2006**, *17*, S304.
[107] M. Law, L. E. Greene, J. C. Johnson, R. Saykally, P. Yang, *Nat. Mater.* **2005**, *4*, 455.
[108] L. Vayssieres, *Adv. Mater.* **2003**, *15*, 464.
[109] L. E. Greene, M. Law, J. Goldberger, F. Kim, J. C. Johnson, Y. Zhang, R. J. Saykally, P. Yang, *Angew. Chem. Intl. Ed.* **2003**, *42*, 3031.
[110] L. E. Greene, M. Law, B. D. Yuhas, P. Yang, *J. Phys. Chem. C* **2007**, *111*, 18451.
[111] J. J. Vegh, D. B. Graves, *Plasma Processes Polym.* **2009**, *6*, 320.
[112] J. Zekonyte, V. Zaporojtchenko, F. Faupel, *Nucl. Instrum. Methods Phys. Res., Sect. B* **2005**, *236*, 241.

[113] S. Dag, L.-W. Wang, *Nano Lett.* **2008**, *8*, 4185.
[114] H. Sirringhaus, P. J. Brown, R. H. Friend, M. M. Nielsen, K. Bechgaard, B. M. W. Langeveld-Voss, A. J. H. Spiering, R. A. J. Janssen, E. W. Meijer, P. Herwig, D. M. de Leeuw, *Nature* **1999**, *401*, 685.
[115] A. Soudi, P. Dhakal, Y. Gu, *Appl. Phys. Lett.* **2010**, *96*.
[116] S. A. Choulis, Y. Kim, J. Nelson, D. D. C. Bradley, M. Giles, M. Shkunov, I. McCulloch, *Appl. Phys. Lett.* **2004**, *85*, 3890.
[117] D. Mondelaers, G. Vanhoyland, H. Van den Rul, J. D'Haen, M. K. Van Bael, J. Mullens, L. C. Van Poucke, *J. Sol-Gel Sci. Technol.* **2003**, *26*, 523.
[118] O. Inganäs, W. R. Salaneck, J. E. Österholm, J. Laakso, *Synth. Met.* **1988**, *22*, 395.
[119] P. J. Brown, D. S. Thomas, A. Köhler, J. S. Wilson, J.-S. Kim, C. M. Ramsdale, H. Sirringhaus, R. H. Friend, *Phys. Rev. B* **2003**, *67*, 064203.
[120] Z. H. Kafafi, B. P. Rand, K. Lee, R. A. J. Janssen, *IEEE J. Sel. Top. Quantum Electron.* **2010**, *16*, 1512.
[121] J. Bouclé, P. Ravirajan, J. Nelson, *J. Mater. Chem.* **2007**, 3141.
[122] T. Xu, Q. Qiao, *Energy Environ. Sci.* **2011**, *4*, 2700.
[123] W. J. E. Beek, M. M. Wienk, R. A. J. Janssen, *J. Mater. Chem.* **2005**, *15*, 2985.
[124] Y. C. Kong, D. P. Yu, B. Zhang, W. Fang, S. Q. Feng, *Appl. Phys. Lett.* **2001**, *78*, 407.
[125] G. Jimenez-Cadena, E. Comini, M. Ferroni, A. Vomiero, G. Sberveglieri, *Mater. Chem. Phys.* **2010**, *124*, 694.
[126] D.-S. Kang, H. S. Lee, S. K. Han, V. Srivastava, E. S. Babu, S.-K. Hong, M.-J. Kim, J.-H. Song, J.-H. Song, H. Kim, D. Kim, *J. Alloys Compd.* **2011**, *509*, 5137.
[127] Y. Leprince-Wang, S. Bouchaib, T. Brouri, M. Capo-Chichi, K. Laurent, J. Leopoldes, S. Tusseau-Nenez, L. Lei, Y. Chen, *Mater. Sci. Eng., B* **2010**, *170*, 107.
[128] K. Laurent, T. Brouri, M. Capo-Chichi, D. P. Yu, Y. Leprince-Wang, *J. Appl. Phys.* **2011**, *110*, 094310.
[129] L. E. Greene, M. Law, D. H. Tan, M. Montano, J. Goldberger, G. Somorjai, P. Yang, *Nano Lett.* **2005**, *5*, 1231.
[130] B. Kannan, K. Castelino, A. Majumdar, *Nano Lett.* **2003**, *3*, 1729.
[131] D. H. Weber, A. Beyer, B. Volkel, A. Golzhauser, E. Schlenker, A. Bakin, A. Waag, *Appl. Phys. Lett.* **2007**, *91*, 253126.
[132] L. Baeten, B. Conings, H.-G. Boyen, J. D'Haen, A. Hardy, J. V. Manca, M. K. Van Bael, *Adv. Mater.* **2011**, *23*, 2802.
[133] L. Znaidi, G. J. A. A. Soler Illia, S. Benyahia, C. Sanchez, A. V. Kanaev, *Thin Solid Films* **2003**, *428*, 257.
[134] Y. Lee, Y. Zhang, S. L. G. Ng, F. C. Kartawidjaja, J. Wang, *J. Am. Ceram. Soc.* **2009**, *92*, 1940.
[135] A. Roelofs, T. Schneller, K. Szot, R. Waser, *Nanotechnol.* **2003**, *14*, 250.
[136] B. Conings, L. Baeten, H.-G. Boyen, D. Spoltore, J. D'Haen, L. Grieten, P. Wagner, M. K. Van Bael, J. V. Manca, *J. Phys. Chem. C* **2011**, *115*, 16695.
[137] J. J. M. Halls, C. A. Walsh, N. C. Greenham, E. A. Marseglia, R. H. Friend, S. C. Moratti, A. B. Holmes, *Nature* **1995**, *376*, 498.
[138] C. Deibel, V. Dyakonov, *Rep. Prog. Phys.* **2010**, *73*.

[139] G. Dennler, M. C. Scharber, C. J. Brabec, *Adv. Mater.* **2009**, *21*, 1323.
[140] B. C. Thompson, J. M. J. Fréchet, *Angew. Chem. Intl. Ed.* **2008**, *47*, 58.
[141] A. Swinnen, I. Haeldermans, P. Vanlaeke, J. D'Haen, J. Poortmans, M. D'Olieslaeger, J. V. Manca, *Eur. Phys. J. Appl. Phys.* **2006**, *36*, 251.
[142] T. Martens, J. D'Haen, T. Munters, Z. Beelen, L. Goris, J. Manca, M. D'Olieslaeger, D. Vanderzande, L. De Schepper, R. Andriessen, *Synth. Met.* **2003**, *138*, 243.
[143] J. L. Bredas, J. E. Norton, J. Cornil, V. Coropceanu, *Acc. Chem. Res.* **2009**, *42*, 1691.
[144] C. Lin, W. C. Pan, F. Y. Tsai, *Synth. Met.* **2010**, *160*, 2543.
[145] H. Y. Park, K. Kim, D. Y. Kim, S. K. Choi, S. M. Jo, S. Y. Jang, *J. Mater. Chem.* **2011**, *21*, 4457.
[146] M. Saito, S. Fujihara, *Energy Environ. Sci.* **2008**, *1*, 280.
[147] A. M. Peiro, P. Ravirajan, K. Govender, D. S. Boyle, P. O'Brien, D. D. C. Bradley, J. Nelson, J. R. Durrant, *J. Mater. Chem.* **2006**, *16*, 2088.
[148] M. Guo, P. Diao, X. Wang, S. Cai, *J. Solid State Chem.* **2005**, *178*, 3210.
[149] K. Hara, T. Horiguchi, T. Kinoshita, K. Sayama, H. Sugihara, H. Arakawa, *Sol. Energy Mater. Sol. Cells* **2000**, *64*, 115.
[150] V. V. Kislyuk, O. P. Dimitriev, *J. Nanosci. Nanotechnol.* **2008**, *8*, 131.
[151] Y. W. Heo, D. P. Norton, L. C. Tien, Y. Kwon, B. S. Kang, F. Ren, S. J. Pearton, J. R. LaRoche, *Mater. Sci. Eng., R* **2004**, *47*, 1.
[152] K. Chen-Hao, W. Jih-Jen, *Nanotechnol.* **2007**, *18*, 505706.
[153] J.-J. Wu, G.-R. Chen, H.-H. Yang, C.-H. Ku, J.-Y. Lai, *Appl. Phys. Lett.* **2007**, *90*, 213109.
[154] E. Barsoukov, J. R. Macdonald, *Impedance Spectroscopy - Theory, Experiment, and Applications, 2nd edition*, John Wiley & Sons, Inc., Hoboken, New Jersey 2005.
[155] J. Bisquert, *J. Phys. Chem. B* **2001**, *106*, 325.
[156] S. Wu, J. Li, Q. Tai, F. Yan, *J. Phys. Chem. C* **2010**, *114*, 21873.
[157] J. Bisquert, F. Fabregat-Santiago, I. Mora-Seró, G. Garcia-Belmonte, S. Giménez, *J. Phys. Chem. C* **2009**, *113*, 17278.
[158] F. Fabregat-Santiago, J. Bisquert, E. Palomares, L. Otero, D. Kuang, S. M. Zakeeruddin, M. Grätzel, *J. Phys. Chem. C* **2007**, *111*, 6550.
[159] C. Longo, A. F. Nogueira, M.-A. De Paoli, H. Cachet, *J. Phys. Chem. B* **2002**, *106*, 5925.
[160] Q. Wang, S. Ito, M. Grätzel, F. Fabregat-Santiago, I. Mora-Seró, J. Bisquert, T. Bessho, H. Imai, *J. Phys. Chem. B* **2006**, *110*, 25210.
[161] G. Garcia-Belmonte, A. Munar, E. M. Barea, J. Bisquert, I. Ugarte, R. Pacios, *Org. Electron.* **2008**, *9*, 847.
[162] Q. Tai, X. Zhao, F. Yan, *J. Mater. Chem.* **2010**, *20*, 7366.
[163] D. Bi, F. Wu, W. Yue, Y. Guo, W. Shen, R. Peng, H. Wu, X. Wang, M. Wang, *J. Phys. Chem. C* **2010**, *114*, 13846.
[164] G. Wang, D. Chen, H. Zhang, J. Z. Zhang, J. Li, *J. Phys. Chem. C* **2008**, *112*, 8850.
[165] J. Tornow, K. Schwarzburg, *J. Phys. Chem. C* **2007**, *111*, 8692.

[166] G. Garcia-Belmonte, P. P. Boix, J. Bisquert, M. Sessolo, H. J. Bolink, *Sol. Energy Mater. Sol. Cells* **2010**, *94*, 366.
[167] A. J. Mozer, N. S. Sariciftci, L. Lutsen, D. Vanderzande, R. Osterbacka, M. Westerling, G. Juska, *Appl. Phys. Lett.* **2005**, *86*, 112104.
[168] D. M. Bagnall, M. Boreland, *Energy Policy* **2008**, *36*, 4390.
[169] R. E. I. Schropp, R. Carius, G. Beaucarne, *MRS Bulletin* **2007**, *32*, 219.
[170] R. Po, M. Maggini, N. Camaioni, *J. Phys. Chem. C* **2009**, *114*, 695.
[171] H. Hoppe, N. S. Sariciftci, *J. Mater. Res.* **2004**, *19*, 1924.
[172] R. R. Lunt, T. P. Osedach, P. R. Brown, J. A. Rowehl, V. Bulović, *Adv. Mater.* **2011**, *23*, 5712.
[173] M. Jørgensen, K. Norrman, F. C. Krebs, *Sol. Energy Mater. Sol. Cells* **2008**, *92*, 686.
[174] S. Bertho, I. Haeldermans, A. Swinnen, W. Moons, T. Martens, L. Lutsen, D. Vanderzande, J. Manca, A. Senes, A. Bonfiglio, *Sol. Energy Mater. Sol. Cells* **2007**, *91*, 385.
[175] D. Credgington, R. Hamilton, P. Atienzar, J. Nelson, J. R. Durrant, *Adv. Funct. Mater.* **2011**, *21*, 2744.
[176] T. Kirchartz, B. E. Pieters, J. Kirkpatrick, U. Rau, J. Nelson, *Phys. Rev. B* **2011**, *83*, 115209.
[177] T.-W. Zeng, C.-C. Ho, Y.-C. Tu, G.-Y. Tu, L.-Y. Wang, W.-F. Su, *Langmuir* **2011**, *27*, 15255.
[178] B. Ray, P. R. Nair, M. A. Alam, *Sol. Energy Mater. Sol. Cells* **2011**, *95*, 3287.
[179] X. Yang, J. Loos, S. C. Veenstra, W. J. H. Verheers, M. M. Wienk, J. M. Kroon, M. A. J. Michels, R. A. J. Janssen, *Nano Lett.* **2005**, *5*, 579.
[180] J. Peet, J. Y. Kim, N. E. Coates, W. L. Ma, D. Moses, A. J. Heeger, G. C. Bazan, *Nat. Mater.* **2007**, *6*, 497.
[181] M. A. Ruderer, S. Guo, R. Meier, H.-Y. Chiang, V. Körstgens, J. Wiedersich, J. Perlich, S. V. Roth, P. Müller-Buschbaum, *Adv. Funct. Mater.* **2011**, *21*, 3382.
[182] N. D. Treat, C. G. Shuttle, M. F. Toney, C. J. Hawker, M. L. Chabinyc, *J. Mater. Chem.* **2011**, *21*.
[183] R. Hamilton, C. G. Shuttle, B. O'Regan, T. C. Hammant, J. Nelson, J. R. Durrant, *J. Phys. Chem. Lett.* **2010**, *1*, 1432.
[184] F. Wu, W. Shen, Q. Cui, D. Bi, W. Yue, Q. Qu, M. Wang, *J. Phys. Chem. C* **2010**, *114*, 20225.
[185] L. Baeten, B. Conings, J. D'Haen, C. D. Dobbelaere, A. Hardy, J. V. Manca, M. K. Van Bael, *ChemPhysChem* **2012, DOI: 10.1002/cphc.201200102**.
[186] L. J. A. Koster, M. Kemerink, M. M. Wienk, K. Maturova, R. A. J. Janssen, *Adv. Mater.* **2011**, *23*, 1670.
[187] L. J. A. Koster, V. D. Mihailetchi, H. Xie, P. W. M. Blom, *Appl. Phys. Lett.* **2005**, *87*, 203502.
[188] H. Azimi, A. Senes, M. C. Scharber, K. Hingerl, C. J. Brabec, *Adv. Energy. Mater.* **2011**, *1*, 1162.
[189] S. R. Cowan, A. Roy, A. J. Heeger, *Phys. Rev. B* **2010**, *82*, 245207.
[190] S. R. Cowan, W. L. Leong, N. Banerji, G. Dennler, A. J. Heeger, *Adv. Funct. Mater.* **2011**, *21*, 3083.
[191] W. L. Leong, S. R. Cowan, A. J. Heeger, *Adv. Energy. Mater.* **2011**, *1*, 517.

[192] J. Bisquert, G. Garcia-Belmonte, *J. Phys. Chem. Lett.* **2011**, *2*, 1950.
[193] C. G. Shuttle, A. Maurano, R. Hamilton, B. O'Regan, J. C. de Mello, J. R. Durrant, *Appl. Phys. Lett.* **2008**, *93*.
[194] A. F. Nogueira, I. Montanari, J. Nelson, J. R. Durrant, C. Winder, N. S. Sariciftci, C. Brabec, *J. Phys. Chem. B* **2003**, *107*, 1567.
[195] C. G. Shuttle, B. O'Regan, A. M. Ballantyne, J. Nelson, D. D. C. Bradley, J. d. Mello, J. R. Durrant, *Appl. Phys. Lett.* **2008**, *92*, 093311.
[196] H. Ohkita, S. Ito, *Polymer* **2011**, *52*, 4397.
[197] A. Maurano, C. G. Shuttle, R. Hamilton, A. M. Ballantyne, J. Nelson, W. Zhang, M. Heeney, J. R. Durrant, *J. Phys. Chem. C* **2011**, *115*, 5947.
[198] Z. Li, F. Gao, N. C. Greenham, C. R. McNeill, *Adv. Funct. Mater.* **2011**, *21*, 1419.
[199] H. Nakanishi, B. A. Grzybowski, *J. Phys. Chem. Lett.* **2010**, *1*, 1428.
[200] C. Jäger, D. Haarer, B. Peng, M. Thelakkat, *Appl. Phys. Lett.* **2004**, *85*, 6185.
[201] A. J. Morfa, A. M. Nardes, S. E. Shaheen, N. Kopidakis, J. van de Lagemaat, *Adv. Funct. Mater.* **2011**, *21*, 2580.
[202] A. J. Morfa, A. M. Nardes, S. E. Shaheen, N. Kopidakis, J. van de Lagemaat, *Adv. Funct. Mater.* **2011**, *21*, 4210.
[203] B. J. Leever, C. A. Bailey, T. J. Marks, M. C. Hersam, M. F. Durstock, *Adv. Energy. Mater.* **2012**, *2*, 120.
[204] J. Bisquert, F. Fabregat-Santiago, I. Mora-Seró, G. Garcia-Belmonte, S. Giménez, *J. Phys. Chem. C* **2009**, *113*, 17278.
[205] B. C. O'Regan, J. R. Durrant, P. M. Sommeling, N. J. Bakker, *J. Phys. Chem. C* **2007**, *111*, 14001.
[206] A. Maurano, R. Hamilton, C. G. Shuttle, A. M. Ballantyne, J. Nelson, B. O'Regan, W. Zhang, I. McCulloch, H. Azimi, M. Morana, C. J. Brabec, J. R. Durrant, *Adv. Mater.* **2010**, *22*, 4987.
[207] A. J. Medford, M. R. Lilliedal, M. Jørgensen, D. Aarø, H. Pakalski, J. Fyenbo, F. C. Krebs, *Opt. Express* **2010**, *18*, 272.
[208] A. Hubler, B. Trnovec, T. Zillger, M. Ali, N. Wetzold, M. Mingebach, A. Wagenpfahl, C. Deibel, V. Dyakonov, *Adv. Energy. Mater.* **2011**, *1*, 1018.
[209] S. E. Shaheen, C. J. Brabec, N. S. Sariciftci, F. Padinger, T. Fromherz, J. C. Hummelen, *Appl. Phys. Lett.* **2001**, *78*, 841.
[210] W. Ma, C. Yang, X. Gong, K. Lee, A. J. Heeger, *Adv. Funct. Mater.* **2005**, *15*, 1617.
[211] A. Pivrikas, H. Neugebauer, N. S. Sariciftci, *Solar Energy* **2011**, *85*, 1226.
[212] G. Li, V. Shrotriya, Y. Yao, J. S. Huang, Y. Yang, *J. Mater. Chem.* **2007**, *17*, 3126.
[213] E. J. Spadafora, R. Demadrille, B. Ratier, B. Grévin, *Nano Lett.* **2010**, *10*, 3337.
[214] J. Jo, S.-S. Kim, S.-I. Na, B.-K. Yu, D.-Y. Kim, *Adv. Funct. Mater.* **2009**, *19*, 866.
[215] W. Ma, C. Yang, A. J. Heeger, *Adv. Mater.* **2007**, *19*, 1387.
[216] S. S. van Bavel, J. Loos, *Adv. Funct. Mater.* **2010**, *20*, 3217.
[217] S. S. van Bavel, M. Barenklau, G. de With, H. Hoppe, J. Loos, *Adv. Funct. Mater.* **2010**, *20*, 1458.
[218] T. Erb, U. Zhokhavets, G. Gobsch, S. Raleva, B. Stühn, P. Schilinsky, C. Waldauf, C. J. Brabec, *Adv. Funct. Mater.* **2005**, *15*, 1193.
[219] Q. Zhang, S. Yodyingyong, J. Xi, D. Myers, G. Cao, *Nanoscale* **2012**, *4*.

[220] B. Conings, L. Baeten, H.-G. Boyen, D. Spoltore, J. D'Haen, M. K. Van Bael, J. V. Manca, *submitted* **2012**.
[221] A. Zen, J. Pflaum, S. Hirschmann, W. Zhuang, F. Jaiser, U. Asawapirom, J. P. Rabe, U. Scherf, D. Neher, *Adv. Funct. Mater.* **2004**, *14*, 757.
[222] C. G. Shuttle, R. Hamilton, J. Nelson, B. C. O'Regan, J. R. Durrant, *Adv. Funct. Mater.* **2010**, *20*, 698.
[223] A. B. Djurisic, X. Chen, Y. H. Leung, A. Man Ching Ng, *J. Mater. Chem.* **2012**, *22*, 6526.
[224] S. H. Park, H. J. Kim, M.-H. Cho, Y. Yi, S. W. Cho, J. Yang, H. Kim, *Appl. Phys. Lett.* **2011**, *98*, 082111.
[225] E. M. J. Johansson, R. Scholin, H. Siegbahn, A. Hagfeldt, H. Rensmo, *Chem. Phys. Lett.* **2011**, *515*, 146.
[226] R. E. Ruther, R. Franking, A. M. Huhn, J. Gomez-Zayas, R. J. Hamers, *Langmuir* **2011**, *27*, 10604.
[227] D. Cahen, A. Kahn, *Adv. Mater.* **2003**, *15*, 271.
[228] M. G. Helander, M. T. Greiner, Z. B. Wang, Z. H. Lu, *Appl. Surf. Sci.* **2010**, *256*, 2602.
[229] R. J. Davis, M. T. Lloyd, S. R. Ferreira, M. J. Bruzek, S. E. Watkins, L. Lindell, P. Sehati, M. Fahlman, J. E. Anthony, J. W. P. Hsu, *J. Mater. Chem.* **2011**, *21*, 1721.
[230] M. C. Scharber, D. Wuhlbacher, M. Koppe, P. Denk, C. Waldauf, A. J. Heeger, C. L. Brabec, *Adv. Mater.* **2006**, *18*, 789.